ULTRAFAST DYNAMICS IN NITRO- AND (ORGANOPHOSPHINE)GOLD(I)-POLYCYCLIC AROMATIC HYDROCARBONS

by

Robert Aaron Vogt

Submitted in partial fulfillment of the requirements

For the degree of Doctor of Philosophy

Dissertation Advisor: Carlos E. Crespo-Hernández

Department of Chemistry

CASE WESTERN RESERVE UNIVERSITY

May, 2013

CASE WESTERN RESERVE UNIVERSITY

SCHOOL OF GRADUATE STUDIES

We hereby approve the thesis/dissertation of

Robert Aaron Vogt

candidate for the degree Doctor of Philosophy degree*.

(signed) Daniel Scherson
(chair of the committee)

Carlos Crespo

Alfred Anderson

Mary Barkley

Kenneth Singer

(date) 11/14/2012

*We also certify that written approval has been obtained for any proprietary material contained therein.

Table of Contents

Table of Contents iii

List of Figures iv

List of Schemes xiv

List of Tables xvi

Abstract 1

Chapter 1. Background and Motivation for this thesis 2

Chapter 2. On the Origin of Ultrafast Nonradiative Transitions in Nitro-PAHs: Excited-State Dynamics in 1-Nitronaphthalene 8

Chapter 3. Role of the Ground State Nitro-Aromatic Torsion Angle on the S_1 State Branching Dynamics and Photochemistry of Nitro-Polycyclic Aromatic Compounds 55

Chapter 4. Excited-State Dynamics of (Organophosphine)Gold(I) Pyrenyl Isomers 87

Chapter 5. Sub-Picosecond Intersystem Crossing in Mono- and Di-(Organophosphine)gold(I) Naphthalene Derivatives in Solution 106

Compound 117

Chapter 6. General Experimental Methods 137

Chapter 7. Future Work 152

Chapter 8. References 153

List of Figures

Figure 2.1. Dependence of the transient absorption signal of 1NN on the pump intensity (in energy units) at the specified probe wavelength. The transient signals were recorded at a fixed time delay of 100 ps in methanol solution. The linear response is lost at pump intensities higher than 4 μJ under the experimental conditions used in this work. 18

Figure 2.2. Structures of the *cis* (left) and *trans* (right) isomers of the 1NN$(CH_3OH)_2$ complex optimized at the B3LYP/IEFPCM/6-311G(d,p) level of theory. The *trans* isomer is more stable than the *cis* by 0.002 kcal/mol in methanol solutions at the same level of theory. The asterisks define the nitro-aromatic torsion angle. 21

Figure 2.3. Ground- and excited-states potential energies of 1NN as a function of the nitro-aromatic torsion angle defined in Fig. 2.2. Single-point energies in (a) cyclohexane, (b) acetonitrile, and (c) for the 1NN$(CH_3OH)_2$ *trans* complex in methanol are reported at the B3LYP/IEFPCM/6-311++G(d,p) and TD-PBE0/NE-IEFPCM/6-311++G(d,p) level of theory for the ground- and excited-states, respectively (see Computational Methods for details). The upper graph in each panel represents the change in the S_1 oscillator strength, while the lower graph in each panel represents the ground-state potential energy as a function of NO_2 torsion angle, respectively. The horizontal black line corresponds to the thermal energy available at 298 K. 23

Figure 2.4. Steady-state absorption spectra of 1NN: (a) in nonpolar and polar aprotic solvents and (b) in polar protic solvents. 24

Figure 2.5. Contour plots of the femtosecond broadband transient absorption spectra of 1NN in cyclohexane, acetonitrile, and pentanol solutions. 26

Figure 2.6. Femtosecond transient absorption spectra of 1NN in nonpolar and polar aprotic solvents: (a) short time dynamics and (b) long time dynamics. Note that the transient absorption spectra cease to change after a time delay of ~40 ps..... 27

Figure 2.7. Transient absorption signals of 1NN in (a) cyclohexane, (b) acetonitrile, and (c) pentanol at the specified probe wavelengths. Best global-fit curves are shown by solid lines (see text for details)..... 28

Figure 2.8. Normalized transient absorption spectra of 1NN in (a) cyclohexane, (b) acetonitrile, and (c) pentanol showing the band narrowing and blue shift characteristic of vibrational cooling dynamics. Bottom panel (d) shows the dynamic Stoke shift of the transient absorption band of 1NN in the time delay window of 40 to 530 ps in pentanol solution. 29

Figure 2.9. Femtosecond transient absorption spectra of 1NN in polar protic solvents: (a) short time dynamics and (b) long time dynamics. 30

Figure 2.10. Picosecond to microsecond transient absorption spectra of 1NN in (a) cyclohexane, (b) acetonitrile, and (c) pentanol. 32

Figure 2.11. Normalized transient absorption signals in the picosecond to microsecond time scale of 1NN in cyclohexane, acetonitrile, and pentanol solvents: (a) in N_2-saturated conditions, and (b) in air-saturated conditions. Best-fit curves are shown by solid lines (see text for details). The reported transient signal is the average of several mono-exponential-decay probe wavelengths. .. 39

Figure 2.12. Correlation of the fourth time constant of 1NN recorded in primary alcohols (methanol, ethanol, n-propanol, n-butanol, and n-pentanol) as a function of (a) viscosity (η) of the solvent, (b) characteristic correlation times ($<\tau>$) and (c) static dielectric constant (ε). Symbols are connected by solid lines to guide eye.44

Figure 2.13. Plausible kinetic mechanisms explain the excited-state dynamics and photochemistry of 1NN in nonpolar, aprotic, and protic solvents. Decay pathways in red describe solvation dynamics and intersystem crossing ($S_0 \leftarrow T_1$) in 1NN observed in primary alcohol solvents. The kinetic model to the right explains satisfactorily the experimental and computational data available to date.47

Figure 3.1. Dependence of the triplet transient absorbance of 2NN and 2M1NN in acetonitrile solutions on the pump power. Measurements were taken at a delay time of 500 ps and at the probe wavelengths shown in the legend. 63

Figure 3.2. Optimized structures of 2-nitronaphthalene (left), 1-nitronaphthalene (center), and 2-methyl-1-nitronaphthalene (right) at the B3LYP/6-311++G(d,p) level of theory. Nitro-aromatic torsion angles are defined with asterisks. 63

Figure 3.3. Potential energy scans for 2NN (left panel) and 2M1NN (right panel) as a function of the nitro-aromatic torsion angle in cyclohexane (top) and acetonitrile (bottom). The torsion angles distribution populated at room temperature is highlighted in gray. Vertical excitation energies were calculated at the TD-PBE0/IEFPCM/6-311++G(d,p) level of theory following ground-state optimizations at the B3LYP/IEFPCM/6-311++G(d,p) level of theory in each solvent. The nitro-aromatic torsion angle was constrained to the specified values during the ground-state optimizations..... 68

Figure 3.4. Optimized S_1 state geometry of 1NN in acetonitrile at the CIS/IEFPCM/6-31+G(d,p) level of theory. Nitro-aromatic torsion angle, as defined in Fig. 1, equal to 75°. Note the pyramidal configuration of the nitro-group. The estimated transition energy and oscillator strength at this level of theory are 3.22 eV and 0.0083, respectively. 69

Figure 3.5. Potential energy scans of the optimized S_1 state as a function of the nitro-aromatic torsion angle for 2NN, 1NN, and 2M1NN in acetonitrile at the TD-PBE0/IEFPCM/6-311++G(d,p) level of theory. Filled symbols represent the torsion angles distribution populated in the ground state at room temperature for each molecule. 69

Figure 3.6. Optimized S_1 state structures for 2NN (left), 1NN (center), and 2M1NN (right) in acetonitrile at the TD-PBE0/IEFPCM/6-311++G(d,p) level of theory. 70

Figure 3.7. Steady-state absorption spectra of 2NN, 1NN, and 2M1NN in cyclohexane (top) and acetonitrile (bottom). 71

Figure 3.8. Photodegradation quantum yield for 2NN, 1NN, and 2M1NN as a function of torsion angles. Vertical bars represent the uncertainty of the photodegradation yields from three independent measurements. Horizontal bars represent the calculated distribution of torsion angles available at room temperature for each molecule. The squares show the torsion angle of the fully-optimized ground-state minimum structure in each molecule. 72

Figure 3.9. Transient absorption spectra of 2NN (top) and 2M1NN (bottom) in cyclohexane (left) and acetonitrile (right). Solvent stimulated Raman emission bands are observed at short time delays. 73

Figure 3.10. Normalized transient absorption spectra of 2NN and 2M1NN at the shown delay times. Arrows highlight the band narrowing and blue shifting characteristic of vibrational cooling dynamics. 76

Figure 3.11. Representative decay traces at selected probe wavelengths for 2NN and 2M1NN in cyclohexane (A and C, respectively) and acetonitrile (B and D, respectively). Solid lines represent the best global-fit curves to the transient absorption data. 77

Figure 3.12. Molecular orbitals participating in the configuration-interaction transitions of the optimized S_1 state in 1NN (top), 2M1NN (middle), and 2NN (bottom) in acetonitrile at the PBE0/IEFPCM/6-311++G(d,p) level of theory.

Similar configuration-interaction transitions were obtained in cyclohexane (not shown). 81

Figure 4.1. Transient absorption spectra for (a) for 1 in chloroform, and (b) and (c) for 2 in chloroform and cyclohexane, respectively. The stimulated Raman signals of the cyclohexane solvent are observable at early time delays. The arrows shown in top panel of (a) highlight the transition from the S_n to the S_1 states. 91

Figure 4.2. Contour plots (a) for 1 in chloroform, and (b) and (c) for 2 in chloroform and cyclohexane, respectively. 93

Figure 4.3. Representative transient absorption signals for (a) 1 in chloroform, (b) 2 in chloroform and (c) 2 in cyclohexane at the specified probe wavelengths (nm). Best global-fit curves are shown by solid lines. 94

Figure 4.4. Transient absorption spectrum for isomer 2 showing vibrational progressions in the excited singlet state at a delay time of 1.4 ps (upper panel) and for the lowest-energy triplet state in cyclohexane (middle panel) and chloroform (bottom panel). 96

Figure 4.5. (a) Partial Kohn-Sham orbital energy level diagrams of model complexes 1′ and 2′. (PBE/Stuttgart ECP and basis on Au; TZVP on C, H, and P). Implicit $CHCl_3$ solvation is included through a polarizable continuum model. Percentage contributions of (phosphine)gold(I) cation and pyrenyl anion

fragments are indicated. (b) and (c) Plots of selected orbitals of 1′ and 2′ respectively (contour level 0.03 a.u.). 98

Figure 4.6. Orbital plots of the HOMO – 2 of 1′ and 2′. The contour level is 0.03 a.u. 99

Figure 4.7. TDDFT-calculated singlet and triplet states of model complexes 1′ (left) and 2′ (right). Calculations include implicit chloroform solvation. Superimposed is a Jablonski diagram depicting the photophysics of the genuine compounds 1 and 2. 100

Figure 4.8. Optimized S_1 state of model complex 2′ at the CIS/IEFPCM/LANL2DZ level of theory in cyclohexane: 78% LUMO ←HOMO and 22% (LUMO + 4) ← (HOMO – 1). 101

Figure 5.1. Optimized structures of the ground state of the model mono- and di-gold(I) naphthalene compounds; (a) 1', (b) 2', and (c) 3', respectively, at the PBE0/(E)-IEFPCM/LANL2DZ level of theory in dichloromethane (left panel). Optimized structures of the first excited singlet state of the model mono- and di-gold(I) naphthalene compounds at the TD-PBE0/(E)-IEFPCM/LANL2DZ level of theory in dichloromethane (right panel). The number assignment of atoms is shown in (a). Carbon atoms are shown in grey, gold atoms in yellow, phosphorus atoms in orange, and hydrogen atoms in white. 110

Figure 5.2. Comparison of the absorption (top panel) and fluorescence (bottom panel) spectra of naphthalene with those for Cy_3PAu(2-naphthyl) (1),

($Cy_3PAu)_2$(2,6-naphthalenediyl) (2), and ($Cy_3PAu)_2$(2,7-naphthalenediyl) (3) in dichloromethane. 115

Figure 5.3. Two-dimensional transient absorption spectra at selected time delays for Cy_3PAu(2-naphthyl) (1) in dichloromethane excited at 285 nm (left panel); for ($Cy_3PAu)_2$(2,6-naphthalenediyl) (2) in dichloromethane excited at 266 nm (middle panel); and for ($Cy_3PAu)_2$(2,7-naphthalenediyl) (3) in dichloromethane excited at 320 nm (right panel). Stimulated Raman emission bands of the solvent are observed around 350 nm within the pulse width of the femtosecond excitation beam in graph (a) of the right panel. The bottom graphs in the left and right panels are blocked with dashed rectangle because the absolute magnitude of the absorption intensities in the spectral region below 420 nm are underestimated by white light generation source used in this work to probe the kinetics from the nanosecond-to-microsecond time scale. 116

Figure 5.4. Top to bottom: contour representation of the multidimensional time-resolved absorption data for Cy_3PAu(2-naphthyl) (1), ($Cy_3PAu)_2$(2,6-naphthalenediyl) (2), and ($Cy_3PAu)_2$(2,7-naphthalenediyl) (3) in dichloromethane. Note that the time scale expands the femtoseconds to microseconds in 1 and 3, while only the femtosecond to nanoseconds in 2..... 118

Figure 5.5. Representative decay traces from the femtosecond to nanosecond time scale for (a) Cy_3PAu(2-naphthyl) (1), (b) ($Cy_3PAu)_2$(2,6-naphthalenediyl) (2), and (c) ($Cy_3PAu)_2$(2,7-naphthalenediyl) (3) in dichloromethane. Best global-fit

curves obtained by modeling the transient absorption data using target analysis based on a sequential kinetic model are shown by solid lines. 121

Figure 5.6. Decay associated spectra of the S_1 state, the receiver T_n state, the vibrationally-excited T_1 state, and the vibrationally-relaxed T_1 state in (a) Cy_3PAu(2-naphthyl) (1), (b) $(Cy_3PAu)_2$(2,6-naphthalenediyl) (2), and (c) $(Cy_3PAu)_2$(2,7-naphthalenediyl) (3) in dichloromethane. The decay associated spectra were obtained by modeling the transient absorption data using target analysis based on a sequential kinetic model. Stimulated Raman emission bands of the solvent are captured in the decay associate spectra of the S_1 state in (c) around 350 nm in part because the dynamics of the S_1 state occurs within the pulse width of the femtosecond excitation beam. The decay associated spectra for the S_1 state was scaled by a factor of 0.25, 0.5 and 1 for panels a, b and c, respectively..... 122

Figure 5.7. Representative decay traces from the nanosecond to microsecond time scale for Cy_3PAu(2-naphthyl) (1) (open squares) and $(Cy_3PAu)_2$(2,7-naphthalenediyl) (3) (open circles) in dichloromethane. Best global-fit curves obtained by modeling the transient absorption data by using an exponential function convoluted with an instrument response function of 500 ps are shown by solid lines. 124

Figure 5.8. Comparison of the goodness of the fit for two representative decay traces at the shown probe wavelengths for compound **1** obtained by using the

target analysis method and a two- (red) or three-steps (blue) sequential kinetic model..... 128

Figure 5.9. Normalized transient absorption spectra for (a) Cy_3PAu(2-naphthyl) (1), (b) $(Cy_3PAu)_2$(2,6-naphthalenediyl) (2), and (c) $(Cy_3PAu)_2$(2,7-naphthalenediyl) (3) in dichloromethane showing the narrowing, blue-shifting, and increased structuring characteristic of vibrational cooling dynamics..... 130

Figure 6.1. Schematic representation of the Falcon laser. Components are as follows: Outcoupler (a), second harmonic generation (b), high transmittance IR/high reflectance 532 nm (c), shutter (d), Q-switch (e), cylindrical lens (f), spherical lens (g), pump chamber (h), polarizer (i), and high reflectance mirror (j). The Falcon is used to pump the Integra. 139

Figure 6.2. Schematic representation of the Integra. Image is based on the one in the Integra manual..... 139

Figure 6.3. Schematic representation of the experimental setup used for the Helios. Key components are shown. Beam alignment camera (a), chopper (b), depolarizer plate (c), 2mm CaF_2 (d), beam splitter (e), CMOS detectors (f), sample (g), 99X reflectance 800 nm mirror (h), retroreflector (i)..... 141

Figure 6.4. Spectum of the white light continuum used as the probe for Eos and Helios systems. 143

Figure 6.5. Spectrum of the light used for irradiating all samples. 147

List of Schemes

Scheme 2.1. Femtosecond broadband transient absorption setup with temporal detection up to hundreds of microsecond. The lettered components are defined as follows: a) dichroic beam splitter, b) Glan-Taylor polarizer, c) neutral density filter, d) depolarizing plate, e) tunable beam splitter, f) sample cell with magnetic stirrer or flow cell, g) variable neutral density filter, h) dichroic all-reflective telescope, j/j') curved mirrors with radius of circular curvature (rcc) = 200 nm (j) and 100 mm (j'), and R) gold coated retroreflector. 14

Scheme 3.1. Pictorial illustration of a kinetic mechanism that can explain the photochemistry of the nitronaphthalene derivatives investigated in this work. Excitation of the distribution of conformations available in the ground state in each molecule to the S_1 state results in different extent of ultrafast bifurcation to two primary relaxation pathways: (1) intersystem crossing to the triplet manifold (left) and dissociation directly from the S_1 state (right) to form the aryloxy and NO radicals. The latter channel is not observed in 2NN due to a sizable energy barrier. The generic yellow Gaussian-shape symbol represents different distributions of torsion angles available for each molecule in the ground-state, the location of which is not the same in each molecule (see Figures 2 and 3). The red, green, and orange Gaussian-shape symbols represent the fraction of population that bifurcates to each of the main relaxation channels (not shown at scale). 80

Scheme 5.1. Proposed sequential kinetic mechanism explaining the excited-state dynamics in Cy_3PAu(2-naphthyl) (1), $(Cy_3PAu)_2$(2,6-naphthalenediyl) (2), and $(Cy_3PAu)_2$(2,7-naphthalenediyl) (3) in dichloromethane. Intersystem crossing from the ligand-centered S_1 state to a receiver, high-energy T_n state with ligand-to-metal (in 2' and 3') or metal-to-ligand (in 1') charge transfer character occurs with a rate constant k_{ISC} ~10^{12} to 10^{13} s^{-1}. Intersystem crossing possibly occurs in the strong non-adiabatic regime. The doorway T_n state internally converts with a rate constant k_{IC} ~5×10^{11} s^{-1} to populate the vibrationally-excited T_1 state. Vibrational cooling dynamics in the T_1 state occurs with a rate constant of k_{VC} ~5×10^{11} s^{-1}. Finally the T_1 state decays by two parallel bimolecular relaxation pathways. The major relaxation pathway is assigned to triplet quenching by molecular oxygen, $k(O_2)$, while the second, minor channel is tentatively assigned to triplet-triplet annihilation or self-quenching (k_b). 131

List of Tables

Table 2.1. Lifetimes from global fits to the transient absorption signals from femtoseconds to the nanoseconds 25

Table 2.2. Lifetimes from global fits to the transient absorption signals from nanoseconds to the microseconds 31

Table 2.3. Vertical excitation energies of the fully optimized 1NN structure in different solvents determined at TD-PBE0/NE-IEFPCM/6-311++G(d,p)//B3LYP/IEFPCM/6-311++G(d,p) level of theory 35

Table 2.4. Singlet-triplet and triplet-triplet energy gaps for the fully optimized 1NN structure in different solvents determined at TD-PBE0/NE-IEFPCM/6-311++G(d,p) //B3LYP/IEFPCM/6-311++G(d,p) level of theory 35

Table 3.1. Vertical excitation energies and selected energy gaps in electron volts obtained from the fully-optimized ground-state structures determined at TD-PBE0/IEFPCM/6-311++G(d,p)||B3LYP/IEFPCM/6-311++G(d,p) level of theory. Oscillator strengths are shown in parentheses. 66

Table 3.2. Lifetimes obtained from a global fit analysis to the transient absorption data. Errors are reported as twice the standard deviation of three or more individual global fit measurements..... 74

Table 4.1. Lifetimes obtained from global fits analyses of the transient absorption spectra..... 90

Table 4.2. Decay lifetimes of the phosphorescent state of 1 and 2 in air-saturated and N_2-saturated conditions 92

Table 5.1. Vertical excitation energies calculated using TD-PBE0 functional, the LANL2DZ basis set, and the NE-IEFPCM solvation model. These energies were obtained relative to the S_0-optimized geometry, which was optimized using the E-IEFPCM solvation model at the same level of theory. The estimated accuracy in energy from a comparison with the experimental data in Figure 5.2 is $\pm$ 0.3 eV.112

Table 5.2. Estimated character of the excited states, in percentage, obtained from a time-dependent density-functional analysis of the single particle transitions constituting each state, relative to the S_0-optimized structures. 113

Table 5.3. Lifetimes obtained from a global and target analysis of the transient absorption data based on a sequential kinetic model (τ_1 to τ_4) or from an exponential decaying function (τ_5); both model functions were convoluted with the corresponding instrument response functions 117

Table 5.4. Estimation of fluorescence and phosphorescence quantum yields from the net emission yields for Cy_3PAu(2-naphthyl) (1), $(Cy_3PAu)_2$(2,6-naphthalenediyl) (2), and $(Cy_3PAu)_2$(2,7-naphthalenediyl) (3) at room temperature. 119

Ultrafast Dynamics in Nitro- and (Organophosphine)Gold(I)-Polycyclic Aromatic Hydrocarbons

Abstract

by

ROBERT AARON VOGT

The light-induced relaxation pathways of various polycyclic aromatic hydrocarbon (PAH) derivatives were studied using broadband transient absorption with femtosecond (10^{-15} s) time resolution, steady-state Xe-lamp irradiation, UV/Vis spectroscopy and HPLC methods. Ground- and excited-state calculations were performed to help interpret the experimental results. Two types of PAH derivatives were chosen for this research: those substituted with nitro groups and those with gold(I) phosphine groups. In both families of PAH investigated the triplet state is populated in high yield following excitation by UV light. The population of the triplet states occurs ultrafast, with lifetimes in the hundreds of femtoseconds in most cases. Kinetic mechanisms explaining the excited-state dynamics and photochemistry of these molecules are proposed. The experimental findings are reinforced with ground- and excited-state calculations at the density functional level of theory.

Chapter 1. Background and Motivation for this thesis

Thousands of tons of organic aromatic compounds are released annually into the atmosphere as a result of the incomplete combustion of fossil fuels and other organic matter as a result of anthropogenic and natural activities.[1] Polycyclic aromatic hydrocarbons (PAH), including nitro-PAHs, comprise 50 to 74% of mass composition of this emitted particulate matter.[2] Studies have shown that nitro-PAHs are acutely toxic, mutagenic, and carcinogenic compounds[3,4] which constitute one of the most troubling classes of environmental pollutants. Nitro-PAHs are released to the environment directly from a variety of incomplete combustion processes[5] and are also formed in situ by atmospheric reactions of PAHs.[6-8] Nitro-PAHs have been identified as components of grilled food and in diesel, gasoline and wood smoke emissions. They are also commonly found in aquatic systems and in sediments.[3,9-12]

Despite the potential negative impact of nitro-PAHs on human health, the emission of nitro-PAHs to ambient air continues, primarily from municipal incinerators,[13] motor vehicles (particularly from diesel exhausts),[14,15] and industrial power plants[16] among other sources. These emissions are likely to rise with the increase consumption of petroleum and coal, particularly in developing countries. It is estimated that nitro-PAHs account for over 50% of the total vapor- and particle-phase direct mutagenicity of ambient air.[17] Epidemiological studies show that exposure to diesel exhaust and urban air pollution is associated with an increased risk of lung cancer.[12] The increase in lung cancer risk that results from human exposure to particulate air pollution and the detection of nitro-PAH

compounds in lungs of non-smokers with lung cancer have led to not only continue interest in assessing their potential risk to humans but also in monitoring their concentrations and fate in the environment.[18]

Photochemical transformation has been proposed to be one of the main routes of natural removal of nitro-PAHs in the environment.[3,4,19-21] Evidence suggests that the composition of the organic layer of an aerosol surrounding the elemental carbon core significantly influences the photochemistry of nitro-PAHs.[22-24] Nitro-PAHs can interact with a wide variety of organic components found within the atmosphere aerosols, affecting the nitro-PAHs photochemistry.[23-25] Known constituents of wood smoke and diesel particles, such as phenols, substituted phenols, benzaldehydes, and oxygenated PAHs, may accelerate the photodegradation rates. Importantly, nitro-PAHs are frequently more toxic than their parent PAHs,[3] and photochemical degradation of a number of nitro-PAHs in turn leads to products that are more toxic than their parent compounds.[3,26] However, the light-induced transformation mechanisms of nitro-PAHs are still under debate and knowledge of their fates in the environment is of current interest. Certainly, understanding the light-induced reactions and sinks of nitro-PAHs is essential to evaluating the associated environmental exposure and risks.

In addition to studying the photophysics of nitro PAHs, PAH derivatives containing (organophosphine)gold(I) functional groups were also investigated. The photophysics of these compounds is of interest because of their potential use in many applications including metallotherapeutic drugs, photodynamic

therapy, organic near-infrared emitters and sensing applications.[27-34] Comparisons made between the nitro-PAHs and the (organophosphine)gold(I) PAHs reveal striking similarities in their electronic relaxation pathways, particularly, the ultrafast intersystem crossing dynamics and close to unity triplet yields.

The work outlined in this thesis contains specific knowledge about the environmental and structural factors that modulate the light-induced fate and molecular-level mechanisms of nitro- and (organophosphine)gold(I) PAHs in solution. The information presented in this thesis is essential to understanding the photochemistry of these compounds and could lead to future applications.

Chapter 2. On the Origin of Ultrafast Nonradiative Transitions in Nitro-PAHs: Excited-State Dynamics in 1-Nitronaphthalene*

ABSTRACT

The electronic energy relaxation of 1-nitronaphthalene was studied in nonpolar, aprotic, and protic solvents in the time window from femtoseconds to microseconds. Excitation at 340 or 360 nm populates the Franck-Condon $S_1(\pi\pi^*)$ state, which is proposed to bifurcate into two essentially barrierless nonradiative decay channels with sub-200 fs lifetimes. The first main decay channel connects the S_1 state with a receiver T_n state that has considerable $n\pi^*$ character. The receiver T_n state undergoes internal conversion to populate the vibrationally excited $T_1(\pi\pi^*)$ state in 2 to 4 ps. It is shown that vibrational cooling dynamics in the T_1 state depends on the solvent used, with average lifetimes in the time scale from 6 to 12 ps. Furthermore, solvation dynamics competes effectively with vibrational cooling in the triplet manifold in primary alcohols. The relaxed T_1 state undergoes intersystem crossing back to ground state in a few microseconds in N_2-saturated solutions in all the solvents studied. The second minor channel involves conformational relaxation of the bright S_1 state (primarily rotation of the NO_2-group) to populate a dissociative singlet state with significant charge-transfer character and negligible oscillator strength. This dissociative channel is proposed to be responsible for the observed photochemistry in 1-nitronaphthalene. Ground- and excited-state calculations at the density functional level of theory that include bulk and explicit solvent effects lend support to the proposed mechanism where the fluorescent S_1 state decays rapidly and irreversibly to dark excited states. A four-state kinetic model is proposed that satisfactorily explains the origin of the nonradiative electronic relaxation pathways in 1-nitronaphthalene.

* This text has been modified from Reichardt, C.; Vogt, R. A.; Crespo-Hernández, C. E.; "On the Origin of Ultrafast Nonradiative Transitions in Nitro-PAHs: Excited-State Dynamics in 1-Nitronaphthalene", J. *Chem. Phys.* **2009**, *131*, 224518.

INTRODUCTION

Electronic promotions to nπ^* states are possible when heteroatoms are incorporated into a molecule. In general, low-energy n $\rightarrow$ π^* transitions are observed when the heteroatom is conjugated to a π-electron system, but still has lone-pair electrons. Examples include aromatic compounds containing carbonyl-, azo-, nitroso-, and nitro-groups. The n $\rightarrow$ π^* transitions can open up additional nonradiative electronic relaxation channels that can dramatically affect the excited-state dynamics of a molecule relative to the heteroatom-containing counterpart.[35] The subject of this study is 1-nitronaphthalene (1NN), a polycyclic aromatic hydrocarbon containing a single nitro-group. Compared to other heteroatomic compounds, the excited-state dynamics of nitro-polycyclic aromatic hydrocarbons, referred to as nitro-PAHs hereafter, has received significantly less attention.[3,5,36]

Our interest in nitro-aromatic compounds is not exclusively based on the fundamental photochemical insights that can be gained about these heteroaromatic molecules from ultrafast time-resolved studies. Nitro-PAHs also constitute one of the most troubling classes of environmental pollutants. Concern about these compounds arises partly from their ubiquity: nitro-PAHs are released to the environment directly from a variety of incomplete combustion processes[6-8] and are also formed in situ by atmospheric reactions of PAHs.[6-8] They may pose a significant health risk because of their widespread presence in the environment and their genotoxic properties. Photochemical degradation has been suggested to play a major role in the natural removal of nitro-PAHs from the environment,[4]

often leading to oxidation products that are more toxic than their parent compounds.[3,37] However, the photochemistry of nitro-PAHs is still poorly understood.[3,36]

In 2007, Peon and co-workers detected the fleeting fluorescence lifetimes of several nitro-PAHs using the fluorescence up-conversion technique.[38] This work stimulated a renaissance in other research laboratories to understand the time-resolved photochemistry of nitro-PAHs using different spectroscopic techniques.[11,39,-41] Ultrafast transient absorption spectroscopy, in combination with the implementation of time-dependent density functional theory (TD-DFT), has been used recently to investigate the intricate nonradiative relaxation pathways observed in several nitro-PAH compounds.[39-42] In particular, the excited-state dynamics of 1NN has attracted considerable interest[38,41-48] because of three major reasons. 1NN can be considered a building block of most other nitro-PAHs. It is small enough to allow high-level quantum chemical calculations to be performed. Perhaps the main reason for the renewed interest in its photophysics is the recent proposal that 1NN is the organic molecule with the largest intersystem crossing rate ever measured.[41]

Zugazagoitia et al. used pump-probe transient absorption spectroscopy to study the excited-state relaxation pathways of 1NN in several solvents.[42] Single probe-wavelength decay signals in the spectral region from 380 to 700 nm were presented. The authors provided evidence of vibrational cooling in the lowest-energy triplet state (T_1), which was argued to take place in the time scale from 1 to 16 ps. Evidence was presented that the decay of an absorption band below

400 nm is accompanied by the simultaneous increase of an absorption band in the visible assigned to the T_1 state. In their work, cross-phase modulation effects in the solvent and in the cell walls obscured the sub ~1 ps excited-state dynamics,[42] making the direct observation of the ultrafast dynamics in 1NN impossible. The authors thus rely on previous fluorescence up-conversion experiments[41] to suggest that the transient signals below 400 nm can be assigned to an intermediate triplet state, which acts as a receiver state in the transit from the S_1 state to the T_1 state.[42] What is not clear from the above experiments is why the triplet yield of 1NN is only 63%.[43] If the intersystem crossing rate is that large (~2×10^{13} s^{-1})[41] a higher triplet yield would be expected. The relatively small triplet yield is particularly surprising considering that Morales-Cueto et al. previously reported that internal conversion ($S_0 \leftarrow S_1$) in 1NN is negligible based on time-resolved anisotropy measurements using the up-conversion technique.[38] Thus, it became apparent to us that other nonradiative decay pathway must compete with the intersystem crossing rate.

In this contribution, we present a comprehensive experimental and computational study on the excited-state dynamics in 1NN in nonpolar, aprotic and protic solvents. Broadband transient absorption spectroscopic experiments in the time window from femtoseconds to microseconds are presented. The experimental results are complemented with ground- and excited-state quantum chemical calculations that include solvent effects. In addition to the previously observed vibrational cooling dynamics in the triplet manifold, our results reveal a pronounced time-dependent Stokes shift in the T_1 state when primary alcohols

are used as solvent. Furthermore, our combined experimental and computational results lend strong support to the suggestion that a bifurcation of the initially excited bright S_1 state leads to dark excited states in less than 200 fs. Our results satisfactorily explain the origin of the ultrafast nonradiative dynamics in 1NN and why many nitro-PAHs are traditionally considered to be nonfluorescent.[36]

EXPERIMENTAL AND COMPUTATIONAL METHODS

A. Chemicals

1NN was obtained from Sigma-Aldrich (99% purity). 1NN purity was verified using high-performance liquid chromatography (HPLC) and steady-state emission measurements. Fluorescence was not detected from potential impurities. Ethanol (99.8%), n-propanol (99.7%), n-butanol (99.8%), n-pentanol (≥99%) and chloroform (99.8%) were obtained from Sigma-Aldrich. Methanol (99.9%), cyclohexane (99.9%), and DMSO (99.9%) were obtained from Fisher Scientific. Acetonitrile (99.6%) was obtained from Acros. All solvents were used as received. *Caution*: 1NN is moderately toxic. Proper safety precautions should be used at all times to limit potential health risks.

B. Broadband Transient Absorption Setup with Femtosecond to Microsecond Temporal Detection

The experimental setup used in the transient absorption experiments is based on a Quantronix *Integra-i/e 3.5* Laser. A diagram of the system is shown in Scheme 2.1. Femtosecond (fs) pulses are generated at a repetition rate of 1 kHz using a regenerative amplifier in combination with a second two-pass amplifier and a pulse picker. The fundamental laser beam characteristics are continuously

monitored using a *GRENOUILLE* (Model 8-50, Swamp Optics), which is fed by the light transmitted through a high-reflective dielectric mirror. The method employed is based on the frequency-resolved optical gating (FROG) technique developed by Trebino and coworkers.[49] Pulses with full-width-half-maximum of 100 fs centered at 800 nm are typically measured.

An optical parametric amplifier (OPA, TOPAS, Quantronix / Light Conversion) is fed with 1.2 mJ of the fundamental laser beam to generate the desired excitation wavelengths. The 800 nm beam is reduced to a beam diameter of ~10 mm in an all-reflective telescope before it is sent to the OPA. Any contributions to the excitation beam from other wavelengths or polarizations are effectively removed by a reflective wavelength filter (λ-filter) and a Glan-Taylor prism. The excitation pulses are attenuated to the desired intensity (typically 1-3 μJ) using a neutral density optical filter. The use of low excitation intensity is required to minimize cross-phase modulation effects,[50] as well as to work within the linear response region of the sample (see below). The polarization of the excitation pulses is randomized by passing the beam through a depolarizing plate in the spectrometer to prevent rotational relaxation effects from contributing to the kinetics.

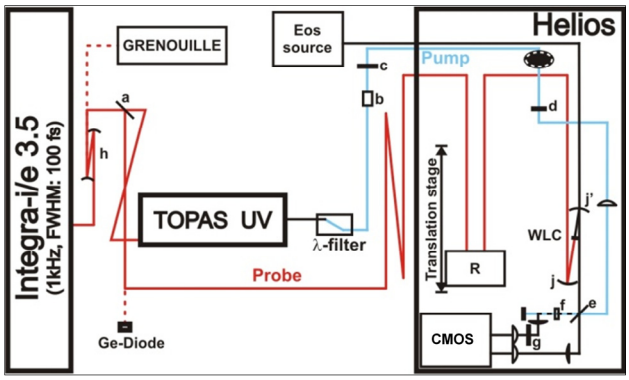

Scheme 2.1. Femtosecond broadband transient absorption setup with temporal detection up to hundreds of microsecond. The lettered components are defined as follows: a) dichroic beam splitter, b) Glan-Taylor polarizer, c) neutral density filter, d) depolarizing plate, e) tunable beam splitter, f) sample cell with magnetic stirrer or flow cell, g) variable neutral density filter, h) dichroic all-reflective telescope, j/j') curved mirrors with radius of circular curvature (rcc) = 200 nm (j) and 100 mm (j'), and R) gold coated retroreflector. Flat mirrors are omitted for clarity.

A broadband transient absorption spectrometer (Helios, Ultrafast Systems, LLC) is used for data acquisition. The spectrometer includes an optical delay line that provides a maximum time delay of 3.2 ns and an all-reflective optics white light continuum (WLC) generation scheme for broadband probing. A continuously moving 2 mm CaF_2 crystal is used for continuum generation giving access to the spectral range from 350 to 720 nm. A dichroic optical filter is used to block wavelengths higher than 730 nm to prevent saturation of the CMOS detector by the fundamental beam. The broadband probe pulses are split in two fractions, re-collimated, and focused into optical fibers leading into the spectrometer/CMOS detection units. One of the two beams passes a 2 mm optical path length sample cell (Quartz, Starna Cells, Inc.) for probing the signal, while the other beam is used as reference for the spectral composition of the white light. Every other pump pulse is blocked by a synchronized chopper wheel to generate a reference

signal, leading to an alternating sequence of spectra with and without sample excitation.

The broadband femtosecond probe pulses are corrected for group velocity dispersion (GVD)[51] using a home-made LabView (National Instruments, Inc.) program as follows. GVD causes light on the blue side of the spectrum to lag behind light on the red side. This is corrected so that the spectrum reported at each delay time is accurate. The solvent-only non-linear response dataset is acquired back-to-back with the sample signal dataset in any given solvent. Then the wavelength-dependent time-zero t_0, i.e. the temporal overlap of the pump pulse with a given probe wavelength of the WLC, is determined by fitting gaussian functions of the type $f_{coh}(t)$ to single-wavelength traces using Equation 1.

$$f_{coh}(t) = \left[a_1 + a_2 \cdot (t - t_0) + a_3 \cdot \left((t - t_0)^2 - 1 \right) \right] \cdot e^{-\frac{(t-t_0)^2}{b}} + y_{offset} \qquad (1)$$

The parameters of this fit are the amplitudes of the gaussian functions and their first and second derivatives (a_1 to a_3); the width parameter *b*; the origin of the function t_0 t_0; and an optional y_{offset}. Interpolation of the $t_0(\lambda)$ extracted from the fourth-order polynomial for the solvent-only dataset allows the GVD correction to the sample signal dataset to be performed in back-to-back experiments. Data acquisition is processed by the LabView-based software included with the Helios spectrometer. In this work, a typical averaging time for a single spectrum of 2 s, equaling 1,000 single laser shots, is used.

Flipping the curved mirror *j'* in Scheme 2.1 allows the use of a complementary white light generation source in the spectral range from ~350 to 675 nm (Eos, Ultrafast Systems, LLC). This light source is used to follow the time evolution of the transient absorption signals on the time scale from hundreds of picoseconds to microseconds. In this mode, a diode that monitors the WLC source is used as external trigger that synchronizes the femtosecond laser system. This hybrid transient absorption setup permits the measurement of decay signals with a time resolution of 400 ps, bridging the gap between conventional femtosecond and nanosecond broadband transient absorption spectrometers.

Data analysis is performed with Igor Pro 6.04 software (Wavemetrics, Inc.). A sum of exponential terms, convoluted with a Gaussian response function, was used to globally fit the kinetic traces. A delta function is included in the fitting subroutine to account for any coherent response signals whenever needed. An instrument response function of 160 $\pm$ 50 fs is estimated from the coherent UV signal seen in the solvent-only scans. In the global fitting analysis, representative kinetic traces in the spectral range between 350 nm and 700 nm are selected (nineteen equidistant traces in this work) for each dataset of at least three independent experiments. The lifetimes are linked for all the traces while the amplitudes are left wavelength-dependent. The decay of the transient absorption signals obtained using the Eos module are analyzed using the same global fitting method described above but with a fixed instrument response function of 400 ps. The reported uncertainties for the kinetic analysis are twice the standard

deviation (2σ) of at least three independent and globally fitted experiments in a given solvent.

The absorbance of the 1NN solutions in a given solvent was adjusted to 1.0 ± 0.2 at the excitation wavelength of 340 nm or 1.5 ± 0.3 at the excitation wavelength of 360 nm using a 2 mm optical path length cell. Within experimental uncertainties, no differences in the transient absorption spectra were observed when exciting the solutions at 340 nm versus 360 nm. However, excitation at 340 nm was frequently used in order to conveniently avoid light scattering from the excitation beam which would interfere with the measurement of transient signals in the spectral region around 350 nm. The sample in the probed volume is continuously renewed using a Teflon-coated stir bar and a magnetic stirrer to avoid re-excitation of the excited volume by successive laser pulses. Solutions were carefully monitored for photodegradation using steady-state absorption spectroscopy (Cary 100 spectrophotometer, Varian, Inc.) throughout the experiments. The samples were replaced with fresh solutions as needed; typically before a 5 % decrease in steady-state absorbance at the excitation wavelength was observed.

The probe beam was focused into the sample cell, where it was superimposed on the pump pulse using a pump/probe beam diameter ratio of three. Under our experimental conditions, the transient absorption signals of 1NN in methanol solutions deviated from linearity at pump intensities higher than 4 μJ (Figure 2.1), suggesting a saturation of an intermediate state and/or competing triplet-triplet annihilation processes at excitation intensities higher than 4 μJ.

Similar deviations from linearity in ΔA were observed in other solvents. Therefore, care was taken to work in the linear response region of the transient absorption signals in each solvent used. The transient absorption data in the visible range of the spectrum (i.e., ~450 to 720 nm) were also recorded using a 2 mm sapphire plate as a white light continuum generation source while exciting the solutions at 360 nm. The results of the latter experiments were identical to those using CaF_2 and are thus not presented.

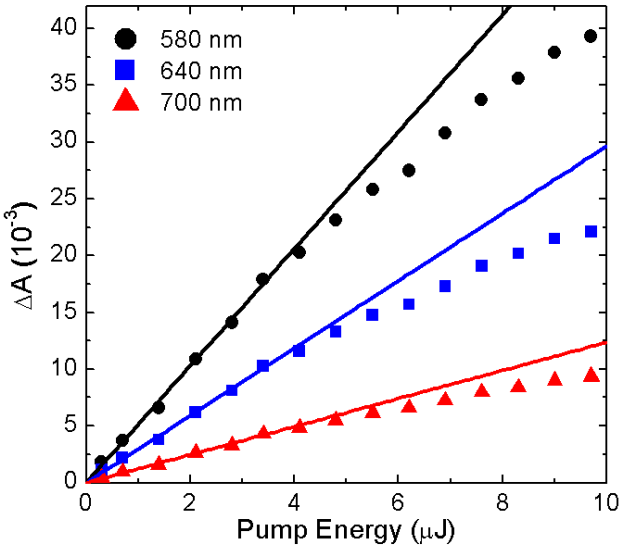

Figure 2.1. Dependence of the transient absorption signal of 1NN on the pump intensity (in energy units) at the specified probe wavelength. The transient signals were recorded at a fixed time delay of 100 ps in methanol solution. The linear response is lost at pump intensities higher than 4 μJ under the experimental conditions used in this work (see Experimental Methods for details).

C. Quantum Chemical Calculations

All calculations were performed using the Gaussian 03 suite of programs.[52] Ground-state optimizations were performed at the density functional level of theory (DFT) using the B3LYP functional.[53] Optimized ground-state

geometries were calculated without any geometrical restriction except those enforced by symmetry. The optimized geometries were confirmed to be local minima on the ground-state potential energy surface through vibrational frequency analysis at the B3LYP/6-31++G(d,p) level of theory.

Excited-state calculations were performed using the time-dependent implementation of density functional theory (TD-DFT) and the PBE0 functional.[54] The PBE0 functional provides accurate (i.e., within 0.2 eV or less) excited-state energies,[40,55-59] singlet-triplet energy gaps,[40,57] excited-state ordering,[55,58] and ground-state absorption spectra,[40] particularly when solvent effects are taken into account.[40,58-60]

The following gradient procedure was used to optimize the ground-state geometry of 1NN in vacuum: first with a small basis set B3LYP/6-31G, and then B3LYP/6-31G(d,p), B3LYP/6-31++G(d,p), B3LYP/6-311++G(d,p), and B3LYP/6-311++G(2d,2p) levels of theory. A similar gradient procedure was used to obtain the vertical excitation energies in vacuum but using the PBE0 functional. The ground-state nuclear coordinates of 1NN converged within 0.004 Å for the bond distances and 0.9° for the nitro-group torsional angles at the B3LYP/6-311++G(d,p) level of theory. Convergence of the vertical excitation energies within 0.06 eV or smaller was also obtained at the TD-PBE0/6-311++G(d,p) level of theory. Thus, the 6-311++G(d,p) standard basis set was used for all other ground- and excited-state calculations reported in this work.

Solvent effects are expected to lead to large ground- and excited-state energy changes and re-ordering of excited states in heteroaromatic compounds.[55] Thus, the effect of the bulk solvent dielectric on the ground-state geometries and on the excited-state vertical energies was modeled by performing self-consistent reaction field (SCRF) calculations using the polarizable continuum model (PCM)[61] with the integral equation formalism (SCRF=IEFPCM).[62] The default solvent parameters were used, as given in Gaussian 03. Vertical excitation energies were modeled using the non-equilibrium (NE) implementation of IEFPCM,[63] as given in Gaussian03. Results are presented at the TD-PBE0/NE-IEFPCM/6-311++G(d,p) level of theory.

The inclusion of bulk solvent effects is expected to satisfactorily model the ground- and excited-state properties of 1NN in non-polar and polar aprotic solvents. However, explicit solvent-solute hydrogen bonding interactions can significantly influence the electronic properties of 1NN due to the presence of oxygen atoms with lone pairs in the nitro-group. Thus, additional ground- and excited-state calculations were performed that include explicit solute-solvent interactions using methanol as a model solvent. In this set of calculations, 1NN plus two methanol molecules were fully optimized at the B3LYP/IEFPCM/6-311G(d,p) level of theory without any geometry restrictions, whereas single point calculations were obtained at B3LYP/IEFPCM/6-311++G(d,p) level of theory. Two local minima were optimized for the 1NN$(CH_3OH)_2$ complex in the ground state: one in which the alkyl groups of the methanol molecules are *cis* and the other where the alkyl groups are *trans* to the nitro-group of 1NN (Figure 2.2).

Even though the *trans* complex is lower in energy than the *cis* by only 0.02 kcal/mol at the B3LYP/IEFPCM/6-311++G(d,p) level of theory, it was used exclusively for all subsequent calculations. Vertical excitation energies for the *trans* 1NN$(CH_3OH)_2$ complex were obtained at the PBE0/NE-IEFPCM/6-311++G(d,p) level (i.e., bulk solvent effects were also included). Basis set superposition errors were not taken into consideration as they are not expected to significantly influence the semi-quantitative results obtained in this "super-molecule" approach.

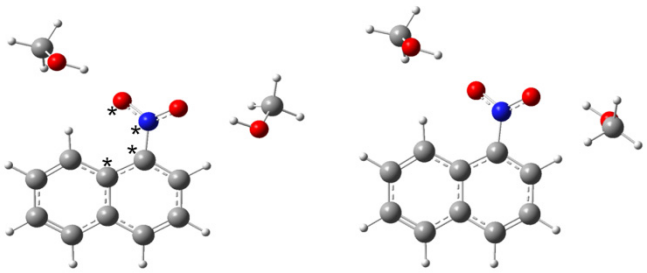

Figure 2.2. Structures of the *cis* (left) and *trans* (right) isomers of the 1NN$(CH_3OH)_2$ complex optimized at the B3LYP/IEFPCM/6-311G(d,p) level of theory. The *trans* isomer is more stable than the *cis* by 0.002 kcal/mol in methanol solutions at the same level of theory. The asterisks define the nitro-aromatic torsion angle.

D. Estimation of Ground- and Excited-State PES using the Nitro-Aromatic Torsion Angle as Variable Nuclear Coordinate

Previous experiments and calculations have suggested that rotation of the nitro-group is one of the main nuclear relaxation coordinates in the excited states in nitro-PAHs.[40,64,65] Thus, ground- and excited-states potential energy surfaces (PES) of 1NN in cyclohexane and acetonitrile were also modeled using the nitro-aromatic torsion angle as a variable nuclear coordinate at the TD-PBE0/NE-IEFPCM/6-311++G(d,p)//B3LYP/IEFPCM/6-311G(d,p) level of theory. In this set

of calculations, all nuclear coordinates were fully optimized in the ground state except for the nitro-aromatic torsion angle, which was fixed at discrete values between -90 to 90 degrees. The estimated potential energy from -90 to 0 degrees is identical to that from 0 to 90 degrees, as expected from symmetry considerations (Figure 2.3a,b). The PES were also calculated for the *trans* 1NN/$(CH_3OH)_2$ complex from -90 to 0 degrees at the same level of theory (Figure 2.3c). Note that symmetry is broken for this complex and thus the potential energy of the complex from -90 to 0 degrees is not simply the mirror image of that from 0 to 90 degrees. In this latter set of calculations, all nuclear coordinates were fixed to values of the fully optimized ground-state complex geometry except that of the nitro-aromatic torsion angle that was used as a variable nuclear coordinate.

RESULTS

A. Solvatochromic Shifts in the Lowest-Energy Steady-State Absorption Band of 1NN

The ground-state absorption spectra of 1NN in nonpolar and polar aprotic solvents are shown in Figure 2.4a. In general, a red shift (bathochromic shift) in the lowest-energy absorption band is observed with an increase in solvent polarity. The exception is chloroform, in which the lowest-energy absorption band of 1NN lies midway between those found in acetonitrile and DMSO. Minimal solvatochromic shifts are observed for the lowest-energy absorption band of 1NN in protic solvents. The absorption band is slightly red-shifted and broadened with a decrease in the length of the alkyl chain of the alcohols (Figure 2.4b). The small red shift of the lowest-energy absorption band suggests that the ground

state of 1NN is only moderately stabilized by an increase in polarity and hydrogen bonding ability of the solvent.

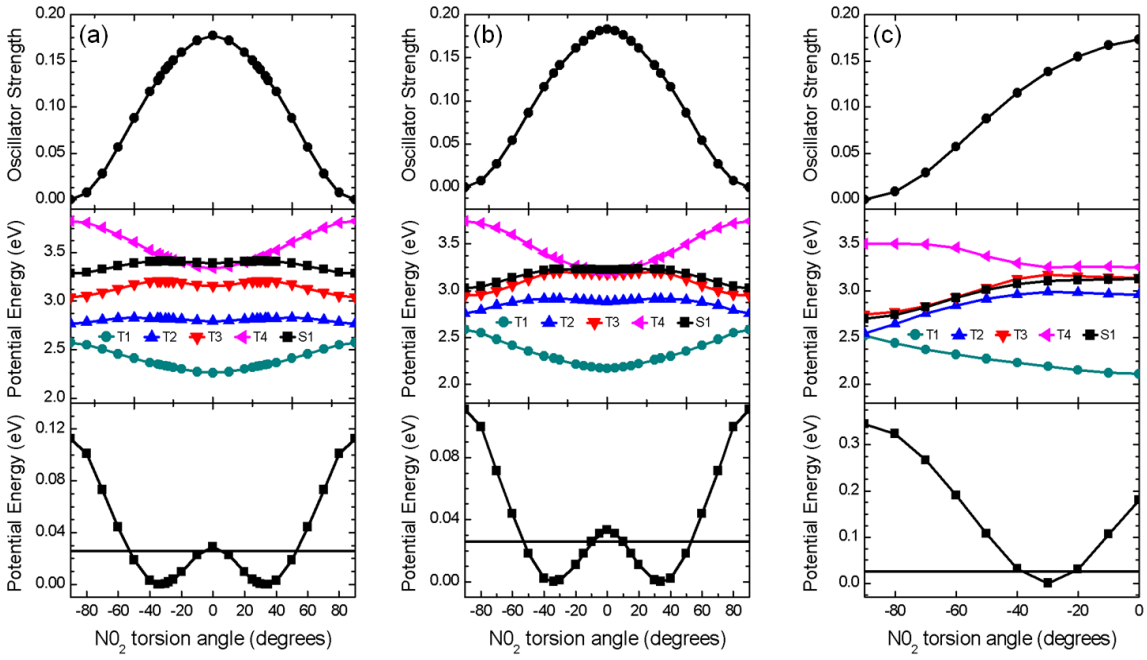

Figure 2.3. Ground- and excited-states potential energies of 1NN as a function of the nitro-aromatic torsion angle defined in Fig. 2.2. Single-point energies in (a) cyclohexane, (b) acetonitrile, and (c) for the 1NN$(CH_3OH)_2$ *trans* complex in methanol are reported at the B3LYP/IEFPCM/6-311++G(d,p) and TD-PBE0/NE-IEFPCM/6-311++G(d,p) level of theory for the ground- and excited-states, respectively (see Computational Methods for details). The upper graph in each panel represents the change in the S_1 oscillator strength, while the lower graph in each panel represents the ground-state potential energy as a function of NO_2 torsion angle, respectively. The horizontal black line corresponds to the thermal energy available at 298 K.

B. Transient Absorption Spectra in Nonpolar and Polar Aprotic Solvents

Femtosecond broadband transient absorption spectroscopy experiments were performed in the spectral range from 350 to 700 nm to directly probe the excited-state dynamics of 1NN. The excitation wavelength (340 nm or 360 nm) was chosen to the red of the ground-state absorption band to minimize excess

vibrational energy in the first excited singlet state. In nonpolar solvents, three exponentials plus a constant offset are needed to adequately fit the spectral evolution in the femtoseconds to three nanoseconds time window. The lifetimes obtained from a global fit analysis are presented in Table 2.1. Representative contour plots and transient absorption spectra are shown in Figure 2.5 and Figure 2.6, while representative kinetic traces are shown in Figure 2.7.

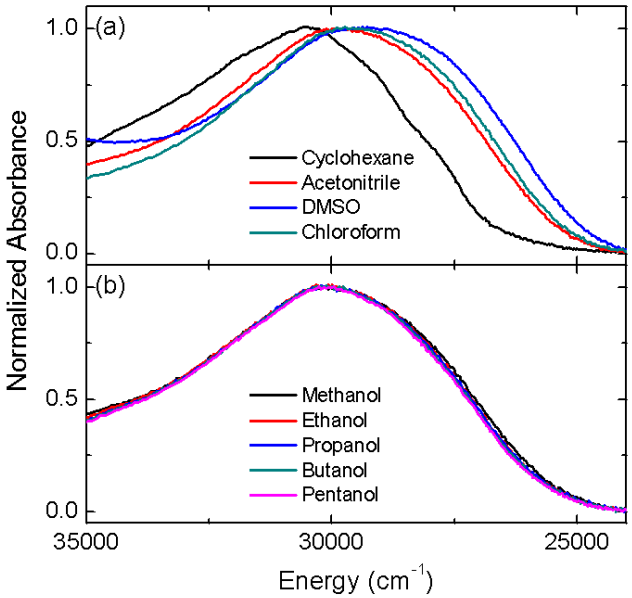

Figure 2.4. Steady-state absorption spectra of 1NN: (a) in nonpolar and polar aprotic solvents and (b) in polar protic solvents.

The changes in the transient absorption spectra of 1NN in cyclohexane solution are shown in Figure 2.6. An absorption band with maximum below 400 nm (UV band hereafter) grows within the temporal resolution of our experimental setup with a lifetime of 110 ± 50 fs (Figure 2.6a, Table 2.1). The absorption maximum of this UV band is not accurately determined because of the contribution of ground-state bleaching (negative absorbance) in this spectral

region, which underlie the excited-state absorption signal (positive absorbance) in the studied solvents. The UV absorption band decays with a lifetime of 2.3 ± 0.2 ps, while a simultaneous increase in absorption in the spectral region above 400 nm in cyclohexane is observed (Figure 2.6b and Figure 2.7). Importantly, the decay of this UV absorption band matches the rise time of the absorption bands above 400 nm (band in the visible hereafter, Figure 2.6). The absorption band in the visible increases rapidly during the first ~45 ps and remains constant thereafter.

Table 2.1. Lifetimes from global fits to the transient absorption signals from femtoseconds to the nanoseconds[a]

Solvent	ε_0[b]	η (cP)[c]	μ (D)[b]	τ_1 (ps)	τ_2 (ps)	τ_3 (ps)	τ_4 (ps)	τ_f (ps)[d]
Cyclohexane	2.02	1.02[e]	0.0	0.11 ± 0.05	2.3 ± 0.2	10.3 ± 0.3	--	0.10 ± 0.02
Chloroform	4.81	0.580	1.2	0.19 ± 0.05	3.6 ± 0.2	12.1 ± 0.6	--	--
Acetonitrile	35.94	0.345[f]	3.5	0.14 ± 0.05	2.8 ± 0.2	11.2 ± 0.4	--	0.05 ± 0.01
DMSO	46.45	1.993[f,g]	4.1	--	2.1 ± 0.2	8.7 ± 0.2	--	--
Pentanol	13.90	4.0	1.7	0.11 ± 0.05	2.12 ± 0.06	10.0 ± 0.2	97 ± 2	0.065 ± 0.01
Butanol	17.51	2.948	1.8	0.15 ± 0.05	2.4 ± 0.1	10.2 ± 0.2	83 ± 2	--
Propanol	20.45	2.256	1.7	0.15 ± 0.05	2.44 ± 0.08	10.6 ± 0.3	56 ± 2	--
EtOH	24.55	1.200	1.7	0.13 ± 0.05	2.4 ± 0.2	10.1 ± 0.6	31 ± 2	--
Methanol	32.66	0.597	1.7	0.17 ± 0.05	1.7 ± 0.2	6.1 ± 0.5	13.4 ± 0.5	0.060 ± 0.01

[a] errors are reported as two times the standard deviation of three or more individual global fit measurements; [b] taken from ref. [74]; [c] all viscosities are taken from ref. [89] at 20 °C except where noted; [d] taken from ref. [41]; [e] viscosity at 17 °C; [f] viscosity at 25 °C; [g] taken from ref. [90]

A closer inspection of the absorption band in the visible shows a systematic blue shift (hypsochromic shift) and band narrowing with an increase in delay time of up to ~45 ps (Figure 2.5 and Figure 2.6b). This spectral evolution can be more conveniently observed in the normalized transient absorption spectra shown in Figure 2.8, and is adequately described by a lifetime of 10.3 ± 0.3 ps in cyclohexane. In chloroform, a blue shift and band narrowing is also

observed, while the spectral evolution of the band in the visible lasts for ~50 ps (Figure 2.6b).

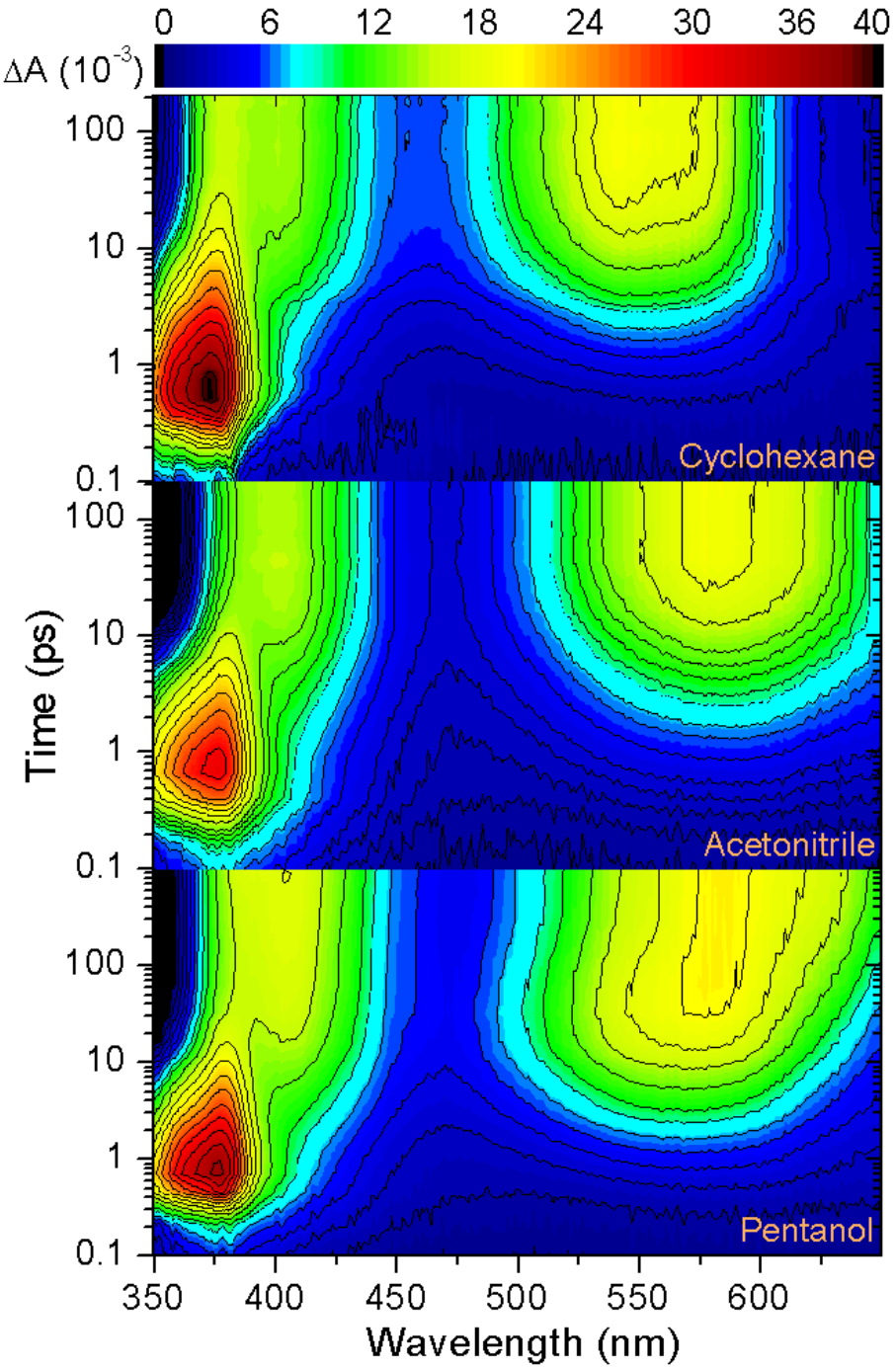

Figure 2.5. Contour plots of the femtosecond broadband transient absorption spectra of 1NN in cyclohexane, acetonitrile, and pentanol solutions.

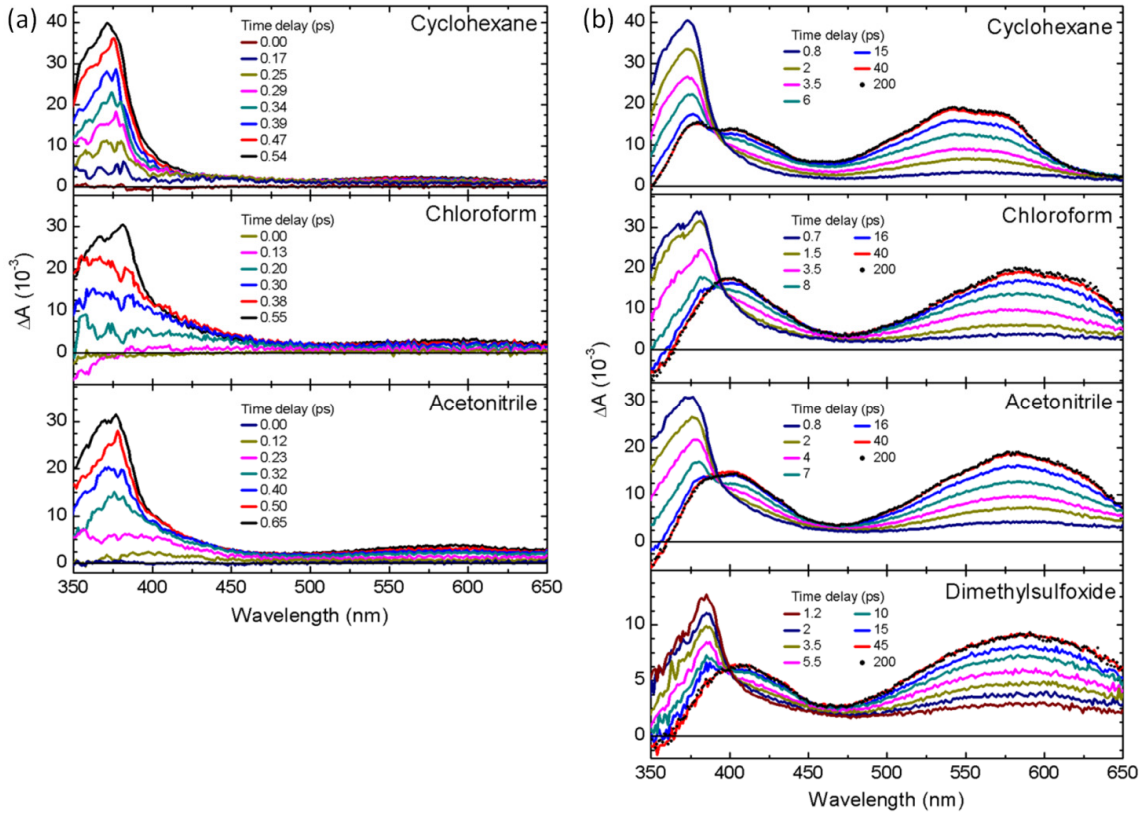

Figure 2.6. Femtosecond transient absorption spectra of 1NN in nonpolar and polar aprotic solvents: (a) short time dynamics and (b) long time dynamics. Note that the transient absorption spectra cease to change after a time delay of ~40 ps.

The changes in the transient absorption spectra of 1NN in polar aprotic solvents are also shown in Figure 2.5 and Figure 2.6. Similar to the nonpolar solvents, three exponentials plus a constant offset are needed to adequately fit the transient absorption dynamics in the femtosecond to three nanosecond time window (Table 2.1). Except for a systematic red shift of the transient absorption bands, the spectral evolution of 1NN in polar aprotic versus nonpolar solvents is quite similar. Initially, an absorption band with a maximum below 400 nm is formed within the time resolution of our experimental setup, which decays with a lifetime between ~2 to 3 ps depending on the solvent used. Absorption bands in

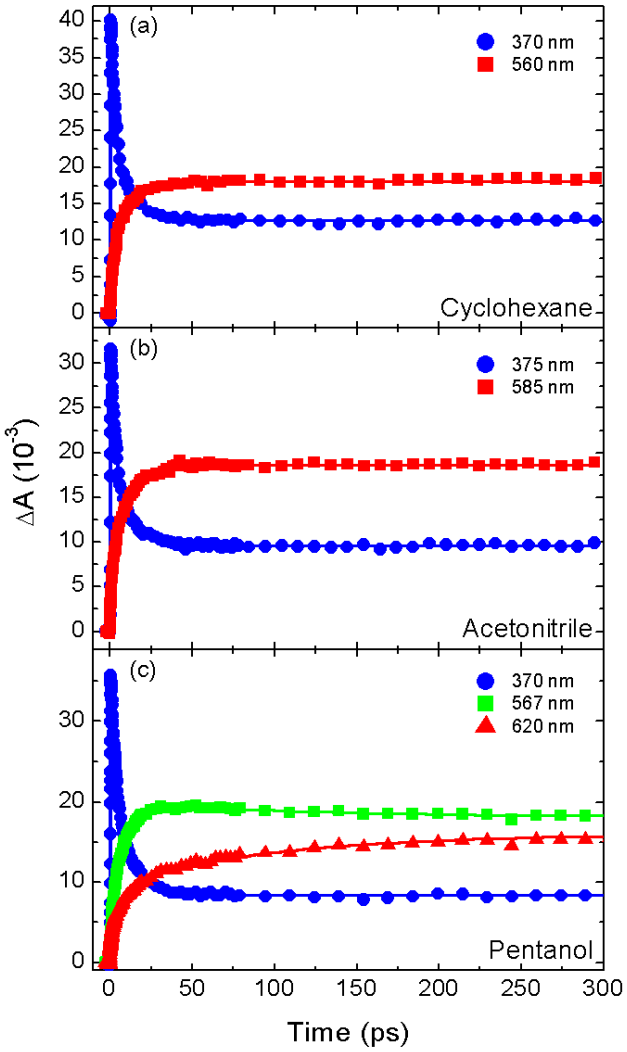

Figure 2.7. Transient absorption signals of 1NN in (a) cyclohexane, (b) acetonitrile, and (c) pentanol at the specified probe wavelengths. Best global-fit curves are shown by solid lines (see text for details).

the visible are formed simultaneously with identical lifetimes (Figure 2.6 and Figure 2.7). In analogy to the spectral evolution observed during the first tens of picoseconds in nonpolar solvents, a blue shift and narrowing of the transient absorption band in the visible are observed in the polar aprotic solvents (Figure 2.5 to Figure 2.8). Depending on the solvent used, the spectral evolution of the

absorption band in the visible is adequately described by a lifetime of 9 to 11 ps (Table 2.1).

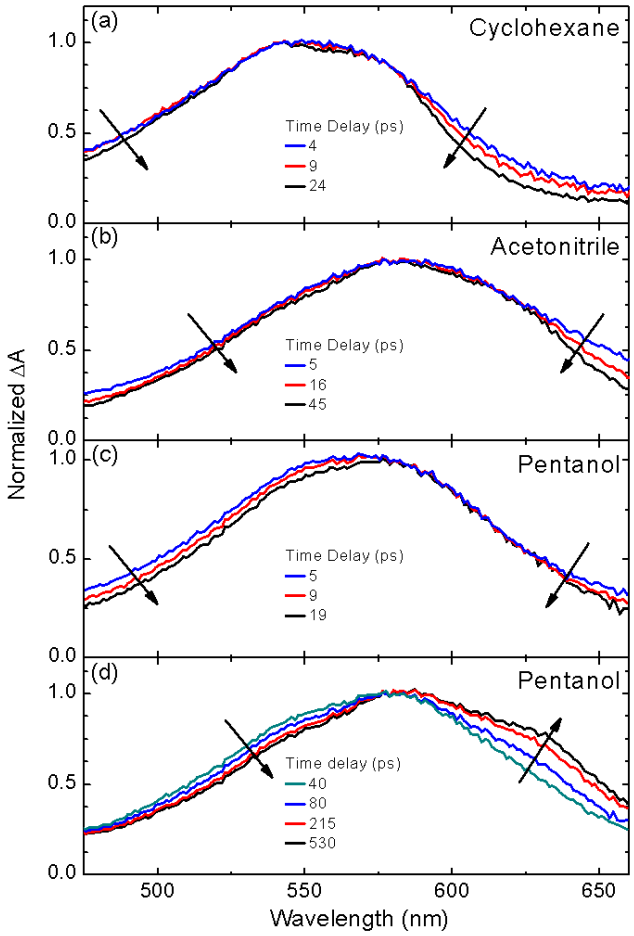

Figure 2.8. Normalized transient absorption spectra of 1NN in (a) cyclohexane, (b) acetonitrile, and (c) pentanol showing the band narrowing and blue shift characteristic of vibrational cooling dynamics. Bottom panel (d) shows the dynamic Stoke shift of the transient absorption band of 1NN in the time delay window of 40 to 530 ps in pentanol solution.

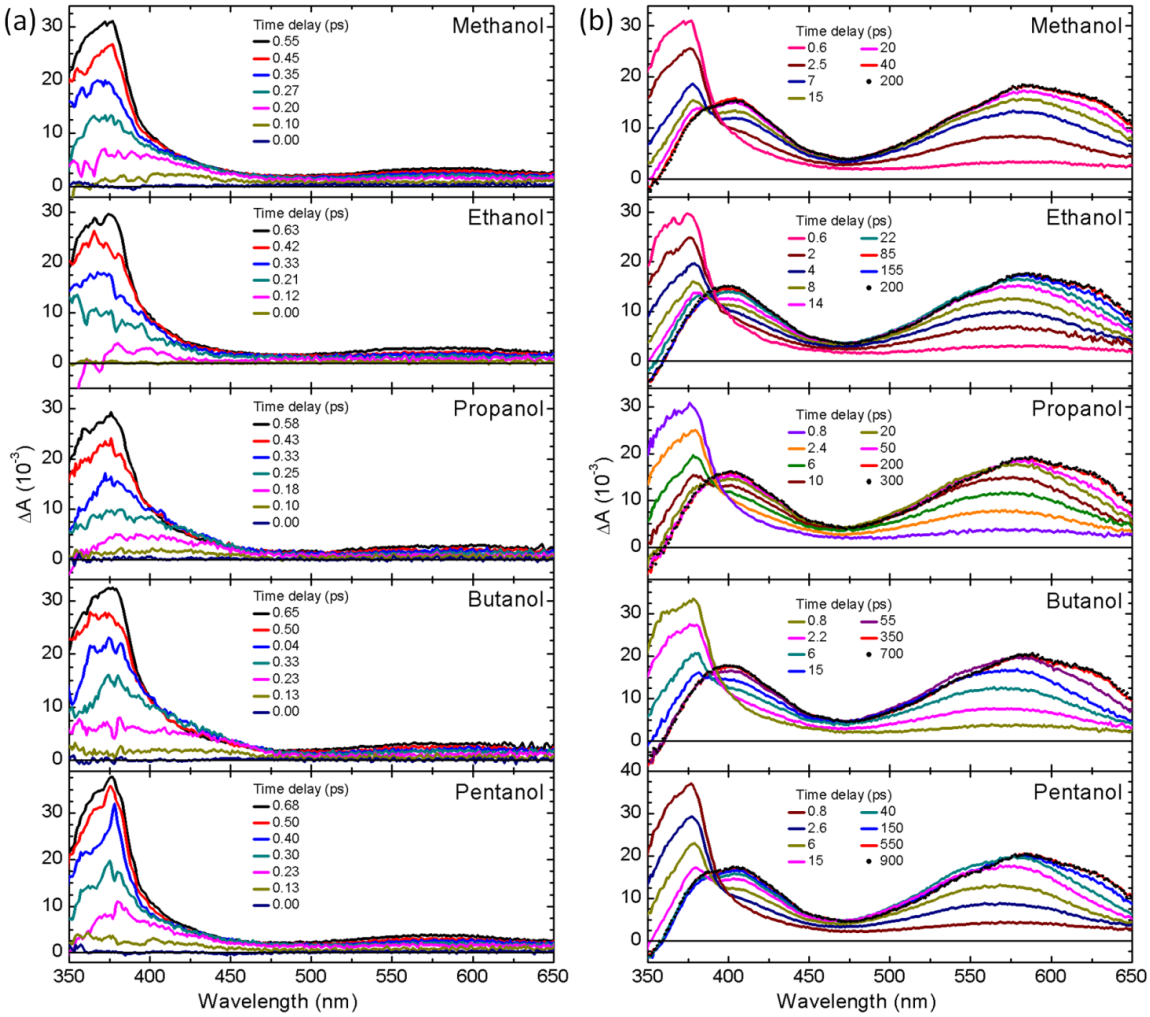

Figure 2.9. Femtosecond transient absorption spectra of 1NN in polar protic solvents: (a) short time dynamics and (b) long time dynamics.

C. Femtosecond broadband Transient Absorption Spectra in Protic Solvents

The ultrafast excited-state dynamics of 1NN was also studied in five primary alcohols that differ in the length of their alkyl chain (Figure 2.5 and Figure 2.9). Four exponentials plus a constant offset are needed to adequately fit the transient absorption signals in the femtosecond to nanosecond time window in these solvents (Table 2.1). Besides the similar spectral evolution observed in all aprotic solvents studied during the first tens of picoseconds, an additional red

shift of the transient absorption band in the visible is observed, with a characteristic lifetimes of ~13 to 97 ps depending of the alcohol used (see Figs. 2.5, and 2.7 to 2.9).

D. Transient Absorption Spectra in the Sub-Nanoseconds to Microseconds Time Window

The changes in the transient absorption spectra of 1NN were also studied in the time window from 400 ps to 30 μs in cyclohexane, acetonitrile, and pentanol solutions. These solvents were selected as representatives of nonpolar, aprotic, and protic solvents. The transient absorption spectra decay completely at delay times of up to 30 μs depending on the solvent used (Figure 2.10). The decay of the transient absorption spectra of 1NN in this time window is satisfactorily described by a monoexponential function in the spectral region from ~ 350 to 700 nm (Figure 2.11). The monoexponential behavior implies that a single transient absorption species is responsible for the temporal evolution. Importantly, the transient absorption spectrum of 1NN is readily quenched by molecular oxygen (Table 2.2). A 5- to 19-fold decrease in the lifetime is observed in air-saturated versus N_2-saturated conditions.

Table 2.2. Lifetimes from global fits to the transient absorption signals from nanoseconds to the microseconds[a]

Solvent	τ_5 (ns) Air-Saturated	τ_5 (μs) N_2-Saturated
Cyclohexane	280 ± 20	1.3 ± 0.1
Acetonitrile	360 ± 40	6.7 ± 0.5
Pentanol	500 ± 40	6.4 ± 0.3

[a] errors are reported as two times the standard deviation of three or more individual global fit measurements.

DISCUSSION

A. Ground-State Calculations in Solvents of Varying Polarity and Hydrogen Bonding Ability

The ground-state geometry of 1NN was optimized in different solvents at the B3LYP/IEFPCM/6-311++G(d,p) level of theory. The nitro-aromatic torsion angle, defined in Figure 2.2, varies slightly from 33.1° in cyclohexane to 34.1° in methanol at this level of theory. A nitro-aromatic torsion angle of 29.9° was obtained when the ground state of 1NN is optimized in the presence of two methanol molecules at the B3LYP/IEFPCM/6-311G(d,p) level of theory. Previous ground-state optimizations of 1NN predicted a nitro-aromatic torsion angle between ~28 to 31.8° depending on the solvent used at the PBE0/6-311G(d,p) level of theory,[41,66] in reasonable agreement with our calculations.

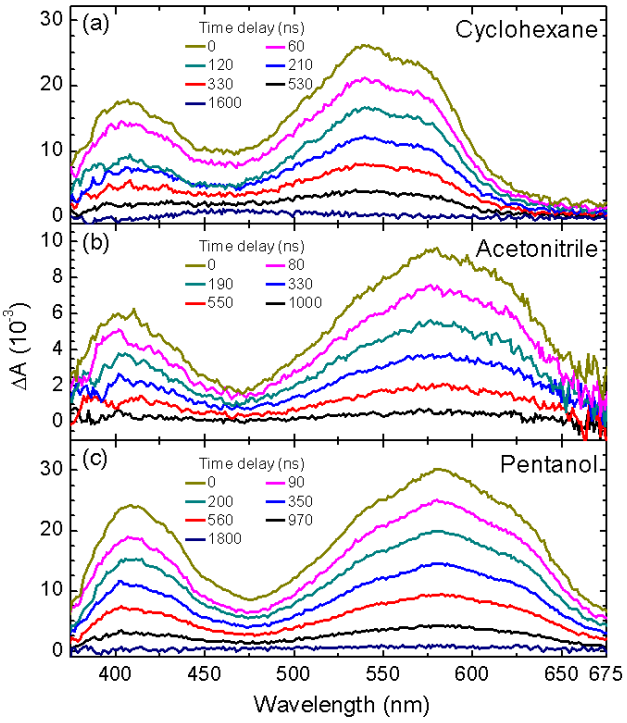

Figure 2.10. Picosecond to microsecond transient absorption spectra of 1NN in (a) cyclohexane, (b) acetonitrile, and (c) pentanol.

Ground- and excited-state potential energy surfaces were estimated using the nitro-aromatic torsion angle as a variable nuclear coordinate in cyclohexane, acetonitrile, and methanol solvents (Figure 2.3). A distribution of nitro-aromatic torsion angles between 0 and ~55° in cyclohexane and acetonitrile lies below k_BT at room temperature. For the *trans* 1NN$(CH_3OH)_2$ complex, a distribution of nitro-aromatic torsion angles between -20 to -40° in methanol solvent are predicted to be accessible at room temperature. Thus, a wide distribution of nitro-aromatic torsion angles is expected to exist at room temperature for 1NN in solution. Importantly, the addition of explicit solvent molecules seems to narrow the distribution of torsion angles accessible in the ground state at room temperature (Figure 2.3c) but the observation would be inconsequential to this chemistry. In agreement with our calculations, shallow ground-state potential energy surfaces have been predicted for other nitro-PAH derivatives in previous gas-phase quantum chemical calculations.[39,64] Clearly, in order to compare the experimental results with the calculations, it becomes necessary to evaluate the vertical excitation energies of 1NN using the full distribution of nitro-aromatic torsion angles available at room temperature. The results of these calculations are presented in the next section.

B. Vertical Excited-State Energies and Singlet-Triplet/Triplet-Triplet Energy Gaps of 1NN in Different Solvents

Table 2.3 shows the vertical excitation energies of the relevant electronic states of the fully-optimized 1NN structure in several solvents. Vertical energy gaps are reported in Table 2.4. Relevant excited electronic states are defined as those accessible by the excitation energies used in this work (3.44 to 3.65 eV). The vertical excitation energy of the S_1 state is stabilized with an increase in the solvent polarity as observed experimentally. The higher stabilization of the S_1 state in methanol, for the *trans* 1NN$(CH_3OH)_2$ complex, compared to aprotic and nonpolar solvents is also in good agreement with the experimental results. The character of the excited states was determined from the effect that the bulk solvent has on the excitation energies and from a molecular orbital analysis of the principal configuration interaction transitions. The S_1 state has 100% $\pi\pi^*$ character in all solvents studied except cyclohexane, where 86% $\pi\pi^*$ and 14% $n\pi^*$ character was obtained. The molecular orbital analysis suggest that on average for all the solvents studied, the T_1 has 85% $\pi\pi^*$ and 15% $n\pi^*$ character; T_2 has 75% $\pi\pi^*$ and 25% $n\pi^*$ character; T_3 has 40% $\pi\pi^*$ and 60% $n\pi^*$ character; and T_4 has 65% $\pi\pi^*$ and 35% $n\pi^*$ character. The effect of the solvent (bulk dielectric constant) on the vertical excited states confirms that the S_1 state has mainly $\pi\pi^*$ character, T_1, T_2 and T_4 have mainly $\pi\pi^*$ character, while T_3 have mainly $n\pi^*$ character. The vertical states have variable percentages of charge transfer character not explicitly shown in the above numbers. These results are in reasonable agreement with previous calculations.[41]

Table 2.3. Vertical excitation energies of the fully optimized 1NN structure in different solvents determined at TD-PBE0/NE-IEFPCM/6-311++G(d,p)//B3LYP/IEFPCM/6-311++G(d,p) level of theory

Solvent	S_1 (eV)	T_1 (eV)	T_2 (eV)	T_3 (eV)	T_4 (eV)
Cyclohexane	3.41	2.34	2.82	3.21	3.48
Chloroform	3.30	2.31	2.87	3. 21	3.41
Ethanol	3.23	2.28	2.91	3.20	3.36
Methanol	3.23	2.28	2.91	3.20	3.36
Acetonitrile	3.23	2.28	2.91	3.20	3.36
Dimethyl sulfoxide	3.21	2.28	2.91	3.20	3.35

Table 2.4. Singlet-triplet and triplet-triplet energy gaps for the fully optimized 1NN structure in different solvents determined at TD-PBE0/NE-IEFPCM/6-311++G(d,p) //B3LYP/IEFPCM/6-311++G(d,p) level of theory

Solvent	$\Delta E_{gap}{}^{a}$ (eV)	$\Delta E_{gap}{}^{b}$ (eV)	$\Delta E_{gap}{}^{c}$ (eV)
Cyclohexane	-0.066	0.202	0.864
Chloroform	-0.105	0.098	0.896
Ethanol	-0.125	0.034	0.920
Methanol	-0.128	0.031	0.920
Acetonitrile	-0.128	0.030	0.921
DMSO	-0.139	0.017	0.922

[a] $\Delta E(S_1 - T_4)$; [b] $\Delta E(S_1 - T_3)$; [c] $\Delta E(T_3 - T_1)$.

Vertical excitation energies were also calculated at fixed nitro-aromatic torsion angles. The percentage of $\pi\pi^*$ and $n\pi^*$ character of the vertical excited states varies with a change in nitro-aromatic torsion angle (not shown). Of particular relevance are those torsion angles that are predicted to be present in the ground state at room temperature. Figure 2.3a,b shows the change in potential energy of the S_1 and T_1 to T_4 excited states as a function of the nitro-aromatic torsion angle in cyclohexane and acetonitrile solutions, while Figure

2.3c shows the change in excited-state potential energies for the *trans* 1NN$(CH_3OH)_2$ complex in methanol. Explicit solute-solvent hydrogen bonding interactions decrease the energy gap of the S_1 and T_3 states relative to that in cyclohexane, making these states effectively isoenergetic to one another. A similar decrease in the energy gap of the S_1 and T_3 states is observed with an increase in solvent polarity (Table 2.4) with energy gap values as small as 0.02 eV in dimethyl sulfoxide (DMSO). It is likely that a distribution of ground-state torsion angles is also present in other nitro-PAHs at the time of excitation,[38,39] as has been recently shown by Mohammed and Vauthey in their study of the excited-state dynamics of 1-nitroperylene.[39]

Invoking El-Sayed's propensity rules,[67] the TD-PBE0/NE-IEFPCM/6-311++G(d,p) calculations suggest that ultrafast intersystem crossing from the S_1 state to the T_3 state should be favorable for most of the distribution of torsion angles present at room temperature in the solvents studied in this work. Ultrafast intersystem crossing from S_1 to T_3 state can explain the sub-100 fs fluorescence lifetimes measured recently for 1NN using the femtosecond fluorescence up-conversion technique.[41] In addition, the relatively large triplet yield of 1NN[36,43] seems to be a consequence of the small energy gap and the strong vibronic coupling between the S_1 and T_3 states in the Franck-Condon region of the S_1 state potential energy surface. The spin-orbit coupling between S_1 and T_3 states is predicted not to change significantly with solvent, as the calculations show that the topology of these states does not change much with solvent. As a consequence, the triplet state yield of 1NN is predicted to remain approximately

constant in the solvents investigated in this work. The predicted insensitivity of the triplet quantum yield to the solvent used is confirmed experimentally (see section F below). In addition, the fluorescence lifetime of 1NN is estimated to be only moderately sensitive to solvent effects (Table 2.1).[41]

Figure 2.3 shows that a fraction of the distribution of torsion angles predicted to be accessible at room temperature can in principle decay through a barrierless relaxation pathway in the S_1 PES that reaches the S_1 state minimum. This conformation has a nitro-aromatic torsion angle of 90°and a C-N bond distance that is elongated by 0.017 Å in acetonitrile (0.009 Å in cyclohexane) relative to the minimum energy ground-state structure. Importantly, this conformation is also predicted to have a zero oscillator strength and a HOMO to LUMO transition with significant charge transfer character[68] where electron density from the sp^2 orbitals of the naphthalene moiety is transferred to the oxygen atoms lone pairs in the nitro-group independent of the solvent used. The apparent insensitivity of this channel to the solvent polarity is somewhat unexpected but in accord with the relative triplet yields estimated below in the different solvents. The accumulation of electron density in the p* orbitals of the oxygen atoms together with the elongation of the C-N bond in going from the Franck-Condon geometry to the conformationally relaxed S_1 structure suggest that this state is formally a dissociative channel in the PES. Even though the participation of this decay channel is expected to be small it can responsible for the photochemistry of 1NN as is argued below.

C. Assignment of the Transient Absorption Spectra at Delay Times Above 200 ps

We begin the discussion of the experimental results by assigning the long-lived transient absorption bands in the 350 to 675 nm spectral region observed after excitation of 1NN at 340 nm. As shown in Figs. 2.10 and 2.11, the decay of transient absorption bands in this spectral region can be satisfactorily described by a monoexponential function at delay times longer than 400 ps independent of the solvent used. The monoexponential behaviour strongly suggests that a single transient species is responsible for the decay of the long-lived transient absorption bands. Importantly, the long-lived transient absorption species is quenched by oxygen; 5- to 19-fold shorter lifetimes are measured in air- versus N_2-saturated solutions (Figure 2.11 and Table 2.2). Consequently, we assign this long-lived species to the T_1 of 1NN. That is, the band with absorption maximum in the visible is assigned to a $T_n \leftarrow T_1$ transition while the band with absorption maximum in the UV is assigned to a $T_m \leftarrow T_1$ transition, for m > n. Previous nanosecond transient absorption experiments have also assigned this long-lived species to the $T_1(\pi\pi^*)$ state,[41,43,45-47] in good agreement with our experimental and computational results. The red-shift of the triplet-triplet absorption bands with an increase in solvent polarity can be explained by an increase in the dipole moment of the T_1 state.

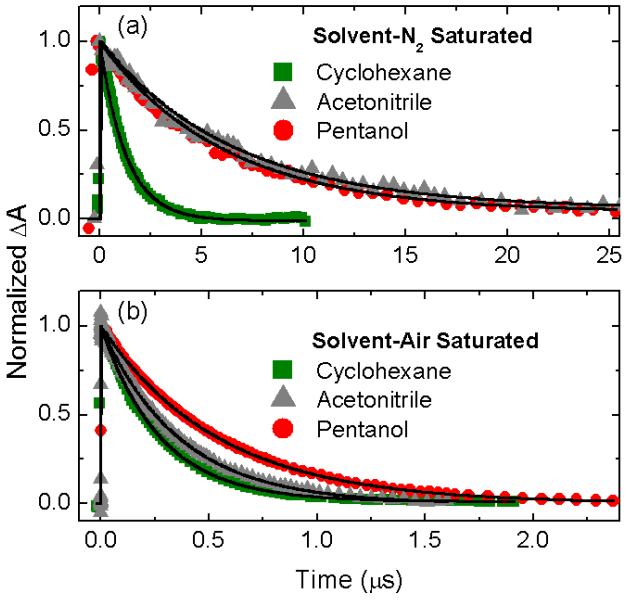

Figure 2.11. Normalized transient absorption signals in the picosecond to microsecond time scale of 1NN in cyclohexane, acetonitrile, and pentanol solvents: (a) in N_2-saturated conditions, and (b) in air-saturated conditions. Best-fit curves are shown by solid lines (see text for details). The reported transient signal is the average of several mono-exponential-decay probe wavelengths.

Table 2.2 shows that the T_1 state decays with a lifetime between 280 to 500 ns and 1.3 to 6.7 μs in air- and in N_2-saturated solutions, respectively. The 280 ± 20 ns lifetime in air-saturated cyclohexane solutions is in good agreement with that measured previously in isopentane.[46] To the best of our knowledge, triplet decay lifetimes in other solvents or in N_2-saturated conditions have not been reported previously. Table 2.2 also shows that the lifetime of the triplet state increases in going from nonpolar solvents to polar solvents. We argue that the slowdown in the decay of the triplet state may be due to an increase in the solvent polarity. An increase in solvent polarity on going from cyclohexane to

acetonitrile solution can stabilize the T_1 state and retard the conformational relaxation needed for efficient intersystem crossing to the S_0 state.

D. Assignment of the Transient Absorption Associated with the Third Lifetime to the Vibrationally-Excited T_1 State

We have shown in the previous section that the long-lived transient absorption spectrum of 1NN can be unequivocally assigned to the T_1 state, which absorbs in the spectral region from 350 to 700 nm. We now turn the attention to the sub-nanosecond excited-state dynamics observed in nonpolar and polar solvents. Figure 2.6b and Figure 2.9b show that the transient absorption spectra of 1NN at delay times longer than ~45 ps are identical to that of the long-lived T_1 state within experimental uncertainties. We postpone the discussion of the actual intersystem crossing rate constant for a later section. Suffice it to mention here that intersystem crossing in 1NN obviously occurs on a sub-nanosecond time scale and that the transient absorption spectrum at delay times of ~45 ps is due to triplet-triplet absorption bands.

Figure 2.8 shows the normalized triplet absorption band ($T_n \leftarrow T_1$) of 1NN in cyclohexane, acetonitrile, and pentanol solutions in the time window from ~1 to 45 ps. As in previous sections, these three solvents are selected as representatives of the other nonpolar, aprotic and protic solvents. A blue-shift and narrowing of the transient absorption band in the visible is observed within ~1 to 45 ps delay times, which is a hallmark of vibrational cooling (VC) dynamics.[69-71] Similar spectral changes during this time window are observed for the band in the visible in the other solvents. Thus, we assign the third lifetime to

intermolecular VC dynamics in the T_1 state. To detect VC in an excited electronic state, a non-equilibrium energy distribution in a given electronic state must be created faster than the time required for relaxation to a lower-energy electronic state. The accumulation of excess vibrational energy in the T_1 state is likely as the process preceding VC takes place with lifetimes of 2 to 4 ps and the T_1 state population does not decay for several tens of nanoseconds (see Table 2.2). Note that intramolecular vibrational energy redistribution in other nitro-aromatic derivatives has been shown to occur on much faster time scales.[65,72]

Although, no clear correlation was found between the physical properties of the solvents used and the observed VC dynamics (see the lifetime τ_3 in Table 2.1), the modulation of VC dynamics previously observed in other solute molecules when using chloroform and methanol as solvent are reproduced in 1NN. An increase in the magnitude of τ_3 is observed for chloroform: a solvent often used to slow down VC dynamics in solute molecules.[65,69,70,73] In addition, the value of τ_3 decreases relative to other nonpolar and polar solvents when methanol is used as a solvent, consistent with the expectation that VC dynamics is strongly accelerated in hydrogen bonding solvents.[71] These general observations lend additional support to the assignment of τ_3 to VC dynamics in the T_1 state of 1NN.

We considered but dismissed the assignment of the kinetic data and the spectral shifts in the ~1 to 45 ps time window to solvent reorientation dynamics based on the following evidence: (i) cyclohexane is considered to be an “ideal”

nonpolar solvent in which the excited solute molecules do not exhibit solvent relaxation effects or Stokes shifts.[74] In the past, cyclohexane has been used as a reference solvent (i.e., gas-phase like behavior) in ultrafast studies aiming at understanding solvation dynamics using solvatochromic probes such as coumarin dyes.[74-76] Continuum dielectric theories for modeling both the static and dynamic aspects of polar and nonpolar solvation dynamics predict zero Stokes shifts in polar solutes when cyclohexane is used as a solvent.[76,77] Thus, it is difficult to explain the temporal and spectral shifts observed in the transient absorption band in the visible (Figs. 2.6 and 2.8) as due to solvent relaxation effects when cyclohexane is used as a solvent. (ii) The bulk solvent dielectric constant and the typical solvation relaxation times[74,76] of the solvents used in this work do not correlate with the τ_3 reported in Table 2.1. (iii) The calculations and experimental results presented in this work can be adequately explained by a kinetic model that invokes vibrational cooling dynamics in the triplet manifold of 1NN (see below). (iv) As discussed in the next section, solvent reorientation dynamics is indeed observed in the T_1 state but only in primary alcohol solvents and at longer time scales.

E. Assignment of the Transient Absorption Spectra Associated to the Fourth Lifetime in Protic Solvents to Solvation Dynamics

In the previous section we have assigned the third lifetime to vibrational energy relaxation in the T_1 state. Strikingly, in protic solvents we are able to identify spectrally and temporally another relaxation process in the triplet manifold of 1NN (Figs. 2.5, and 2.7 to 2.9). A dynamic Stokes shift of the transient absorption band in the visible is observed in all protic solvents, which is

kinetically characterized by lifetimes in the range of ~13 to 97 ps depending on the alcohol used. The lifetime associated with this process systematically increases as the length of the alkyl chain of the alcohol is increased (see Table 2.1). In fact, a linear correlation is obtained between τ_4 and the viscosity of the alcohol used (Figure 2.12a). The red-shifted transient absorption band at late delay times is identical in all the protic solvents studied within experimental uncertainties (Figure 2.9). We assign this temporal and spectral evolution to solvent reorientation dynamics occurring in the first solvation shell of 1NN in the T_1 state. The decay values we obtain for τ_4 are in very good agreement with the characteristic solvation times and the static dielectric constants reported previously for these alcohol solvents (Figure 2.12b,c),[44] further supporting our assignment of this lifetime to solvation dynamics. We argue that the reorientation of the solvent molecules in response to the change in the dipole moment and nuclear coordinates of 1NN in the T_1 state relative to the vertical S_1 state is the main solvent relaxation pathway. The longer the alkyl chain and the higher the viscosity of the alcohol, the longer it takes for a given alcohol molecule to reorient in response to the change in the dipole moment and the nuclear coordinates of 1NN in the T_1 state.

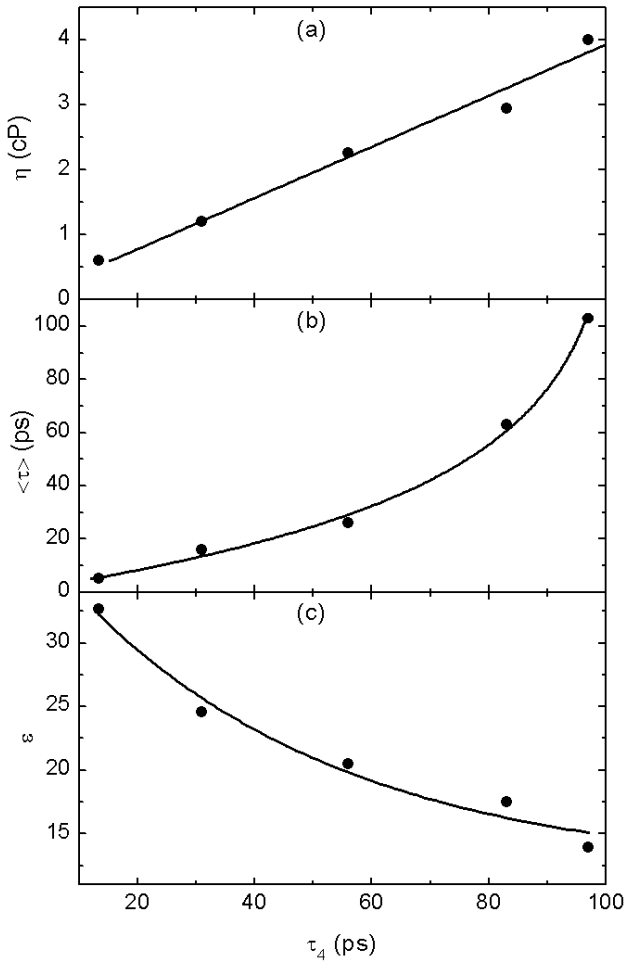

Figure 2.12. Correlation of the fourth time constant of 1NN recorded in primary alcohols (methanol, ethanol, n-propanol, n-butanol, and n-pentanol) as a function of (a) viscosity (η) of the solvent, (b) characteristic correlation times ($<\tau>$) reported in ref. [74], and (c) static dielectric constant (ε). Symbols are connected by solid lines to guide eye.

The dynamic Stokes shift represented kinetically by τ_4 cannot be explained by photoreduction of the T_1 state by hydrogen abstraction from the alcohol. Experiments performed in 2-propanol + 3M HCl conditions, which favour photoreduction of the T_1 state,[78] show the formation of transient absorption bands with spectral signatures significantly different to those associated with τ_4 in pure alcohol solutions.[79] In addition, the initially populated T_1 state decays with a

much shorter lifetime in n-propanol + 3M HCl solutions than in pure n-propanol.[79] Hurley and Testa have shown that the T_1 state of 1NN is practically unreactive towards hydrogen abstraction from 2-propanol (rate constant < 10^2 $M^{-1}s^{-1}$).[43] Thus, in primary alcohol solvents, vibrational cooling and solvent reorganization dynamics in the T_1 state precede intersystem crossing to the ground state of 1NN.

F. Assignment of the UV Transient Absorption Spectra Associated with the τ_1 and τ_2 Lifetimes

Assignment of the kinetics associated to the initial UV absorption band is complicated by the fact that two kinetic models can in principle satisfactorily explain the observed ultrafast dynamics. We therefore begin this section by briefly presenting these models before discussing the existing evidence in support of the kinetic model that best explains the combined experimental and computational results.

In the first model, the UV band formed with a lifetime of sub-200 fs is assigned to intersystem crossing from the S_1 state to a receiver excited T_3 state (Figure 2.13a). Internal conversion from the receiver T_3 state to the T_1 state occurs with a lifetime of ~2 to 4 ps depending of the solvent used, populating the T_1 state with excess vibrational energy. In the second model, the sub-200 fs lifetime is assigned to ultrafast conformational relaxation in the S_1 state (Figure 2.13b). Intersystem crossing to a triplet state then occurs with a lifetime of ~2 to 4 ps populating the vibrationally-hot T_1 state. Thus, in the first model, the evolution of the UV band is assigned to dynamics in an upper triplet state (T_3), while in the

second it is assigned to conformational dynamics in the S_1 state. The rate limiting step in the first model is then slow internal conversion in the triplet manifold, while it is intersystem crossing from the S_1 state in the second.

The main transient absorption and computational results are satisfactorily explained by the first kinetic model. The calculations predict that a distribution of nitro-aromatic torsion angles would be present in the ground state at room temperature at the time of excitation. In particular, the vertical excitation energies of the S_1 and T_3 states are predicted to be practically isoenergetic for most of the distribution of torsion angles. The relatively high triplet state yield reported for 1NN (≥ 0.63)[36,43,48] and the calculated small ($S_1 - T_3$) energy gaps suggest that vibronic coupling between the singlet and triplet manifolds in the vicinity of the Franck-Condon region can be strong for most of these configurations. Thus, the calculations support a relaxation pathway in which τ_1 can be assigned to ultrafast intersystem crossing from the S_1 state to the receiver T_3 state.

To provide further support of the applicability of the first kinetic model to explain the main experimental observations, the relative quantum yield of the T_1 state was estimated. If there is a strong vibronic coupling between the S_1 and T_3 in the vicinity of the Franck-Condon region independent of the solvent used, it would be expected that the triplet yield remains practically constant throughout the series of solvent used. Then, in a sequence of back-to-back measurements, the transient absorption spectrometer was set to a fixed time delay of 600 ps and the transient absorption spectra of the triplet state were recorded from ~450 to 700 nm in all the solvent used in this work. Acquisition times of 30-40 seconds

were used, which is equivalent to approximately 15,000 to 20,000 shots averaged per point. For each solution, the spectrum was integrated over the spectral range between the two points of half maximum transient absorption band of the triplet state. The integrated areas of the triplet-triplet absorption band of 1NN were identical within the estimated experimental uncertainties (15%) in all the solvents. The apparent insensitivity of the triplet quantum yield of 1NN to solvent supports the kinetic mechanism of sub-200 fs intersystem crossing through an essentially barrierless path that connects the initial S_1 to the receiver T_3 state.

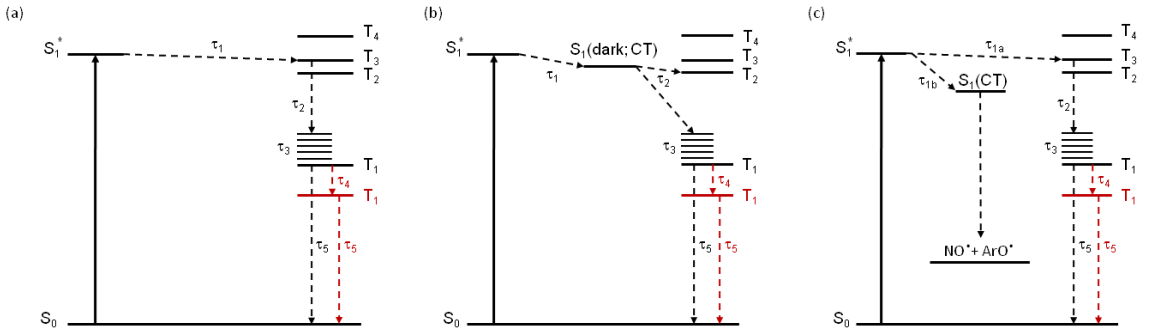

Figure 2.13. Three plausible kinetic mechanisms (a, b, and c) which explain the excited-state dynamics and photochemistry of 1NN in nonpolar, aprotic, and protic solvents. Decay pathways in red describe solvation dynamics and intersystem crossing ($S_0 \leftarrow T_1$) in 1NN observed in primary alcohol solvents. The kinetic model to the right explains satisfactorily the experimental and computational data available to date.

The experimental and computational results also suggest that τ_2 can be assigned to nonradiative internal conversion from the receiver T_3 state to the T_1 state (Figure 2.13a). The larger lifetime obtained for τ_2 in chloroform compared to other solvents suggests that this lifetime is not associated with the intersystem crossing rate in 1NN. This is because a relativistic heavy atom effect is expected

when chloroform is used as a solvent,[35] which is expected to enhance the rate of intersystem crossing instead of slowing it down as experimentally observed (see Table 2.1). Typically, internal conversion from a higher to a lower energy electronic state occurs on ultrafast time scales (Kasha's rule).[35] However, examples do exist of nonradiative internal conversion from upper triplet states to the T_1 state on picoseconds time scales in other naphthalene derivatives.[81] The large energy gap between the T_3 and the T_1 states of ~0.9 eV regardless of the solvent used (Table 2.4), may result in poor Franck-Condon factors for internal conversion.[35] Isoenergetic states are expected to have a large coupling matrix element, whereas electronic states with substantial energy mismatch are generally less efficient for depopulation. It is possible that large conformational changes must occur before an efficient internal conversion process can take place from the receiver T_3 state to the T_1 state. The conformational differences between the receiver T_3 state and the T_1 state, as well as the large energy gap of these states, might conspire to slow down the internal conversion process in the triplet manifold of 1NN. The relatively slow rate of internal conversion in the triplet manifold can thus be a manifestation of the energy gap law of radiationless transition theory.[83]

Zugazagoita et al. have also invoked the argument of a large energy gap between the receiver state and the T_1 state to support a slow internal conversion process in the triplet manifold of 1NN.[42] However, the authors reported time constants for internal conversion as large as 16 ps in the triplet manifold in methanol, which are 4- to 8-fold larger than the lifetime reported in this work. We

think that the apparent disagreement is due to the inability of this previous work to disentangle internal conversion in the triplet manifold from VC and solvation dynamics in T_1 state of 1NN. The experiments presented herein clearly show that solvation dynamics constitute an important relaxation pathway in the triplet manifold of 1NN in primary alcohols.

G. The Possibility of a Branched Electronic Relaxation Pathway

We have shown in the previous section that the main features of the excited-state dynamics in 1NN can be satisfactorily explained by the kinetic model shown in Figure 2.13a. However, this kinetic model fails to explain why the triplet state yield of 1NN is only 63% if the rate of intersystem crossing is as high as 10^{13} s^{-1}. The relatively small triplet yield is particularly puzzling considering that internal conversion from the S_1 to the S_0 state has been suggested to be negligible in this molecule.[38] Thus, another nonradiative decay channel must compete with the intersystem crossing.

The fact that stimulated emission is not observed in the transient absorption experiments suggest that S_1 state dynamics are occurring on a faster time scale than that accessible by our experimental setup. Stimulated emission has been observed in other nitro-aromatic derivatives in less than 100 fs.[65,72] Importantly, conformational relaxation of the nitro-group in several nitro-PAHs[38,40] and in other nitro-aromatic derivatives[65,72] has been proposed as a major nuclear relaxation coordinate in the S_1 state, which occur with a lifetime of < 100 fs. Thus, ultrafast conformational relaxation in the S_1 of 1NN may effectively compete with intersystem crossing to the receiver T_3 state.

Figure 2.3 shows that a fraction of the distribution of torsion angles that are predicted to be available at room temperature can in principle access the dissociative S_1 state through a barrierless relaxation channel from the Franck-Condon region of the PES. This dissociative channel is predicted to have significant charge-transfer character[68] and zero oscillator strength (Figure 2.3). Importantly, the bifurcation of the initial excited-state population to form the dissociative S_1 state is not at variance with the fluorescence up-conversion results of sub-100 fs lifetimes,[41] as this state is expected to be dark in emission. Earlier picosecond transient absorption studies have suggested that the S_1 state may exhibit significant intramolecular charge-transfer character,[48] in agreement with our calculations and calculations by others.[41,45] Thus, we propose a kinetic model where two competitive nonradiative relaxation pathways occur with sub-200 fs lifetimes (Figure 2.13c). This kinetic mechanism merits some additional elaboration.

We shall now define one of the channels that connect the initial S_1 state to the receiver T_3 state by a rate constant k_{1a} and the other relaxation pathway that connects the Franck-Condon state to the dissociative state by k_{1b}. The quantum yields of the two processes, Φ_T and Φ_{diss}, respectively, are given by $\Phi_T = \frac{k_{1a}}{k_{1a} + k_{1b}}$ and $\Phi_{diss} = 1 - \Phi_T = \frac{k_{1b}}{k_{1b} + k_{1a}}$, assuming no other competitive relaxation process depopulates the initial S_1 state. As already mentioned above, $S_0 \leftarrow S_1$ internal conversion in 1NN has been suggested to be negligible.[38] If we

use a triplet yield of 0.63 as a lower bound value, the ratio of k_{1a}/k_{1b} should be ~2.

We expect that the reported fluorescence lifetimes in Table 2.1 reflect a superposition of the two relaxation channels, weighted by the relative quantum yields. Since the decay of the S_1 state population is expected to be dominated by intersystem crossing, it is not surprising that a monoexponential function was fitted to the fluorescence decay signals in 1NN.[41] Importantly, all other nitro-PAHs studied by Peon's group show bi-exponential fluorescence decay lifetimes.[38] In the case of our transient absorption experiments, a close inspection of the data below ~400 nm suggests that the receiver T_n state and the dissociative state (or the aryloxy radical formed from it, see below) contribute to the total absorption signal. Then, similar to the case of the fluorescence up-conversion experiments, the transient absorption signals in the UV are expected to be a superposition of the species produced by both nonradiative channels, weighted by the ratio of their quantum yields as well as by the ratio of their absorption cross sections. It is also important to note that the accuracy of the τ_f and τ_1 lifetimes reported in Table 2.1 are likely to be limited by the instrument response function of the experimental setups, limiting the possibility to extract the precise values of k_{1a} and k_{1b}.

The analysis above suggests that the yield of the dissociative singlet state channel is small (< 37%). However, this channel can be responsible for the observed photochemistry of 1NN in solution (see Figure 2.13c).[79] Two mechanisms have been proposed to explain the formation of nitrogen (II) oxide

(NO) and aryloxy (ArO) radicals in the photochemistry of nitro-PAHs: (1) an intramolecular rearrangement and (2) dissociation-recombination mechanisms.[40,84-87] In the intramolecular rearrangement, a conformational relaxation in the excited state initially occurs where the nitro-group becomes perpendicular to the aromatic moiety of the nitro-PAH. Orbital overlap between the half-occupied, nonbonding *p* orbital of the oxygen atom and an adjacent sp^2 orbital in the aromatic ring leads to an oxaziridine-type transition state, which can collapse to form a nitrite intermediate.[84] In the dissociation-recombination mechanism, reversible homolytic cleavage of the C-N bond leads to the formation of the aryl and nitrogen (IV) dioxide geminate radical pair. The radical pair can recombine to form the aryl nitrite (Ar-ONO) intermediate followed by formation of the NO and ArO radicals. The expected small yield of the ArO radical species and its small absorption cross sections in the UV[85] can explain why this species is not detected in our transient absorption experiments. An alternative $T_n(n\pi^*)$ state has also been suggested to explain the formation of the NO and ArO radicals,[84-86] but we are unable to confirm this relaxation pathway in the present study. Singlet and triplet excited-state optimizations as well as searches for minimum energy paths and conical intersections on the PES are essential to fully map the photochemistry of 1NN and related nitro-PAH compounds. Similarly, time-resolved experiments with higher temporal resolution and wider probe range are likely to provide more insights on the intricate excited-state dynamics and photochemistry of these heteroatomic molecules.

CONCLUSIONS

The excited-state dynamics of 1NN in nonpolar, aprotic and protic solvents was investigated using broadband transient absorption spectroscopy with femtosecond time resolution in combination with ground- and excited-state calculations that include bulk and explicit solvent effects. The results reveal a potential bifurcation of the initial excited-state population in less than 200 fs into two nonradiative decay channels. The first is an essentially barrierless decay path that connects the initial S_1 state to a receiver T_n state. Slow internal conversion of the receiver T_n state leads to the vibrationally-excited T_1 state, which cools down in 6 to 12 ps depending on the solvent used. The second minor channel involves the ultrafast relaxation of the S_1 state to form a dark dissociative state, which is proposed to be partially responsible for the photochemistry of 1NN.

A kinetic model is presented that satisfactorily explains the major experimental and computational results available to date (Figure 2.13c). The ultrafast intersystem crossing indicates a strong vibronic mixing between the S_1 state and the receiver T_n state in the region of the potential energy surface where the crossing occurs. This suggests that a conical intersection may lie along the intersystem crossing decay pathway. In primary alcohols, an additional nonradiative relaxation is observed, which is assigned to solvation dynamics in the T_1 state. The relaxed T_1 state undergoes intersystem crossing back to ground state with a lifetime that is six orders of magnitude smaller than the initial population of the T_1 state in N_2-saturated solutions regardless of the solvent

used. Our results reveal the origin of the ultrafast nonradiative transitions in 1NN and satisfactorily explain why 1NN and other nitro-PAHs have been traditionally considered to be nonfluorescent.

Chapter 3. Role of the Ground State Nitro-Aromatic Torsion Angle on the S_1 State Branching Dynamics and Photochemistry of Nitro-Polycyclic Aromatic Compounds*

ABSTRACT

Femtosecond transient absorption experiments, photodegradation yields, and DFT quantum chemical calculations in the ground- and in the excited-states of three nitronaphthalene derivatives in cyclohexane and acetonitrile solutions are presented. A major aim is to provide insights about the structural-reactivity-relationships in nitro-polycyclic aromatic compounds upon light absorption. Our results lend support to the hypothesis that the photoreactivity of 1-nitronaphthalene, 2-methyl-1-nitronaphthalene, and 2-nitronaphthalene is primarily modulated by the distribution of nitro-aromatic conformations available in the ground state at the time of excitation and by the energy gradient in the Franck-Condon region of the S_1 state leading toward a dissociation channel. Methylation of the ortho position in 1-nitronaphthalene increases the photodegradation yield by 46%; presumably by steering the initial S_1 state population towards the dissociation channel. The experimental and computational results suggest an important link between conformational distribution before light absorption and the photodegradation yield in these nitronaphthalene derivatives.

* This text has been modified from Vogt, R. A.; Reichard; Crespo-Hernández, C. E.;"Role of the Ground-State Nitro-Aromatic Torsion Angle on the S_1 State Branching Dynamics and Photodegradation Yield of Nitro-Polycyclic Aromatic Hydrocarbons", manuscript in preparation.

INTRODUCTION

The time-resolved photochemistry of nitro polycyclic aromatic compounds (nitro-PAHs) has received renewed attention primarily because of their distinctive ultrafast nonradiative dynamics, in particular, the efficient population of the triplet state in yields approaching unity.[38-41,25,42,91-94] Nitro-PAHs have also been identified as persistent organic pollutants in the environment, which can absorb sunlight with the potential of increasing the formation of toxic products.[3,26] Early work has provided evidence that nitro-PAHs containing two to four aromatic rings have vanishingly small fluorescence quantum yields in solution at room temperature.[36,95] More recently femtosecond fluorescence up-conversion and transient absorption experiments in combination with quantum-chemical calculations have shown that the negligible small fluorescence yield is a consequence of ultrafast nonradiative population of one or more decay pathways in the excited states.[38-42,91,94]

Of particular relevance to this work is recent evidence suggesting that the excited-state dynamics of 1-nitronaphthalene (1NN) is primarily controlled by the ground-state distribution of nitro-aromatic torsion angles available at room temperature.[91] Efficient and ultrafast bifurcation of the initial population in the first excited singlet state (S_1) results in intersystem crossing (ISC) to the triplet manifold as a major decay channel and dissociation dynamics as a minor reaction pathway. The photodissociation channel is thought to originate from a direct dissociation-recombination mechanism[88] or from a nitro-nitrite

intramolecular rearrangement mechanism[84] leading to the formation of aryloxy (ArO) and NO radicals.

In this contribution, we extend our initial work on 1NN[91] to investigate the excited-state dynamics of 2-nitronaphthalene (2NN) and 2-methyl-1-nitronaphthalene (2M1NN) in cyclohexane and acetonitrile solutions. Polychromatic light photodegradation yields for 1NN, 2NN, and 2M1NN are also reported to provide new insights about the structural-reactivity-relationships in nitro-PAHs.[96,97] Evidence is provide that the excited-state branching dynamics and photodegradation yields are primarily controlled by the distribution of nitro-aromatic torsion angles in the ground state, which is different in each of the nitronaphthalene derivatives, and by the topology of the S_1 potential energy surfaces in the region of configuration space sampled at the time of excitation.

EXPERIMENTAL AND COMPUTATIONAL METHODS

Chemicals. Cyclohexane (99.9%) was obtained from Fisher Scientific. Acetonitrile (99.6%) was obtained from Acros. Both solvents were used as received. 2NN, 1NN and 2M1NN were obtained from Sigma-Aldrich (99.7%, 99% and 99%, respectively).

The purity of the nitronaphthalene compounds was verified by using high-performance liquid chromatography and fluorescence spectroscopy. None of the nitronaphthalene compounds show fluorescence emission within the sensitivity of the instrument used (Cary Eclipse, Varian, Inc.). In the case of 2NN, a small fluorescence emission was observed after excitation at 340 nm in acetonitrile.

The excitation spectrum of the emitting species did not match the absorption spectrum of 2NN. Hence, we tentatively assign this fluorescence spectrum to an impurity present in very small concentrations (Sigma-Aldrich purity specification for 2NN is 99.7%). Regardless, we decided to re-crystallized 2NN using methanol as solvent. After re-crystallization, a negligibly small fluorescence spectrum was still detected upon 340 nm excitation, suggesting that the fluorescence impurity was not completely removed. Importantly, after careful analysis of the 2NN data, we find no indication that the photodegradation yield and transient absorption experiments for 2NN may be compromised by the presence of this minor impurity. It should be highlighted that 2NN, 1NN and 2M1NN are moderately toxic compounds. Proper safety precautions must be taken at all times to limit health risks.

Ground- and Excited-State Density Functional Calculations. All quantum chemical calculations were performed using the Gaussian 03 suite of programs[52] with the exception of the excited singlet state optimizations that used Gaussian 09.[98] In all calculations, bulk solvent effects were modeled by using self-consistent reaction field calculations (SCRF) with the polarizable continuum model (PCM)[61] with the integral equation formalism (IEFPCM).[62]

Ground-state optimizations were performed using DFT at the B3LYP/IEFPCM/6-311++G(d,p) level of theory.[53,99] The procedure used was similar to the one reported by Reichardt et al.[91] Briefly, a gradient procedure was used starting with the 6-31G(d,p) basis set and increasing in size until the changes in geometry and energy were insignificant. Ground-state bond lengths

converged to within 0.008 Å while nitro-group torsion angles converged to within 0.1 degrees at the B3LYP/IEFPCM/6-311++G(d,p) level of theory. To confirm that the optimized geometries were local minima on the potential energy surface, vibrational frequencies were calculated at the B3LYP/IEFPCM/6-31G(d,p) level of theory. Vertical excitation energies were calculated using the TD-PBE0/IEFPCM/6-311++G(d,p) level of theory,[54] with the gradient procedure described previously.[91] Vertical excitation energies converged to 0.07 eV or better in all cases.

The S_1 state of 2NN, 1NN, and 2M1NN were optimized without any geometry restrictions at the TD-PBE0/IEFPCM/6-311++G(d,p) level of theory using the Gaussian 09 suite of programs.[98] Vibrational frequencies were calculated at the TD-PBE0/IEFPCM/6-31G level of theory to confirm that the optimized geometries were local minima on the S_1 state potential energy surface. Vertical and adiabatic potential energy surfaces were calculated using the nitro-aromatic torsion angle as the variable coordinate by fixing this angle at selected values and allowing all other geometrical parameters in the S_0 or S_1 states to relax. Vertical potential energy surfaces were obtained at the TD-PBE0/IEFPCM/6-311++G(d,p)||B3LYP/IEFPCM/6-311++G(d,p) level of theory. The adiabatic S_1 state potential energy surfaces for 2NN, 1NN, and 2M1NN were calculated by optimizing the S_1 state at the TD-PBE0/IEFPCM/6-311++G(d,p) level of theory, with the exception of the nitro-aromatic torsion angle that was constrained at selected angles. The energy values for these potential energy surfaces, as well as the vertical potential energy surfaces described above, are

reported relative to the ground-state global minimum energy at the same level of theory.

Steady-State Measurements. All steady-state absorbance measurements were performed using a Cary 100 UV/Vis spectrometer (Varian, Inc.). Irradiation experiments were performed using a 150W Xe lamp (Newport-Oriel, Apex Source Arc, source model 66453, lamp model 6255). The wavelength range of 275-375 nm was selected by using a FGUVS11S colored glass filter (Schott). Initial experiments filtered out the IR light using a quartz cell filled with water. However, it was found that filtering the IR had no impact on the results, suggesting that thermal decomposition from IR light absorption emanating from the lamp is insignificant in these molecules. The polychromatic light was focused through a 450 mm lens placed at 5 cm from the front of the lamp source. The sample was placed at 41 cm from the front of the lens. The beam width at the sample was 0.95 cm. Solutions were contained in a 1 cm quartz cuvette (Starna, Inc.) and stirred continuously with a magnetic stir bar (Starna, Inc.) while irradiating to assure that the solutions were homogenous throughout the irradiation volume.

The determination of the polychromatic photodegradation quantum yields requires the measurement of the change in concentration of the nitronaphthalene derivatives with irradiation time. We measured the change in concentration with irradiation time using a HPLC (Shimadzu LC-20AD) with an amide column (Ascentis RP-Amide, 5 μm, 25 cm x 4.6 mm) to separate the parent compounds from the photoproducts. This method was used instead of the traditional

chromophore-loss method, as the former provides more accurate determinations of photodegradation yields.[100,101] Calibration curves were obtained for each nitronaphthalene derivatives using the HPLC. At least 5 data points were used for each of the calibration curves of area under the chromatographic peak versus concentration. An isocratic elution was used with a solvent composition of 80% acetonitrile and 20% water. A photodiode array detector (Shimadzu SPD-M20A) was used to measure the absorbance of the eluting compounds. No degradation was observed for 2NN after a total irradiation of four hours. It was, thus, assumed that 2NN was effectively photo-inert under the low-intensity, continuous irradiation conditions used. Potassium ferrioxalate was used as an actinometer to measure the lamp intensity in photon/s.[102] Polychromatic photodegradation yields were measured in air-saturated conditions using the method recently developed by Dodson et al.[103]

Transient Absorption Measurements. The experimental setup used for this research has been described in detail elsewhere.[91] Briefly, the output of a Quantronix Integra-i/e 3.5 Laser (100 fs FWHM centered at 800 nm) was fed into an optical parametric amplifier (TOPAS, Quantronix/Light Conversion) that generates the femtosecond pulses used for excitation of the samples. The excitation wavelength used was 340 nm. Contributions from other wavelengths in the excitation pulses were removed by a reflective wavelength filter and a Glan-Taylor prism. Data was acquired using a broadband transient absorption spectrometer (Helios, Ultrafast Systems, LLC). The white-light probe pulses were corrected for group velocity dispersion,[51] as described elsewhere.[91] Data

analysis was performed using Igor Pro 6.12 software (Wavemetrics, Inc.) From each data set, nineteen evenly spaced traces were selected between 350 and 650 nm. These traces were fit with a sum of exponentials and a delta function convoluted with a Gaussian shaped response function. The instrument response function was estimated to be 160 ± 50 fs in the above probe spectral region from solvent only scans.

The absorbance used in the transient absorption experiments was 1.0 ± 0.2 for all solutions at 340 nm in a 2 mm optical path length cell. This corresponds to a concentration of approximately $(1.0 \pm 0.1) \times 10^{-3}$ M for 1NN and 2M1NN. The extinction coefficients of 2NN have not been reported in the literature and were not determined in this work due to the small quantity of sample available. We estimate that the concentration of 2NN is similar to that used for the other two derivatives. The probed volume of the samples was continuously renewed using a Teflon coated stir bar and a magnetic stirrer. The samples were replaced with fresh samples if a decrease of 5% in the steady state absorbance solutions were observed. Importantly, no changes in the transient absorption spectra or decay signals were evident in solutions that showed 5% or less decrease in ground-state absorption during the time-resolved experiments. Excitation intensities at the sample were 0.5 μJ in all cases. As shown in Figure 3.1, transient signals deviate from linearity at pump intensities greater than 0.6 μJ under the experimental conditions used in this work. All transient absorption measurements were performed under air-saturated conditions.

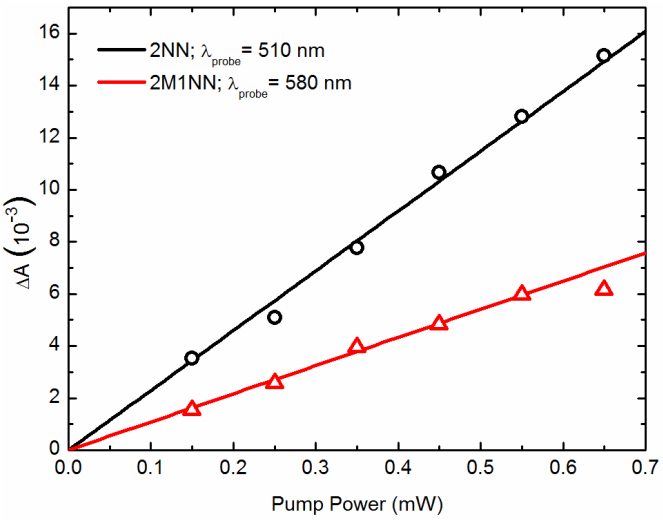

Figure 3.1. Dependence of the triplet transient absorbance of 2NN and 2M1NN in acetonitrile solutions on the pump power. Measurements were taken at a delay time of 500 ps and at the probe wavelengths shown in the legend.

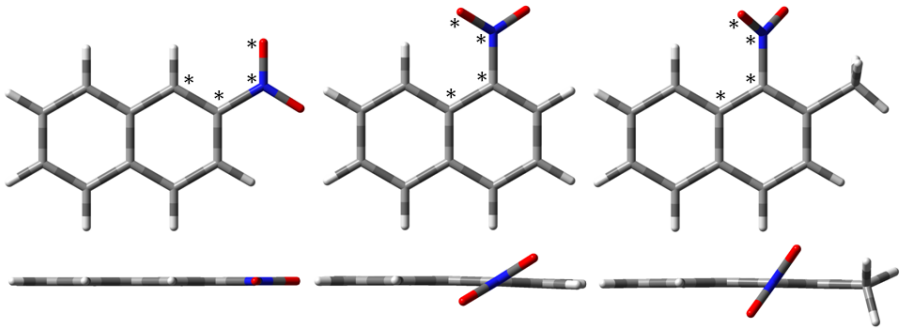

Figure 3.2. Optimized structures of 2-nitronaphthalene (left), 1-nitronaphthalene (center), and 2-methyl-1-nitronaphthalene (right) at the B3LYP/6-311++G(d,p) level of theory. Nitro-aromatic torsion angles are defined with asterisks.

Triplet Yield Measurements. The triplet yield of the nitronaphthalenes in acetonitrile was measured using the energy transfer method with pyrene as the standard.[104] The triplet yield of pyrene is 0.38.[105] Solutions of the nitronaphthalenes with optical density of 0.5 were prepared with various

concentrations of pyrene. The samples were studied using the Eos spectrometer (Ultrafast Systems, LLC). The pump wavelength was 355 nm for the energy transfer experiments. The ratio of the epsilons of the nitronaphthalenes to that of the pyrene was found using

$$A_P = \frac{\varepsilon_P}{\varepsilon_N} A_N \Phi_{ET} \quad (1)$$

were A_P is the maximum absorbance at 412 nm which corresponds to the pyrene triplet, A_N is the maximum absorbance at the triplet peak for the nitronaphthalenes (473 nm for 2NN, 570 for 1NN and 560 for 2M1NN), ε_P and ε_N correspond to the triplet molar absorptivity coefficient for the T_1 state of the pyrene and nitronaphthalene, respectively, and Φ_{ET} is the energy transfer yield from the nitronaphthalene triplet to the pyrene triplet. The energy transfer yield is calculated using

$$\Phi_{ET} = \frac{k_{ET}}{k_{ET} + k_N} \quad (2)$$

where k_{ET} is the rate constant for the energy transfer from the nitronaphthalene to the pyrene and k_N is the rate constant for the decay of the nitronaphthalene without pyrene. The slope from the graph of A_P vs $A_N \Phi_{ET}$ yields the ratio of the epsilons, as shown in Equation 1.

To calculate the triplet yield of the nitronaphthalenes, transient absorption data was collected using a pump wavelength of 334 nm (as opposed to the 355 nm used in the energy transfer portion of the experiment). At this wavelength

both the nitronaphthalenes and the pyrene absorb. Samples of the nitronaphthalenes and the pyrene with an optical density of 0.5 at 334 nm where studied back to back under the same conditions. The triplet yield can be found using

$$\Phi_{T(N)} = \frac{\varepsilon_P}{\varepsilon_N}\frac{A_N}{A_P}\Phi_{T(P)} \qquad (3)$$

where $\varepsilon_P/\varepsilon_N$ is the ratio from Equation 1, $\Phi_{T(P)}$ is the triplet yield of the pyrene and A_N and A_P are the maximum absorbances for pyrene and nitronaphthalenes, respectively.

RESULTS

Quantum Chemical Calculations. Ground-state nitro-aromatic torsion angles, as defined in Figure 3.2, were calculated to be 0.1° for 2NN and 56.8° for 2M1NN in cyclohexane. Changing the solvent to acetonitrile resulted in torsion angles of 0.3° for 2NN and 55.4° 2M1NN. The torsion angle for 2NN is in good agreement with results found in the literature.[66] Experimentally, a similar trend for the torsion angles is predicted using UV/Vis, mass and H-NMR spectroscopic techniques.[96] Figure 3.3 also shows that there is a distribution of torsion angles in the ground state in both 2NN and 2M1NN at room temperature, as observed previously in 1NN.[91]

Vertical excitation energies were calculated using the ground-state optimized geometries. The vertical transition energies and the energy gaps between the excited states are shown in Table 3.1.

Table 3.1. The vertical potential energy surfaces generated from ground-state optimized geometries using the nitro-aromatic torsion angle as the variable coordinate are shown in Figure 3.3. In both nitronaphthalene derivatives, the S_1 oscillator strength has a minimum value at a nitro-aromatic torsion angle of 90°, as previously found in 1NN.[91] The S_1 state of the three nitronaphthalene derivatives is almost isoenergetic with the T_3 state, independent of the solvent used. In the case of 2NN, the S_1 state has a minimum energy at 0°, while the S_1 state of 1NN[7] and 2M1NN has a minimum energy at ~90°. A similar trend is seen for the optimized S_1 state potential energy surfaces when using the nitro-aromatic torsion angle as reaction coordinate (Figure 3.5). These results are in excellent agreement with the fully-optimized S_1 state geometries presented in Figure 3.6 at the same level of theory.

Table 3.1. Vertical excitation energies and selected energy gaps in electron volts obtained from the fully-optimized ground-state structures determined at TD-PBE0/IEFPCM/6-311++G(d,p)||B3LYP/IEFPCM/6-311++G(d,p) level of theory. Oscillator strengths are shown in parentheses.

	Cyclohexane			Acetonitrile		
State	1NN[91]	2M1NN	2NN	1NN[91]	2M1NN	2NN
$S_1(\pi\pi^*)$	3.41 (0.133)	3.28 (0.051)	3.40 (0.093)	3.23 (0.132)	3.09 (0.054)	3.16 (0.089)
$T_1(\pi\pi^*)$	2.34	2.44	2.40	2.28	2.38	2.30
$T_2(n\pi^*)$	2.82	2.79	3.27	2.91	2.85	2.86
$T_3(n\pi^*)$	3.21	3.10	3.27	3.20	3.04	3.14
$\Delta E(S_1\text{-}T_3)$	0.202	0.179	0.136	0.030	0.043	0.021
$\Delta E(T_3\text{-}T_1)$	0.864	0.665	0.868	0.921	0.659	0.841

The predicted excitation energy and oscillator strength (in parentheses) of the fully-optimized S_1 state for 1NN, 2M1NN, and 2NN in acetonitrile are 1.63 (0.0001), 1.60 (0.0000), and 2.67 (0.1241) eV, respectively, at the PBE0/IEFPCM/6-311++G(d,p) level of theory. The corresponding values for 1NN, 2M1NN, and 2NN in cyclohexane are 1.73 (0.0001), 1.67 (0.0000), and 2.93 (0.0724) eV, respectively. The magnitude of energy values obtained from these calculations maybe underestimated due to the significant charge transfer character of the S_1 state. It is known that TD-DFT functional and without asymptotic corrections can underestimate the excitation energies of charge transfer states.[106-108] Thus, caution is suggested in avoiding over interpretation of these results. We note, however, that optimization of the S_1 state minimum of 1NN in acetonitrile using configuration interaction singles (CIS) results in a similar geometry to that predicted by the TD-DFT calculations (Figure 3.5), where the nitro-group is out-of-plane and has a pyramidal conformation. This latter calculation suggests that the structural parameters are less sensitive to the charge transfer character of the S_1 excited states.

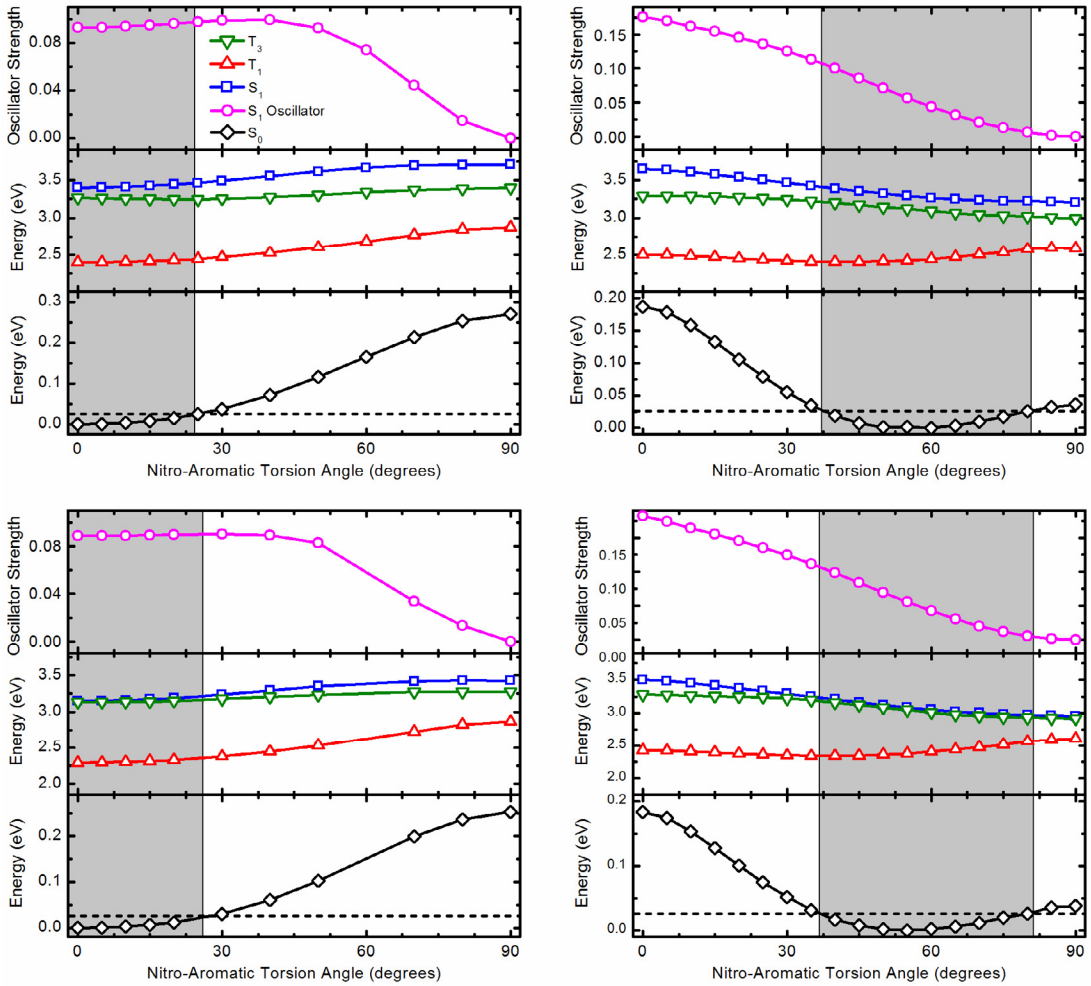

Figure 3.3. Potential energy scans for 2NN (left panel) and 2M1NN (right panel) as a function of the nitro-aromatic torsion angle in cyclohexane (top) and acetonitrile (bottom). The torsion angles distribution populated at room temperature is highlighted in gray. Vertical excitation energies were calculated at the TD-PBE0/IEFPCM/6-311++G(d,p) level of theory following ground-state optimizations at the B3LYP/IEFPCM/6-311++G(d,p) level of theory in each solvent. The nitro-aromatic torsion angle was constrained to the specified values during the ground-state optimizations.

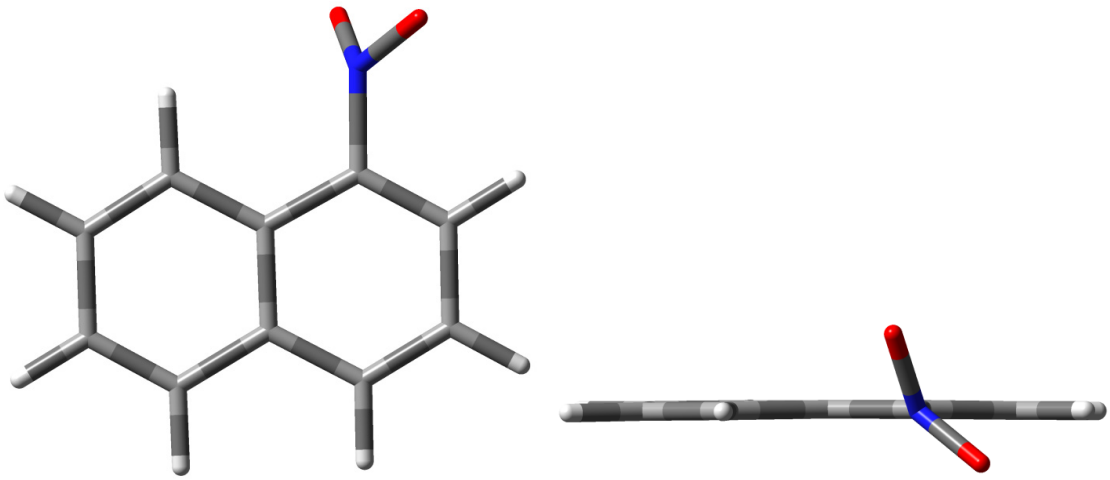

Figure 3.4. Optimized S_1 state geometry of 1NN in acetonitrile at the CIS/IEFPCM/6-31+G(d,p) level of theory. Nitro-aromatic torsion angle, as defined in Figure 3.2, equal to 75°. Note the pyramidal configuration of the nitro-group. The estimated transition energy and oscillator strength at this level of theory are 3.22 eV and 0.0083, respectively.

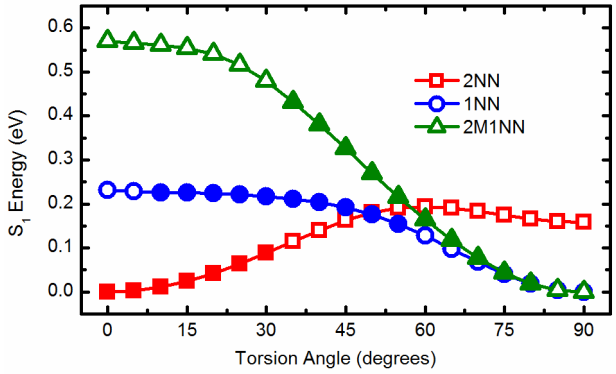

Figure 3.5. Potential energy scans of the optimized S_1 state as a function of the nitro-aromatic torsion angle for 2NN, 1NN, and 2M1NN in acetonitrile at the TD-PBE0/IEFPCM/6-311++G(d,p) level of theory. Filled symbols represent the torsion angles distribution populated in the ground state at room temperature for each molecule.

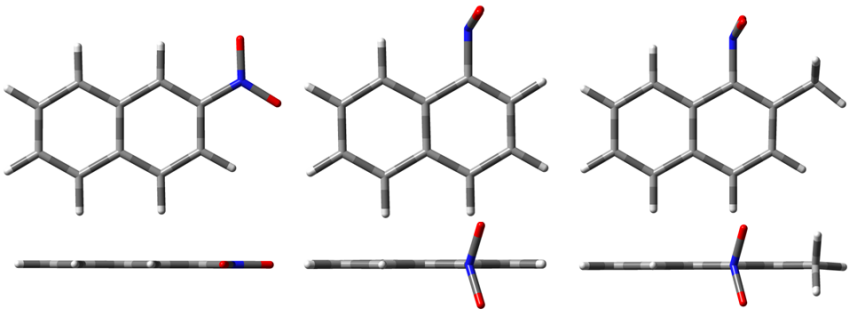

Figure 3.6. Optimized S_1 state structures for 2NN (left), 1NN (center), and 2M1NN (right) in acetonitrile at the TD-PBE0/IEFPCM/6-311++G(d,p) level of theory.

Steady-State Experiments. The ground-state absorption spectra for 1NN, 2NN, and 2M1NN in cyclohexane and acetonitrile are shown in Figure 3.7. A red shift is seen in the lowest-energy absorption band when going from cyclohexane to acetonitrile suggesting that the S_1 state has $\pi\pi^*$ character; in agreement with the calculations. Similar results were obtained for 1NN in a variety of solvents.[41,91] In addition, polychromatic photodegradation quantum yields were determined for 1NN, 2NN, and 2M1NN in acetonitrile solutions (Figure 3.8). The photodegradation quantum yield is largest in 2M1NN and smallest in 2NN, with the value for 1NN lying between the two.

Femtosecond Transient Absorption. Transient absorption experiments were used to measure the evolution of the excited states of the 2NN and 2M1NN in cyclohexane and acetonitrile solutions. The transient spectra of 2NN in cyclohexane are shown in Figure 3.9 (upper left panel). An instrument-response limited rise appears with peak amplitude at ~390 nm after excitation by 340 nm light. Following this fast rise is a broad increase of transient absorption centered at ~450 nm. As this band appears, it becomes more structured showing

vibrational peaks at 392 nm, 432 nm and 458 nm as shown in Figure 3.10. Decay traces and best-global fit curves are shown in Figure 3.11 (A and B).

The excited-state dynamics of 2NN in acetonitrile is similar to that in cyclohexane with a few exceptions (Figure 3.9 upper right panel). At early times, two bands with absorption maxima around 390 and 630 nm rise simultaneously. After few hundreds of femtosecond, these absorption bands seem to level off while a wide absorption band develops with maximum around 450 nm. At longer delay times, the band at 450 nm becomes more structured, showing vibronic bands at ~400 and 465 nm and a shoulder at ~495 nm.

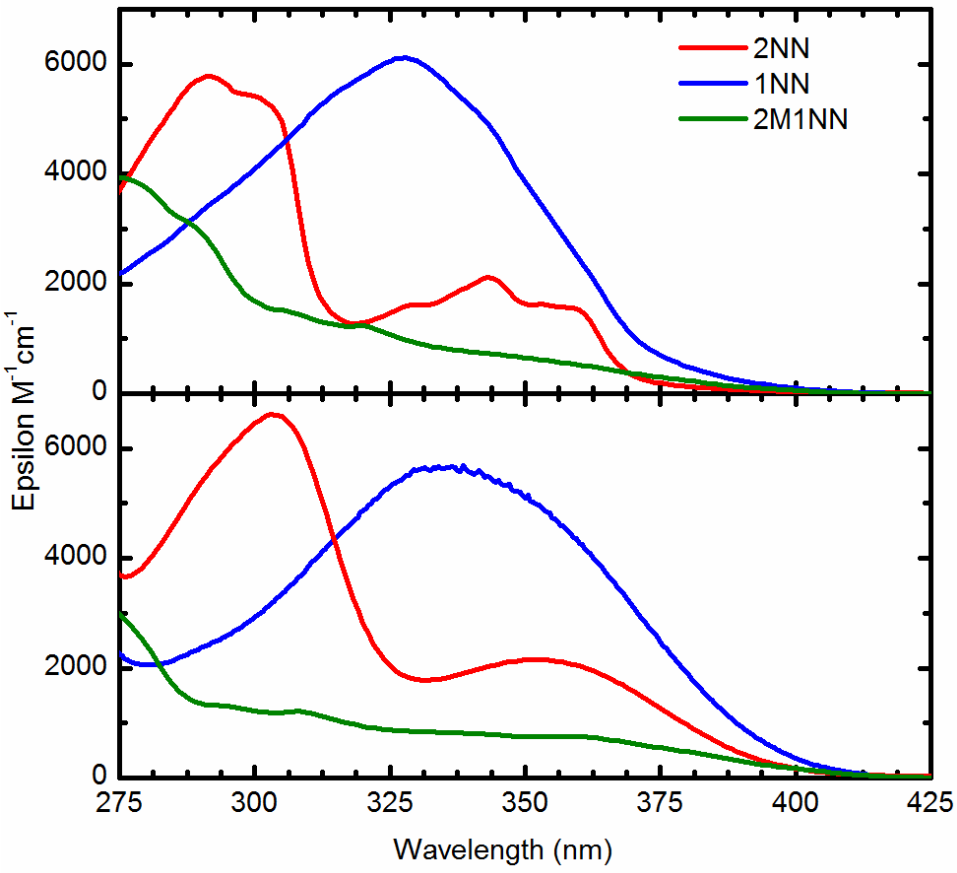

Figure 3.7. Steady-state absorption spectra of 2NN, 1NN, and 2M1NN in cyclohexane (top) and acetonitrile (bottom).

Figure 3.9 also shows transient absorption spectra of 2M1NN in cyclohexane (lower left panel) and acetonitrile (lower right panel) solutions. The excited-state dynamics of 2M1NN begins with an instrument-response limited rise with peak absorbance at ~375 and ~385 nm in cyclohexane and acetonitrile, respectively, and low-amplitude absorption above 500 nm. The UV band decays as a visible band rises in with maxima at 413 nm and 568 nm in cyclohexane and 420 nm and 590 nm in acetonitrile. At longer delay times, the visible bands become more structured and undergo blue shifts as shown in Figure 3.10. Decay traces and best-global fit curves are shown in Figure 3.11 (C and D).

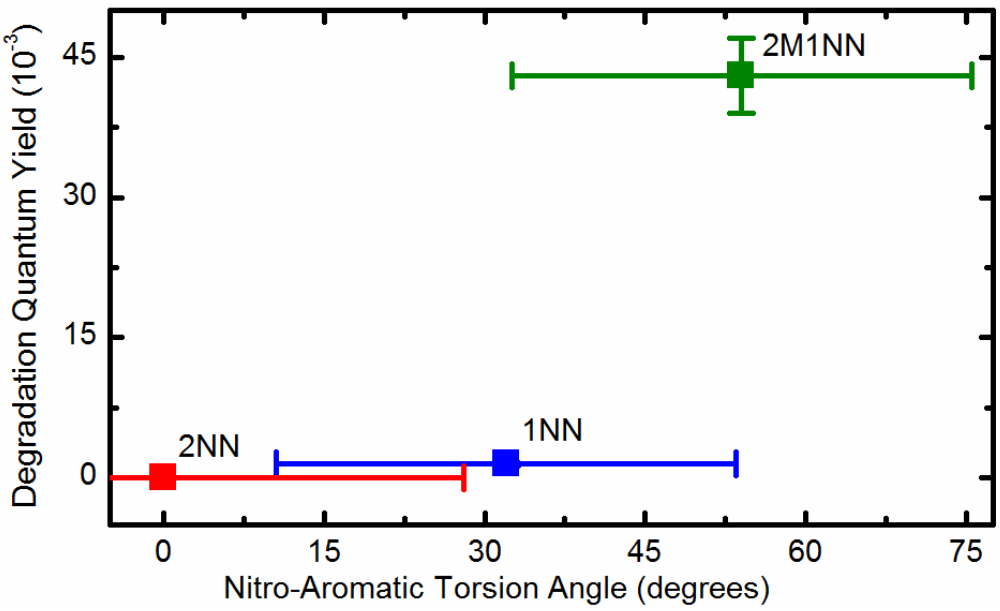

Figure 3.8. Photodegradation quantum yield for 2NN, 1NN, and 2M1NN as a function of torsion angles. Vertical bars represent the uncertainty of the photodegradation yields from three independent measurements. Horizontal bars represent the calculated distribution of torsion angles available at room temperature for each molecule. The squares show the torsion angle of the fully-optimized ground-state minimum structure in each molecule.

The excited-state dynamics of 1NN in cyclohexane and acetonitrile were discussed in detail in our previous work.[91] The evolution of 1NN following excitation at 340 nm is similar to that of 2M1NN and 2NN. Briefly, following excitation, an instrument-response limited rise occurs in both solvents used. The UV band then decays as a visible band rises in with maxima at 378 nm, 402 nm and 554 nm in cyclohexane and 401 nm and 578 nm in acetonitrile. As these bands rise in, they narrow and shift towards the blue side of the spectrum.[91]

Triplet Yield Measurements. The triplet yields for the nitronaphthalenes in acetonitrile are 0.93 ± 0.15, 0.64 ± 0.12 and 0.33 ± 0.05 for 2NN, 1NN and 2M1NN, respectively.

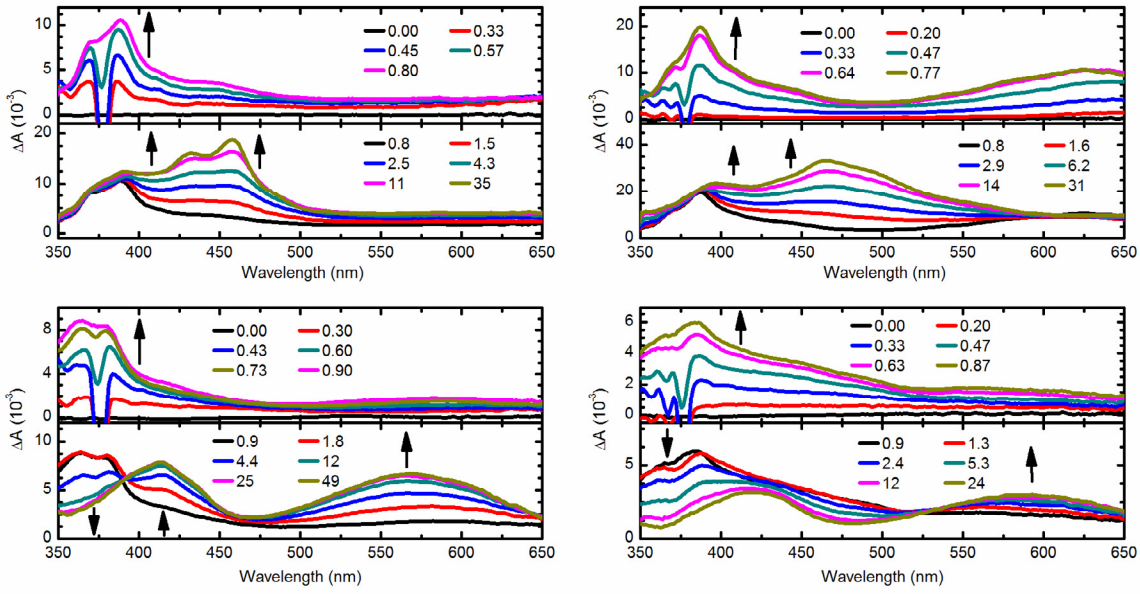

Figure 3.9. Transient absorption spectra of 2NN (top) and 2M1NN (bottom) in cyclohexane (left) and acetonitrile (right). Solvent stimulated Raman emission bands are observed at short time delays.

DISCUSSION

Assignment of the Transient Absorption Bands in 2NN and 2M1NN. We have recently investigated the excited-state dynamics of 1NN in a variety of nonpolar, polar aprotic, and polar protic solvents.[91] Excitation of 1NN with 340 nm laser pulses results in the population of the S_1 state that bifurcates in less than 200 fs to two different decay channels (τ_1, Table 3.2). The major channel is ultrafast population transfer to the triplet manifold, which is proposed to be mediated by intersystem crossing to an upper triplet state (T_3) with significant $n\pi^*$ character.[91] The receiver $T_3(n\pi^*)$ state decays by an anomaly slow internal conversion process (τ_2, Table 3.2) to the lowest-energy triplet state $T_1(\pi\pi^*)$, due partially to a large $T_3 - T_1$ energy gap of close to 1 eV.[42,91] The T_1 state is populated with excess vibrational energy and relaxes by transferring energy to the solvent with an average vibrational cooling lifetime of 9 and 10 ps in acetonitrile and cyclohexane (τ_3, Table 3.2), respectively. The second minor channel is dissociation in the S_1 state, presumably through a dissociation-recombination mechanism (see below),[88,91,92] to form the aryloxy (ArO) and the NO radicals. The latter channel is thought to be responsible of the observed photochemistry in 1NN in nonpolar and polar aprotic solvents.[91]

Table 3.2. Lifetimes obtained from a global fit analysis to the transient absorption data. Errors are reported as twice the standard deviation of three or more individual global fit measurements.

	Cyclohexane			Acetonitrile		
Lifetime / ps	1NN[91]	2M1NN	2NN	1NN[91]	2M1NN	2NN
τ_1	0.11 ± 0.05	0.37 ± 0.07	0.11 ± 0.05	0.14 ± 0.05	0.21 ± 0.05	0.17 ± 0.05
τ_2	2.3 ± 0.2	1.4 ± 0.3	2.1 ± 0.1	2.8 ± 0.2	0.6 ± 0.1	1.9 ± 0.1
τ_3	10.3 ± 0.3	7.1 ± 0.9	10 ± 1	11.2 ± 0.4	5.9 ± 0.3	9.1 ± 0.1

The transient absorption results reported in this work for 2NN and 2M1NN can be satisfactorily explained using the kinetic model previously postulated for 1NN in the same solvents.[91] As in 1NN, very little to no fluorescence emission is observed in 2NN and 2M1NN. This leaves three possible significant channels for relaxation from the S_1 state: nonradiative decay to the ground-state, ultrafast intersystem crossing to the triplet manifold, and product formation directly from the S_1 state. Neither Peon's group[38,41,42] nor our group[40,91] has been able to obtain experimental evidence of ultrafast internal conversion to the ground state in several small nitro-PAHs, including the nitronaphthalene derivatives studied in this work. However, the triplet yield of 1NN and 2NN has been reported to be 0.63 and 0.82, respectively.[43,44] Which is in good agreement with our measurements of 0.93 ± 0.15 for 2NN, 0.64 ± 0.12 for 1NN and 0.33 ± 0.05 for 2M1NN in acetonitrile. Thus, ultrafast intersystem crossing should be the main relaxation pathway, while product formation directly from the S_1 state might also play a role (see below). Hence, in accord with previous works for 1NN,[42,91] the initial rise in the transient absorption spectra in Figure 3.9 is assigned to the population of the receiver $T_3(n\pi^*)$ state, which decays by internal conversion to populate the hot $T_1(\pi\pi^*)$ state (Figure 3.9 and Figure 3.10). We note that 2M1NN shows a faster, average vibrational cooling lifetime than 1NN and 2NN (τ_3, Table 3.2). This is likely a consequence of the methyl group, which lends extra degrees of vibrational freedom.

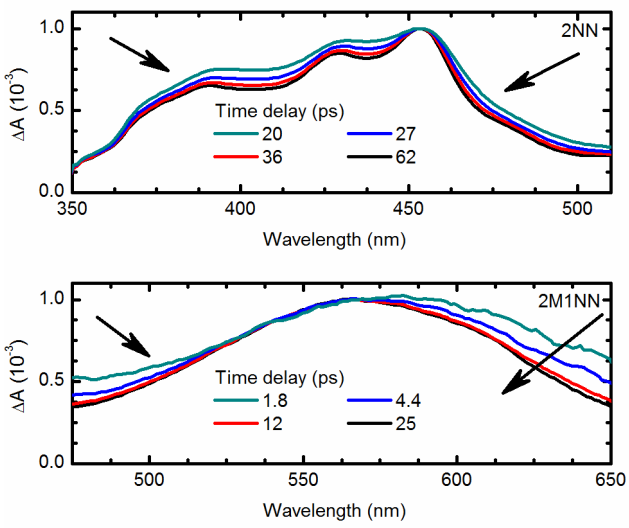

Figure 3.10. Normalized transient absorption spectra of 2NN and 2M1NN at the shown delay times. Arrows highlight the band narrowing and blue shifting characteristic of vibrational cooling dynamics.

In addition, the population in the $T_3(n\pi^*)$ state decays with a lifetime in the 0.6 to 2.8 ps time range in these nitronaphthalene derivatives, which correlates with the energy gap between the T_3 and T_1 states reported in Table 3.2. This is in accord with the energy gap law for nonradiative decay,[82,109] as proposed previously for 1NN.[91]

Interestingly, and in analogy with previous investigations with 1NN,[42,91] we are unable to detect the spectral signature of the initially populated S_1 state. There are two possible explanations for this observation. The S_1 excited state absorption lies outside of the spectral probe region monitored in this work or the decay time of the S_1 state is too fast to be detected within our instrument time resolution.

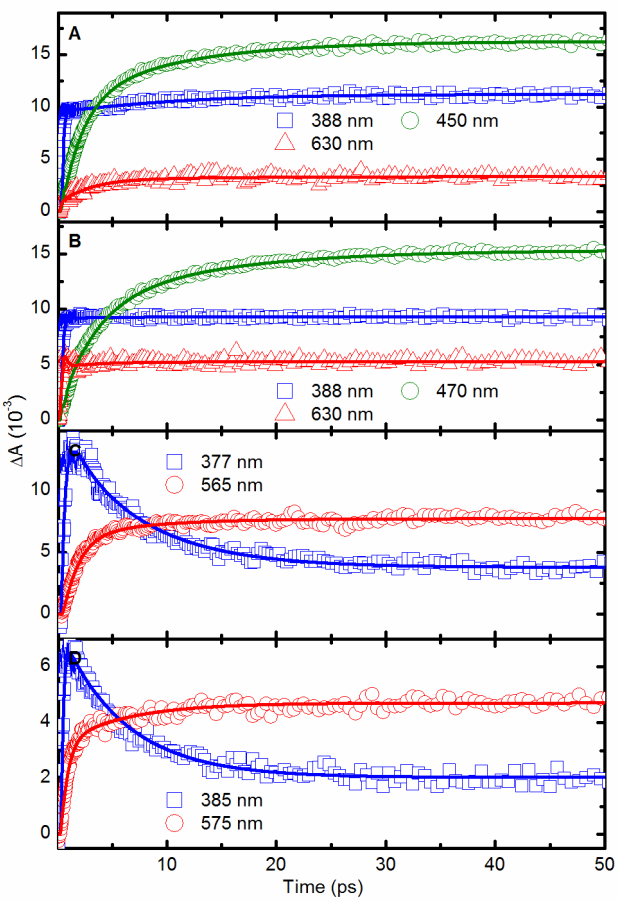

Figure 3.11. Representative decay traces at selected probe wavelengths for 2NN and 2M1NN in cyclohexane (A and C, respectively) and acetonitrile (B and D, respectively). Solid lines represent the best global-fit curves to the transient absorption data.

Correlation between the Ground-State Distribution of Torsion Angles and the Steady-State and Time-Resolved Photochemistry of the Nitronaphthalene Derivatives. Previous investigations have provided compelling evidence that the nitro-aromatic torsion angle plays an important role in the time-resolved[3,25,36-41,91,93,85-87] and steady-state[3,36,84,92,93,96] photochemistry in nitro-PAHs. However, there is ongoing debate about the mechanism by which the nitro-aromatic torsion angle modulates the excited-state dynamics and photochemistry in these molecular systems. In a recent investigation using 1NN

as a model system,[91] we presented evidence that a distribution of nitro-aromatic torsion angles exists in the ground-state at room temperature. It was proposed that this ground-state distribution plays a key role in modulating the extent to which the population in the S_1 state bifurcates toward the dissociative or the intersystem crossing decay channels.[91]

In this work, 2M1NN and 2NN were selected to further evaluate this working hypothesis. Our strategy relies on the premise that the probability of ultrafast branching in the S_1 state is controlled by the topology of the potential energy surface in the Franck-Condon region of the S_1 state that it is accessed by the distribution of torsion angles available in the ground state at the time of excitation. This distribution of torsion angles in the ground state can be shifted toward close to 0 or 90 degrees by a change in the position of the nitro-group or by ortho substitution of a methyl group, respectively, as shown in Figure 3.2 and Figure 3.3. In particular, the ground-state optimizations show that the nitro-aromatic torsion angle increases from 0.1° (0.3°) in 2NN to 56.8° (55.4°) in 2M1NN in cyclohexane (acetonitrile); with 1NN showing an intermediate torsion angle of 33.1° (33.9°)[91] at the B3LYP/IEFPCM/6-311++G(d,p) level of theory. The torsion angle is affected by electrostatic forces acting between the lone pairs of oxygen atoms on the nitro-group and their neighboring atoms on the naphthalene moiety. In the case of 1NN, a *peri* hydrogen atom forces the torsion angle away from 0°.[91] As shown in Figure 3.2, a methyl-group in the ortho position in addition to a *peri* hydrogen atom in 2M1NN forces the torsion angle to

even greater values. 2NN does not have *peri* hydrogen atoms that can interact with the nitro-group, which explain its almost planar conformation.

As previously reported for 1NN,[91] the ground-state calculations predict that a distribution of torsion angles with energies lower than the thermal energy (k_BT) is accessible at room temperature in 2NN and in 2M1NN (Figure 3.3). To our expectation, a correlation is found between the location of the calculated torsion angle distribution in the ground state and the experimentally-measured photodegradation yield in acetonitrile; with 2M1NN showing the highest yield and 2NN being practically photo-inert (Figure 3.9). This result suggests that there is a link between the distribution of torsion angles in the ground state (i.e., the region of configuration space accessed in the S_1 state upon light absorption) and the photodegradation yield in these nitronaphthalene derivatives.

Our results support the kinetic model originally developed for 1NN[91] where excitation of 2M1NN, which has a ground-state distribution of nitro-aromatic torsion angles closer to 90°, results in an increase in population transfer toward the dissociation channel while excitation of 2NN, which has a distribution of torsion angles closer to 0°, results in an increase in population transfer toward the triplet manifold (Figure 3.5 and Scheme 3.1). Even though it is evident that different molecules should have different photochemistry, our experimental and computational results suggest that methylation of 1NN in the ortho position increase the photodegradation yield by 46% in 2M1NN as result of steering of the initial population in the Franck-Condon region of the S_1 state towards the dissociation channel. This is because, with the exception of the ground-state

distribution of torsion angles and the slope of the S_1 potential energy surface in the Franck-Condon region (Figure 3.3 and Figure 3.5), the electronic structure of 1NN is not perturbed significantly upon methylation of the ortho position.

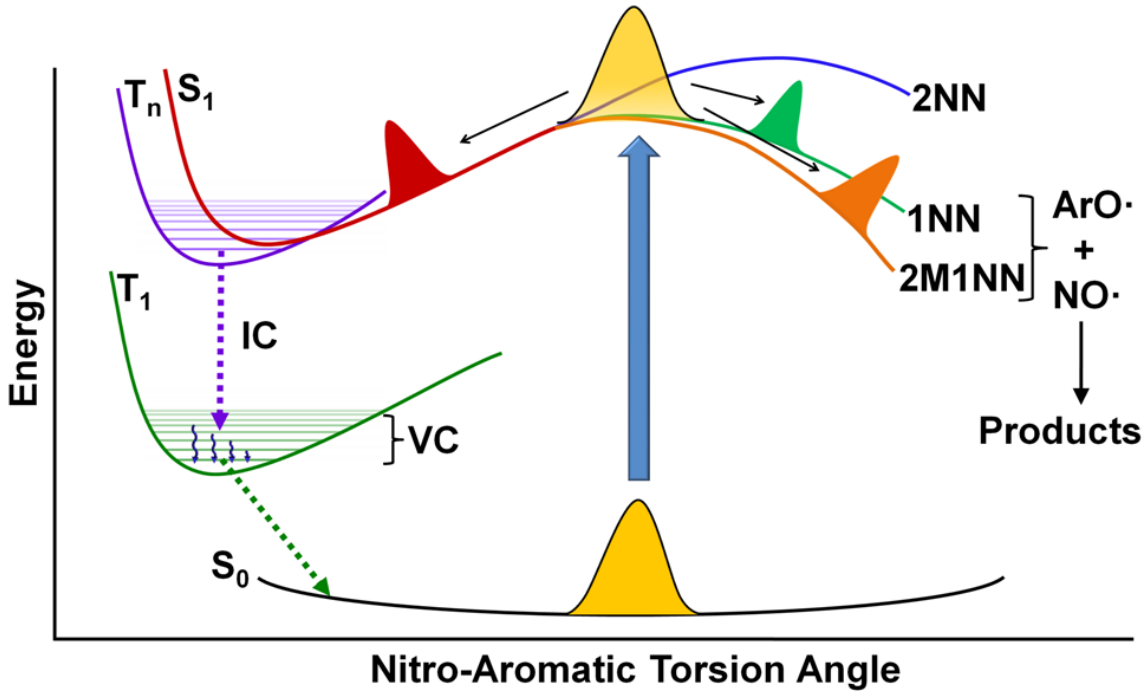

Scheme 3.1. Pictorial illustration of a kinetic mechanism that can explain the photochemistry of the nitronaphthalene derivatives investigated in this work. Excitation of the distribution of conformations available in the ground state in each molecule to the S_1 state results in different extent of ultrafast bifurcation to two primary relaxation pathways: (1) intersystem crossing to the triplet manifold (left) and dissociation directly from the S_1 state (right) to form the aryloxy and NO radicals. The latter channel is not observed in 2NN due to a sizable energy barrier. The generic yellow Gaussian-shape symbol represents different distributions of torsion angles available for each molecule in the ground-state, the location of which is not the same in each molecule (see Figures 3.3 and 3.5). The red, green, and orange Gaussian-shape symbols represent the fraction of population that bifurcates to each of the main relaxation channels (not shown at scale).

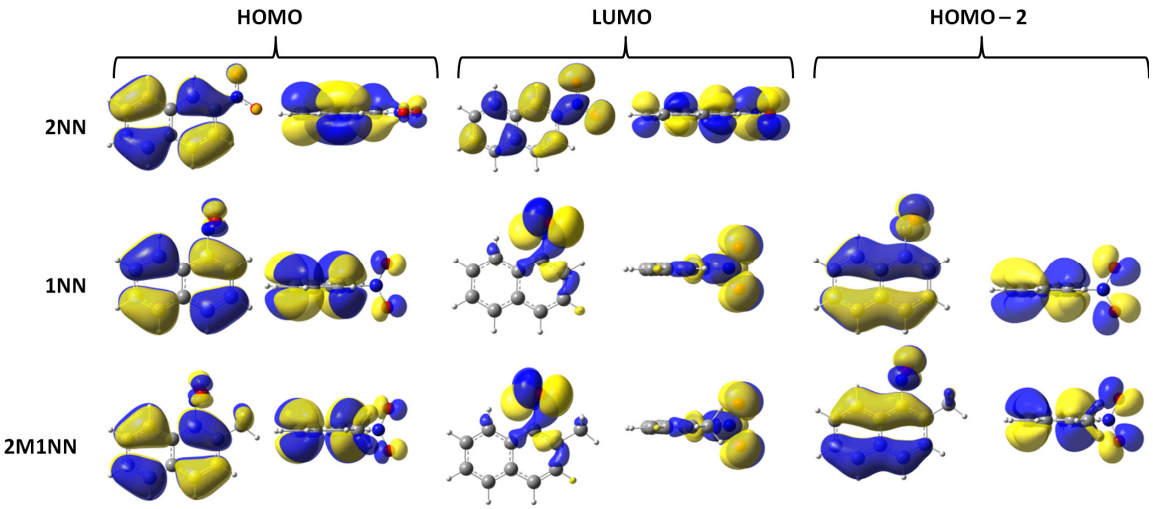

Figure 3.12. Molecular orbitals participating in the configuration-interaction transitions of the optimized S_1 state in 1NN (top), 2M1NN (middle), and 2NN (bottom) in acetonitrile at the PBE0/IEFPCM/6-311++G(d,p) level of theory. Similar configuration-interaction transitions were obtained in cyclohexane (not shown).

The time-resolved results in cyclohexane and acetonitrile lend additional insights about the excited-state relaxation pathway leading to photochemical reaction (Figure 3.9). Similar to 1NN,[91] the transient absorption data for 2M1NN suggests that excitation results in ultrafast branching of the initial (S_1, $\pi\pi^*$) state population toward the triplet manifold or toward a dissociative decay channel. In the case of 2NN, intersystem crossing to the triplet manifold is mostly observed. The relaxed T_1 state in 1NN, and presumably in 2M1NN and 2NN, undergoes intersystem crossing back to the ground state within a few microseconds in N_2-saturated solutions.[91]

The second decay channel in 2M1NN is proposed to evolve along a dissociative decay pathway in the S_1 state potential energy surface. The calculations support that the S_1 state potential energy surfaces of 1NN[7] and of

2M1NN are repulsive in nature along the nitro-aromatic torsion angle reaction coordinate (Figure 3.3Figure 3.5). This decay pathway is populated in ultrafast time scale,[91] reaching a region in the potential energy surface that has significant charge-transfer character and negligible oscillator strength. This is not the case for 2NN. While the S_1 state energy minimum for 2NN has planar geometry with a nitro-aromatic torsion angle of 0° in both solvents, the calculations predict that the S_1 state of 1NN and 2M1NN has the nitro-group close to perpendicular to the aromatic moiety (torsion angle of 106° in 1NN and 104° in 2M1NN), with the nitro-group acquiring a pyramidal conformation (Figure 3.6). The S_1 state optimizations show that the nitro-aromatic torsion angle is the reaction coordinate that plays the key role in the excited-state dynamics in nitro-PAHs, as previously suggested.[38-40,91]

The fully-optimized S_1 state in 2NN is has a 100% LUMO ← HOMO transition with electron density distribution mostly localized in the π-molecular orbitals of the aromatic moiety (Figure 3.12). A small but noticeable fraction of the electron density in 2NN accumulates in the π^* orbitals of the oxygen atoms. In contrast, the fully-optimized S_1 state in 1NN and 2M1NN is composed of 16-17% LUMO ← HOMO and 84-83% LUMO ← HOMO – 2 molecular orbital transitions (Figure 3.12). In both transitions, a major fraction of the electron density is transferred from the π-molecular orbitals of the naphthalene moiety to the anti-bonding orbitals of the nitro group. This transfer of electron density is expected to increase the probability of dissociation and can also explain the pyramidal conformation of the nitro-group in the S_1 state minimum. We note that

nitro-aromatic radical anions with and without ortho substituents have been shown to prefer geometrical structures where the nitro is perpendicular to the aromatic moiety and has a pyramidal conformation in solution.[110-112]

It should be noted that even though the S_1 state minimum of 2NN has some degree of charge transfer character, the charge transfer character of the S_1 state minimum in 1NN and 2M1NN seems to be significantly higher (Figure 3.12). This explains the smaller oscillator strength of the adiabatic S_1 state in 1NN and in 2M1NN relative to that in 2NN. As noted above, the sizable accumulation of electron density in the anti-bonding orbitals resulting in the pyramidalization of the nitro-group, together with the strong charge transfer character of the LUMO $\leftarrow$ HOMO and LUMO $\leftarrow$ HOMO – 2 transitions, are expected to increase the probability of breaking the C-N bond. This supports our[40,91] and others88,[92] hypothesis that dissociation of the nitro-group can occurs directly from the S_1 state.

Figure 3.3 and Figure 3.5 show marked differences in the slope of the two relaxation pathways for the distribution of torsion angles available at room temperature in each molecule. The calculations suggest that upon excitation, the ground-state distributions are promoted to different regions of configuration space in the S_1 potential energy surface, resulting in a different extent of population of the two major relaxation channels. A steeper gradient toward the dissociation channel is predicted for 2M1NN than for 1NN (Figure 3.5). The ultrafast branching in the S_1 state can occur on the same time scale as conformational relaxation,[40,91] making it a competitive relaxation pathway. Thus,

the magnitude of the photodegradation yield in 2M1NN and 1NN is proposed to result primarily from the fraction of the initial population that evolves along the dissociation channel (Scheme 3.1).[91] In 2NN, the distribution of torsion angles available at room temperature has to surmount a 4.6 kcal/mol energy barrier in the S_1 potential energy surface and thus cannot access the sloped region toward the dissociation channel (Figure 3.5, Scheme 3.1).

Evidence that the triplet state of the nitronaphthalene derivatives is not the primary photochemical channel is the observation that even though triplet state yield of 2NN (0.83)[44] is greater than that of 1NN (0.63),[43] the photodegradation yield is much higher in 1NN than 2NN. Hence, excitation of 2NN results in ultrafast population transfer from the Franck-Condon region toward the T_3 state (Scheme 3.1).[91] The T_3 state internally converts to the T_1 state, which can presumably decay back to the ground state in cyclohexane and acetonitrile solutions.

CONCLUSIONS

We provide evidence that the ultrafast branching dynamics in the S_1 state is primarily controlled by different distribution of nitro-aromatic torsion angles that are available in the ground state in each molecule and by the topology of the S_1 state in the Franck-Condon region of configuration space sampled at the time of excitation. This model is more evident when comparing the experimental and computational results obtained for 1NN and 2M1NN. Substitution of the hydrogen atom in the ortho position of 1NN by a methyl group does not significantly perturb the electronic structure of these two molecules, while it increases the

photodegradation yield of 2M1NN by ~46% relative to that of 1NN. The key changes are the shift of the ground-state distribution of torsion angles to closer to 90° and the steeper energy gradient in the S_1 state toward the dissociation pathway that methylation of the ortho position in 1NN has on 2M1NN. Our results provide evidence of an important relationship between conformational distribution of the nitro-aromatic torsion angles before light absorption and the photochemistry of these nitronaphthalene derivatives.

Interestingly, a correlation seems to exist between the mutagenic and carcinogenic structure-activity relationships of nitro-PAHs[97] and the structure-reactivity relationship observed in this work. If these results can be generalize to other nitro-PAHs, photochemical experiments could in principle be used as an affordable and convenient method to screen and prioritize compounds before more costly and involved experimental analysis using laboratory animals are performed to test for the biological activity of nitro-PAHs.

UV resonance Raman and / or femtosecond time-resolved vibrational techniques should be able to provide further insights about the excited-state structural dynamics in nitro-aromatic compounds and its relationship with the ground-state conformational sampling. From a computational side, high-level *ab initio* and molecular dynamics simulations are needed to fully map the minimum energy paths, energy barriers, and the potential participation of conical intersections in the nonradiative dynamics of these nitronaphthalene derivatives. It would be also interesting to evaluate the applicability of the proposed kinetic

mechanism to other small nitro-PAHs (i.e., nitro-PAHs with three and four aromatic rings).

Chapter 4. Excited-State Dynamics of (Organophosphine)Gold(I) Pyrenyl Isomers*

ABSTRACT

Ultrafast dynamics of isomeric (tricyclohexylphosphine)gold(I) pyrenyl complexes have been measured in chloroform and cyclohexane at room temperature. Internal conversion from an upper excited singlet (S_n) to the S_1 state occurs in less than 200 fs after 340 nm excitation. Internal conversion in the singlet manifold is followed by 11 to 100 ps intersystem crossing to a receiver triplet state depending on the site of pyrene metalation. The receiver triplet state (T_n) then decays to the T_1 state in an ultrafast time scale, which decays back to the S_0 state in microseconds time scale in N_2-saturated conditions. The singlet and triplet transient absorption spectra of the 2-metalated isomer show pronounced vibrational structure at room temperature, which is absent in the 1-metalated isomer. The vibrational progressions in the singlet and triplet absorption bands of the 2-metalated isomer are assigned to C=C stretching modes. An increase in intensity and red shift of 250 cm^{-1} of the vibrational bands in going from chloroform to cyclohexane is observed, which is proposed to be a manifestation of the Ham effect. Time-dependent density-functional theory calculations on model complexes predict an accidental degeneracy of the S_1 and T_2 states of the 1-pyrenyl. No such degeneracy occurs for the 2-pyrenyl isomer. A small S_1–T_2 energy gap promotes the tenfold increase in the intersystem crossing rate in the 1-pyrenyl complex. The calculations indicate that the frontier orbitals of both gold complexes are pyrenyl-centered. Altogether, the combined experimental and computational results reveal that the site at which pyrene is metalated significantly modulates its excited-state dynamics.

* This text has been modified from Vogt, R. A.; Peay, M. A.; Gray, T. G.; Crespo-Hernández, C. E.; "Excited-State Dynamics of (Organophosphine)Gold(I) Pyrenyl Isomers", *J. Phys. Chem. Lett.* **2010**, *1*, 1205.

INTRODUCTION

Triplet excited states outlast singlets, and the long lifetimes invite a number of applications. Among these are sensing,[113-115] singlet oxygen sensitization,[116] protein imaging,[117] organic light-emitting diode (OLED) construction,[118-120] and others.[121-124] Research interest in phosphorescent metal complexes is growing. The heavy-atom effect of the metal center relaxes spin selection rules, and intersystem crossing to triplet states becomes more efficient.[125]

Gold(I) is possibly an ideal heavy-atom effecter.[126,127] The (phosphine)- and (*N*-heterocyclic carbene)gold(I) fragments are isolobal with the hydrogen atom; they bind terminally to sp^2-hybridized carbon.[29,128,130,131-133] Gold(I) being d^{10}, ligand-field states do not induce nonradiative decay. Finally, gold(I) often adopts linear two-coordination.[134,141] The low coordination number militates against steric strain in gold(I) organometallics.

We recently disclosed the synthesis of aurated pyrenes **1** and **2**.[136,137] These isomers show structured emission from 600-900 nm with millisecond-scale lifetimes at 77 K. A later report by Yip and co-workers[138] provides absorption and emission spectra of four (triphenylphosphine)gold(I) pyrene derivatives, but time-resolved data are not discussed. Here we present quantitative studies of the excited-state dynamics of both complexes. Included are measurements of the time constant for intersystem crossing to the emitting triplet state. Ultrafast measurements are rationalized with time-dependent density-functional theory calculations.

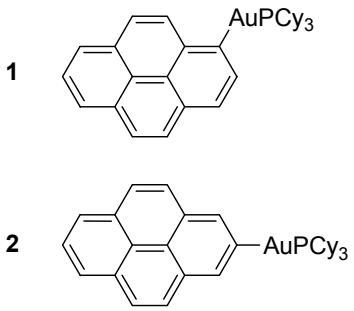

Cy = cyclohexyl

RESULTS AND DISCUSSION

Figure 4.1 collects broadband transient absorption spectra of the (phosphine)gold(I) pyrene derivatives 1 and 2 in cyclohexane and chloroform solutions; Figure 4.2 depicts corresponding contour plots. Absorption decay traces and global fits to the experimental data appear in Figure 4.3. Two exponentials and a time-independent offset are needed to adequately fit the transient absorption signals in the temporal window from femtoseconds to three nanoseconds. Table 4.1 assembles the lifetimes obtained from global fit analyses. The initial growth in the transient absorption spectra observed during the first ~500 fs is assigned to internal conversion among singlet excited states (top panel in Figure 4.1a, b, and c). Two transient absorption bands with maxima at ~380 and 580 nm are observed for the S_n state ($S_m \leftarrow S_n$ transitions, where m > n). Foggi and co-workers have observed similar transient absorption spectra and ultrafast internal conversion in the singlet manifold in pyrene after 340 nm excitation in ethylene glycol at room temperature.[139] Their results further support our assignment of the sub-200 fs relaxation pathway to internal conversion from an S_n state to the S_1 state in both 1 and 2 isomers. Importantly, the S_n state decays to populate the S_1 state with a sub-200 fs lifetime independent of the

isomer or solvent used. The near-identical lifetimes of 2 in chloroform and cyclohexane (Table 4.1), rule out intermolecular vibrational cooling dynamics as responsible for the observed sub-200 fs spectral evolution. The reason is that intermolecular vibrational cooling dynamics often slow down in chloroform.[65,69,70] The spectral bands of the S_1 state for both isomers in chloroform strikingly resemble those of the pyrene molecule[139], strongly suggesting that absorption of light at 340 nm excite mainly the pyrene chromophore in isomers 1 and 2. Excited-state calculations reported below corroborate this hypothesis.

Table 4.1. Lifetimes obtained from global fits analyses of the transient absorption spectra

Compound	Solvent	τ_1 (ps)	τ_2 (ps)
1	Chloroform	0.19 ± 0.02[a]	11.3 ± 0.2
2	Chloroform	0.13 ± 0.02	108 ± 1
2	Cyclohexane	0.15 ± 0.02	106 ± 1

[a] errors are reported as two times the standard deviation from global fit analyses of the transient data of at least two individual measurements.

The second lifetime is assigned to intersystem crossing (ISC) from the S_1 state to a receiving triplet state in both **1** and **2**, which internally converts to the T_1 state in an ultrafast time scale. Evidence for this assignment comes from the observation of well-defined isosbestic points (bottom panels in Figure 4.1a, b, and c) and also from the fact that molecular oxygen quenches the corresponding long-lived transient species (see Table 4.2). In addition, both isomers show steady-state phosphorescence in chloroform in the spectral region from 600 to 900 nm at 77 K.[137] The insensitivity of this lifetime to the use of cyclohexane versus chloroform (a heavy-atom solvent) is understood in terms of the

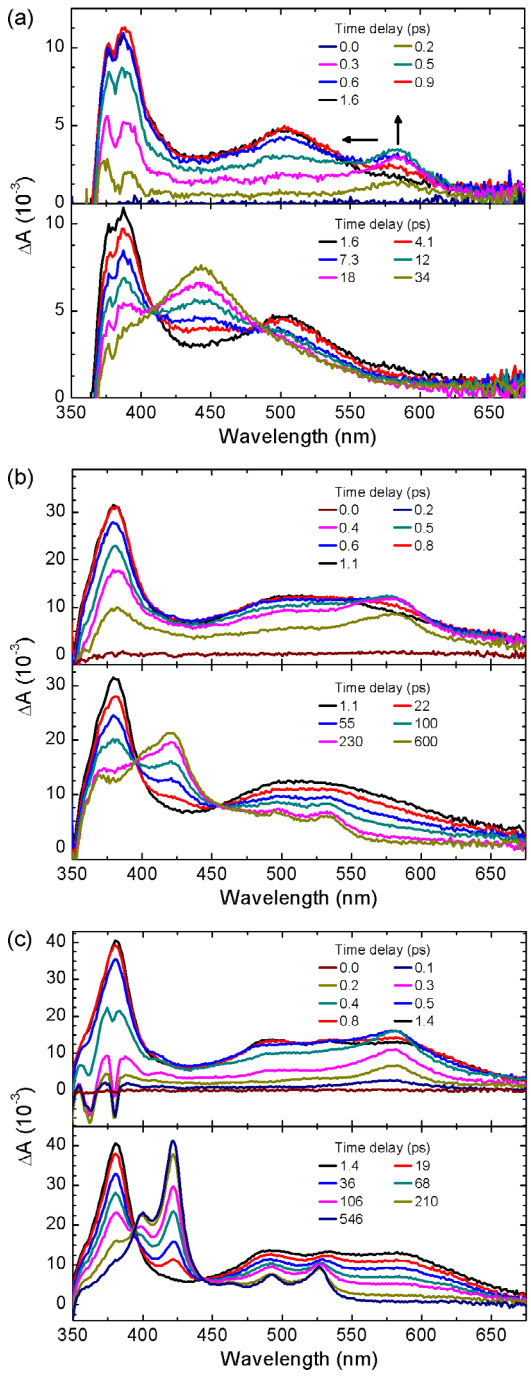

Figure 4.1. Transient absorption spectra for (a) for 1 in chloroform, and (b) and (c) for 2 in chloroform and cyclohexane, respectively. The stimulated Raman signals of the cyclohexane solvent are observable at early time delays. The arrows shown in top panel of (a) highlight the transition from the S_n to the S_1 states.

intramolecular heavy-atom effect already imposed by the gold atom. The spin-orbit coupling of a 5d-electron in gold (5100 cm^{-1})[140] is comparable to that of a 5p-electron in iodine (5700 cm^{-1}),[141] a classical heavy atom. The lack of solvent effect for the second lifetime also seems to rule out vibrational cooling in the triplet manifold. Here again, the spectral features of long-life transient absorption spectrum for both isomers (i.e., strong absorption maximum around 425 and moderate absorption bands above 450 nm) resemble those of the T_1 state of pyrene.[142-144] This observation further supports the assignment of the long-lived species to the T_1 state. The T_1 state decays back to the S_0 state in hundreds of nanoseconds in air-saturated versus tens of microseconds in N_2-saturated solvents (Table 2). The decay signal is bi-exponential for **2** in N_2-saturated cyclohexane, but not in chloroform. No attempts are made to characterize the origin of the second lifetime in the present work. However, it is likely to be related to a formation of a photoproduct, as a precipitate deposited in the cell over time.

Table 4.2. Decay lifetimes of the phosphorescent state of 1 and 2 in air-saturated and N_2-saturated conditions

Sample	Solvent	τ_{air} (ns)	τ_{N2} (μs)
1	Chloroform	295 ± 10[a]	9 ± 3
2	Chloroform	320 ± 30	16.1 ± 0.7
2	Cyclohexane	210 ± 20	17 ± 5; 66 ± 9[b]

[a] errors are reported as two times the standard deviation from global fit analyses of the transient data of two individual measurements; [b] a bi-exponential decay was observed; see the text for details.

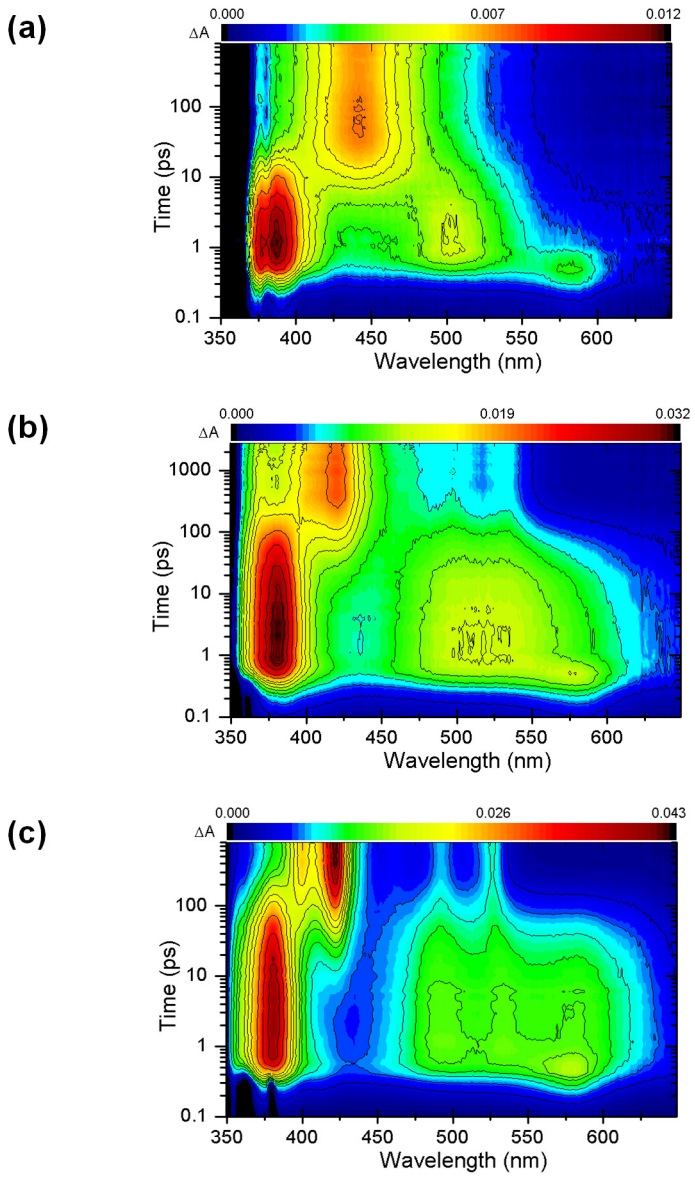

Figure 4.2. Contour plots (a) for 1 in chloroform, and (b) and (c) for 2 in chloroform and cyclohexane, respectively.

Strikingly, Table 4.1 shows that the ISC lifetime in **1** decays tenfold faster than in **2**. The increased rate of ISC in **1** compared to **2** is explained by an increase in spin-orbit coupling between the singlet and triplet manifolds in **1** due to a decrease in the singlet-triplet energy gap, which strengthens vibronic

coupling between the S_1 state and the receiver triplet state. Excited-state calculations performed using the time-dependent implementation of density functional theory support this proposal (see below).

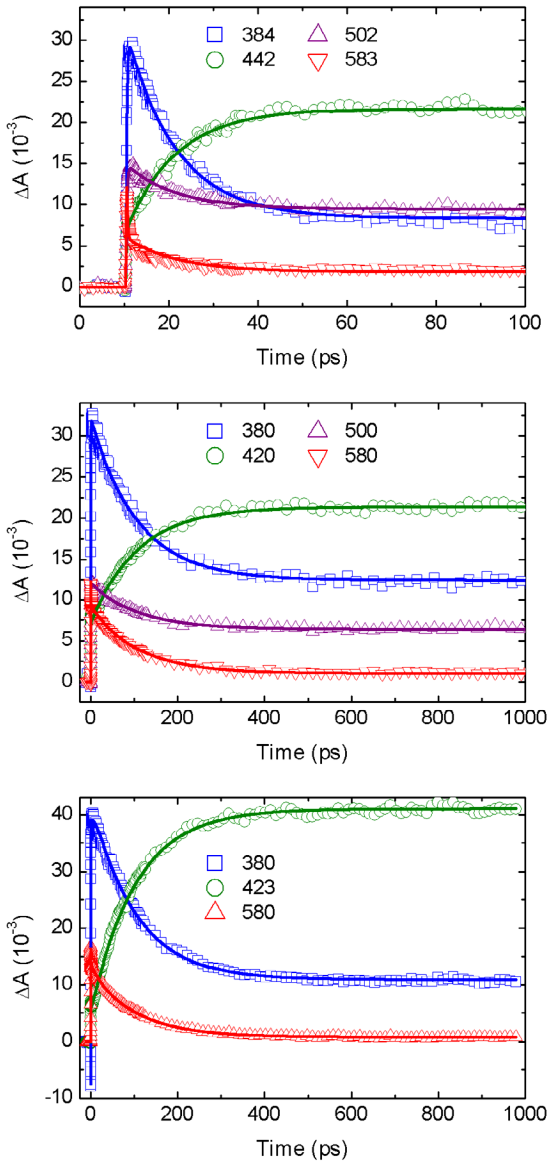

Figure 4.3. Representative transient absorption signals for (a) 1 in chloroform, (b) 2 in chloroform and (c) 2 in cyclohexane at the specified probe wavelengths (nm). Best global-fit curves are shown by solid lines.

The time-resolved results suggest that internal conversion from the receiver triplet state to the T_1 state is ultrafast in both isomers. Crespo-Hernández and co-workers have recently shown that ISC to a receiver triplet state in 1-nitropyrene is also followed by ultrafast internal conversion to the T_1 state in nonpolar solvents.[40] The ISC lifetime of **1** is only 1.5-fold larger than that of 1-nitropyrene. It is tempting to suggest that the excited-state dynamics of the pyrene chromophore, in particular the ISC rate, is modulated by the position at which the pyrene molecule is substituted. Work is underway to corroborate this hypothesis using other substituted polycyclic aromatic compounds.

Attention now shifts to the vibronic structure observed in the transient absorption spectra and its solvent dependence. While the transient absorption bands of **1** does not show vibrational structure, **2** shows significant vibronic structure from ~400 to 650 nm, more so in cyclohexane solution than in chloroform (Figure 4.1). Prominent vibrational progressions in electronic absorption bands often reveal the most important nuclear distortions that occur during the electronic transition.[35] The triplet absorption band of **2** shows a vibrational separation of 1290 $\pm$ 40 cm^{-1} in cyclohexane and in chloroform solutions (Figure 4.4). Frequency calculations of the optimized T_1 state of **2′**, suggest that this vibrational separation can be assigned to C=C stretching vibrational modes in the pyrene moiety. Similarly, the S_1 state shows weak vibronic structure in cyclohexane but not in chloroform solutions (see top panel in Figure 4.4). A vibrational spacing of 1570 $\pm$ 20 cm^{-1} is estimated for this weak vibrational series. Optimization of the S_1 state of model compound **2′** at the CIS

level of theory in cyclohexane (CIS/IEFPCM/LANL2DZ, see methods section) suggest that C=C stretching modes are also the major nuclear distortions that occur during this transition.

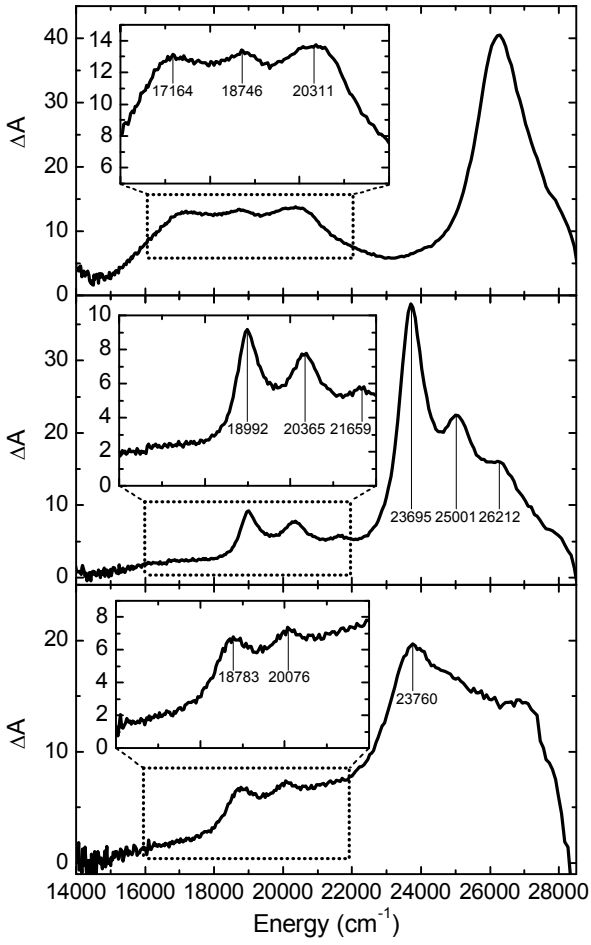

Figure 4.4. Transient absorption spectrum for isomer 2 showing vibrational progressions in the excited singlet state at a delay time of 1.4 ps (upper panel) and for the lowest-energy triplet state in cyclohexane (middle panel) and chloroform (bottom panel).

Surprisingly, an increase in the intensity of the vibrational progressions, and a red shift of 250 $\pm$ 40 cm^{-1} in the case of the triplet absorption bands, is observed in going from chloroform to cyclohexane solutions for isomer **2** (Figure

4.4). Similar solvent effects have been observed in the fluorescence and phosphorescence vibronic structure of other pyrene derivatives at 77 K,[145] which has been suggested to be a manifestation of the Ham effect.[146,147] In simple terms, the Ham effect is thought to result from nonspecific interactions of the solute molecule with the neighboring solvent molecules, which distort the symmetry of the solute molecular framework affecting its electronic structure through dispersion (London) forces. Furthermore, it has been suggested that the pyrene chromophore is an ideal molecule for detecting this solvent effect.[145] In general, symmetry-forbidden vibrational components appear with increasing intensity as the polarizability and polarity of the solvent increase. In the present case, the higher polarizability of cyclohexane (11.04 $Å^3$) versus chloroform (8.53 $Å^3$) is proposed to play the major role in increasing the intensity of the vibrational progressions observed for isomer **2** in the singlet and triplet manifolds.[148] The calculated large dipole moments of isomer **2′** in the S_1 (9.58 D) and T_1 (9.01 D) states at the DFT/IEFPCM/LANL2DZ level of theory suggest that **2** is highly polarized in the singlet and triplet manifolds. Thus, a relatively large change in solute-solvent interaction may be required after excitation. It seems reasonable that as the polarizability of the solvent increases, the larger the perturbation to the electronic structure of the highly polarized solute in the excited states would be. Certainly, more experimental and computational work is needed to corroborate this proposal.

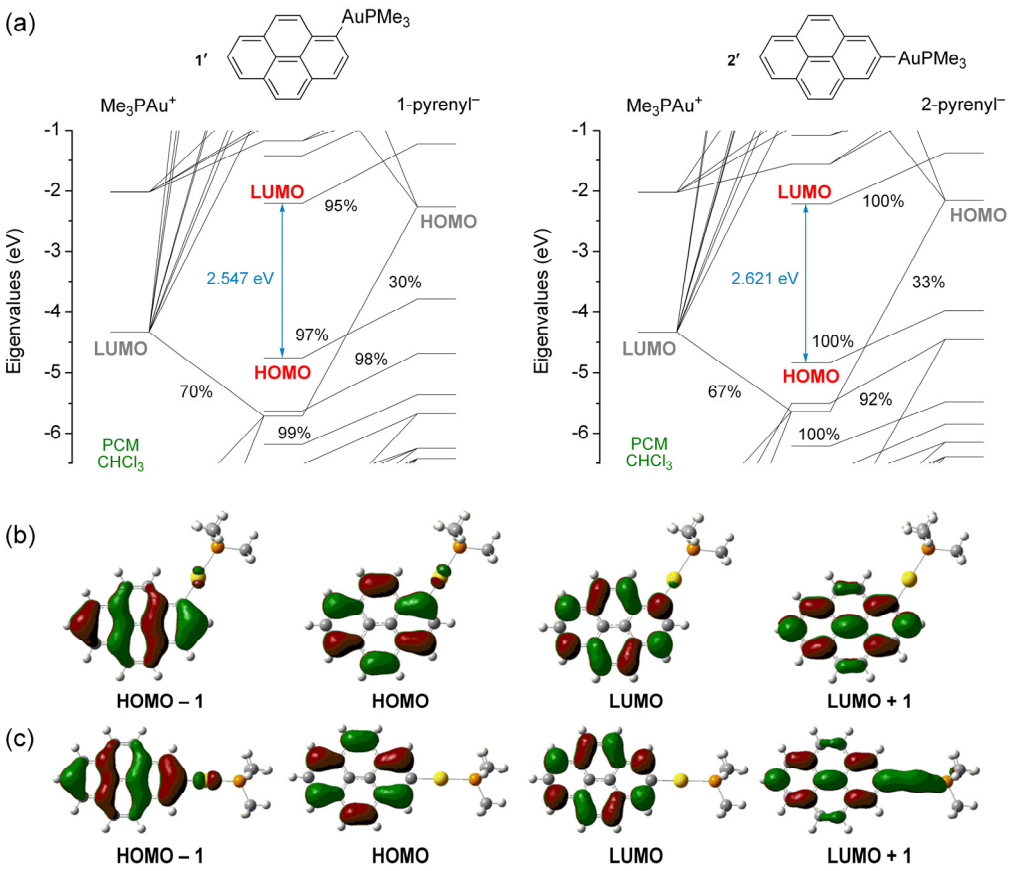

Figure 4.5. (a) Partial Kohn-Sham orbital energy level diagrams of model complexes 1′ and 2′. (PBE/Stuttgart ECP and basis on Au; TZVP on C, H, and P). Implicit $CHCl_3$ solvation is included through a polarizable continuum model. Percentage contributions of (phosphine)gold(I) cation and pyrenyl anion fragments are indicated. (b) and (c) Plots of selected orbitals of 1′ and 2′ respectively (contour level 0.03 a.u.).

Density-functional theory (DFT) calculations were applied to model complexes **1′** and **2′**, where trimethylphosphine replaces tricyclohexylphosphine. Figure 4.5 (a) depicts partial Kohn-Sham orbital energy level diagrams of **1′** and **2′**; plots of frontier orbitals appear in Figure 4.5 (b) and (c). The two highest occupied and lowest unoccupied orbitals are primarily pyrenyl π^* functions. The LUMO + 1 of **2′** has a 14% contribution from gold (in terms of electron density)

that is lacking in **1′**. Transitions from the HOMO – 1 or HOMO of **2′** to its LUMO + 1 will bear pyrenyl ligand-to-metal charge-transfer (LMCT) character. For both compounds, the HOMO – 2 accounts for the C–Au σ-bond. Plots of these orbitals appear in Figure 4.4. HOMO–LUMO energy gaps are similar and both concur with an absorption onset in the ultraviolet. To the eye, both organogold complexes are colorless.

Time-dependent DFT calculations find that the first several excited states of **1′** and **2′** are mainly pyrenyl ππ* transitions. Figure 4.7 plots the vertical excitation energies computed for these states. In **1′**, a near-degeneracy occurs between the first excited singlet and the second triplet state. The calculated energies of S_1 and T_2 for **1′** are 3.147 eV (394.0 nm) and 3.149 eV (393.7 nm). No such coincidence occurs for **2′**. In additon, the S_1 and T_1 states of **2′** were

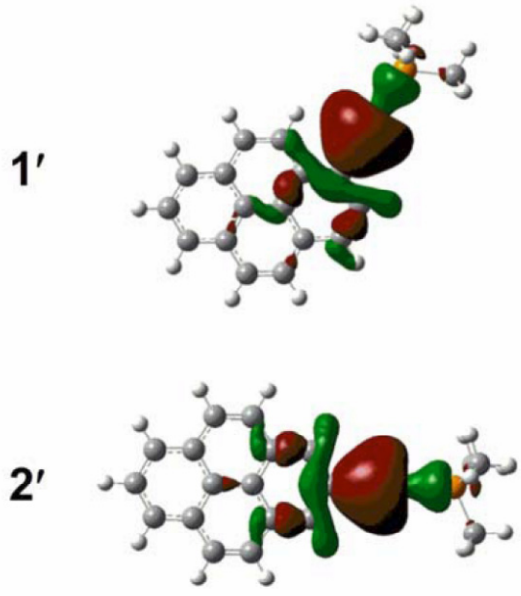

Figure 4.6. Orbital plots of the HOMO – 2 of 1′ and 2′. The contour level is 0.03 a.u.

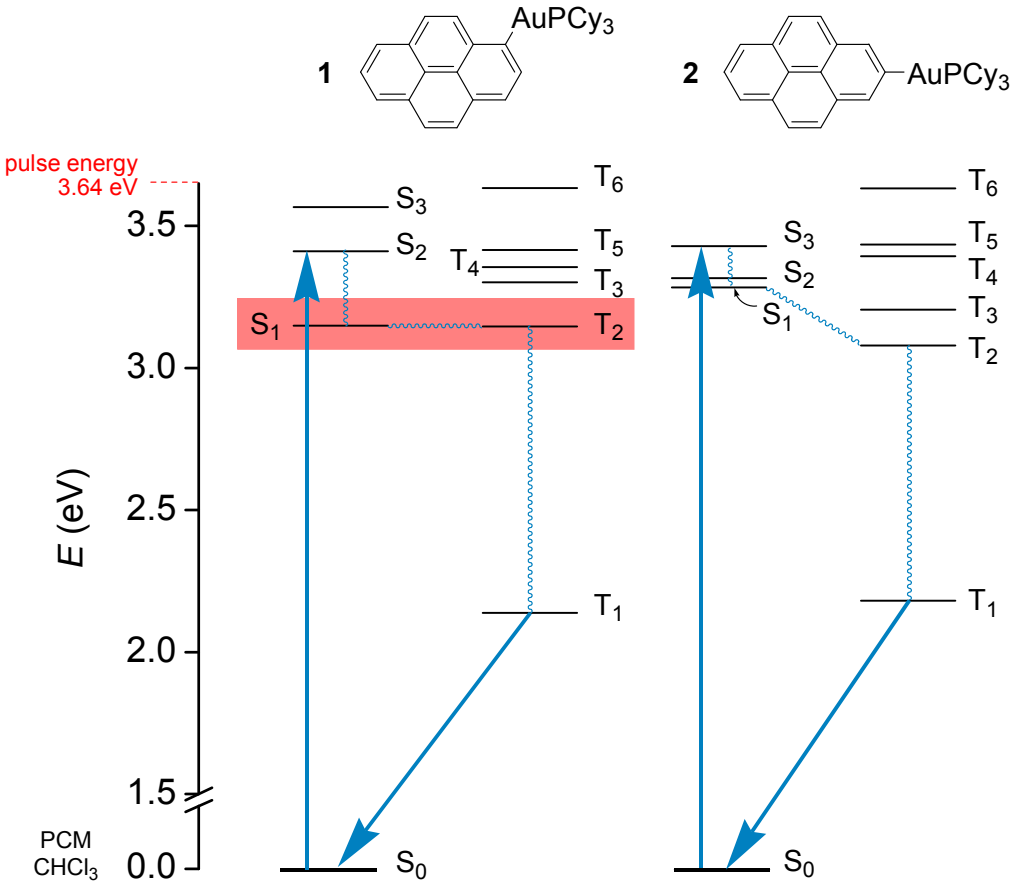

Figure 4.7. TDDFT-calculated singlet and triplet states of model complexes **1′** (left) and **2′** (right). Calculations include implicit chloroform solvation. Superimposed is a Jablonski diagram depicting the photophysics of the genuine compounds **1** and **2**.

optimized at the CIS/IEFPCM/LANL2DZ and PBE1PBE/IEFPCM/LANL2DZ levels of theory, respectively, in cyclohexane. The S_1 state is composed of 78% LUMO ← HOMO and 22% (LUMO + 4) ← (HOMO – 1) single particle transitions. These molecular orbitals are reported in Figure 4.8 and are almost exclusively pyrenyl $\pi\pi^*$ transitions. Frequency calculations were performed at the same

levels of theory and no imaginary frequencies were observed. The calculated S_1 state vibrational frequencies were scaled using a scaling factor of 0.9335 before comparison with experiments.

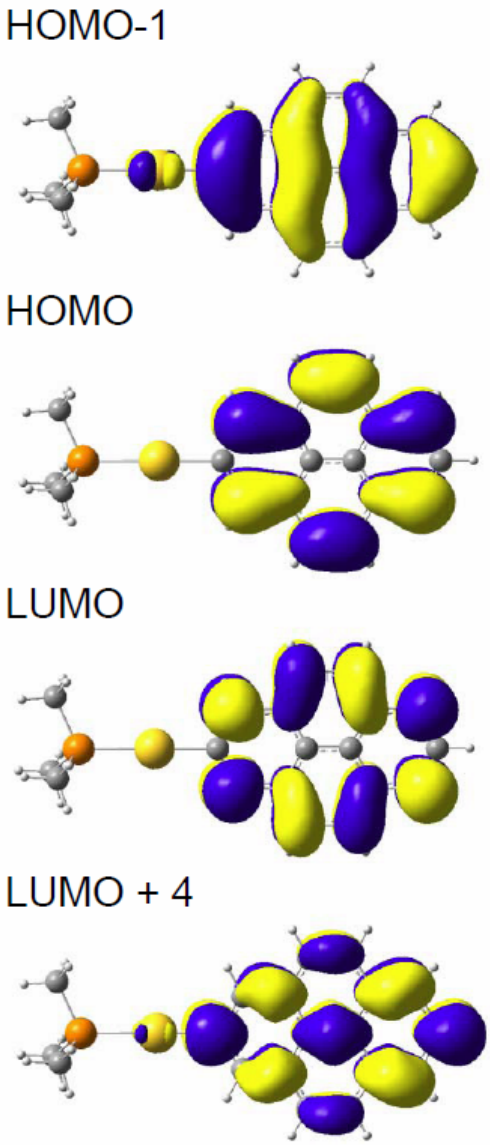

Figure 4.8. Optimized S_1 state of model complex **2′** at the CIS/IEFPCM/LANL2DZ level of theory in cyclohexane: 78% LUMO ←HOMO and 22% (LUMO + 4) ← (HOMO – 1).

CONCLUSIONS

In summary, (trialkylphosphine)gold(I) groups are relativistic spectators. The kinetic model presented in Figure 4.5 accounts for experimental and computational results. Excitation at 340 nm populates an S_n state in both metalated pyrenes. Ultrafast internal conversion (> 200 fs) in the singlet manifold ensues, which is followed by ISC. Intersystem crossing is an order of magnitude faster in **1** than in **2** because of a fortuitous degeneracy of the S_1 state and a receiver triplet state in **1**, which calculations assign as T_2. Time-dependent DFT calculations capture this excited-state oddity. The spin-orbit coupling of gold relaxes the spin prohibition of intersystem crossing in both isomers. Ultrafast internal conversion in the triplet manifold leads to the emitting triplet T_1, which decays nonradiatively or by phosphorescence. The position of metalation at pyrene dominates the excited-state dynamics. Substitution of pyrene at the 1-position with either a nitro or (trialkylphosphine)gold(I) group leads to remarkably similar ISC rates. Studies of related organometallics and of di-gold pyrenes are underway.

Experimental and Computational Methods

The femtosecond broadband transient absorption spectrometer and data analysis procedure have been described in detail elsewhere.[91] Briefly, a Quantronix *Integra-i/e 3.5* Laser generating 100 fs pulses at 800 nm with a repetition rate of 1 kHz is used to pump an optical parametric amplifier (OPA, TOPAS, Quantronix / Light Conversion). The OPA output is tuned to 340 nm, which is used as the excitation wavelength. Contributions to the excitation pulse

from other wavelengths or polarizations are removed by a reflective wavelength filter (λ-filter) and a Glan-Taylor prism. The excitation pulses are attenuated to the desired intensity using a neutral density optical filter in order to minimize cross phase modulation effects.[149,150] The polarization of the excitation pulses is randomized by passing the beam through a depolarizing plate in the spectrometer to prevent rotational relaxation effects from contributing to the kinetics.

A broadband transient absorption spectrometer (Helios, Ultrafast Systems, LLC) is used for data acquisition. A continuously moving 2-mm CaF_2 crystal is used for white light continuum generation (WLC) giving access to the spectral range from 350 to 675 nm. The probe pulses are corrected for group velocity dispersion (GVD)[51] using a home-made LabView (National Instruments, Inc.) program, as described previously.[91] Details of the spectrometer can be found elsewhere.[91] A pump/probe beam diameter ratio of three was used in this work. An averaging time of 0.4 s is used for a single spectrum, equaling 200 single laser shots. A complementary WLC generation source is used to follow the time evolution of the transient absorption signals from hundreds of picoseconds to microseconds in the spectral range from 360 to 675 nm (Eos, Ultrafast Systems, LLC), as described elsewhere.[91]

Data analysis is performed using the Igor Pro 6.04 software (Wavemetrics, Inc.). The kinetic traces are globally fitted using a sum of exponential terms, convoluted with a Gaussian response function of 160 fs.[91] An instrument response function of 400 ps is used when analyzing the transient signals

obtained with the Eos module. A delta function is included in the fitting subroutine to account for any coherent response signals when needed. Representative kinetic traces in the spectral range between 350 nm and 675 nm are selected for each dataset in the global fitting analysis. The time constants are linked for all the traces while the amplitudes are left wavelength-dependent. The reported uncertainties for the kinetic analysis are twice the standard deviation (2σ) of at least two independent transient absorption measurements.

The absorbance of **1** and **2** were adjusted to 1.0 ± 0.2 at the excitation wavelength of 340 nm using a 2-mm optical path length cell. The samples were continuously stirred with a Teflon-coated stir bar and a magnetic stirrer to avoid re-excitation of the excited volume by successive laser pulses. Solutions were carefully monitored for photodegradation using a spectrophotometer (Cary 100, Varian, Inc.) throughout the experiments. The samples were replaced with fresh solutions before a 5% decrease in steady-state absorbance at the excitation wavelength was observed. Ground- and excited state calculations were performed using Gaussian03.[52] Gas-phase geometries were optimized in C_s symmetry using the TZVP basis set of Godbelt, Andzelm, and co-workers for non-metal atoms,[151] and the Stuttgart 97 effective core potential and basis on gold;[152] scalar relativistic effects are treated implicitly.[153] Harmonic frequency calculations show the converged structures to be potential energy minima in the ground state. Chloroform solvation was included through the polarizable continuum model of Tomasi and co-workers. [63,154] Computed densities for both

isomers passed stability tests. Population analyses were performed with the AOMIX-CDA software of Gorelsky.[155,156]

Chapter 5. Sub-Picosecond Intersystem Crossing in Mono- and Di-(Organophosphine)gold(I) Naphthalene Derivatives in Solution*

ABSTRACT

Femtosecond to microsecond broadband transient absorption experiments are reported for Cy3PAu(2-naphthyl) (**1**), (Cy3PAu)2(2,6-naphthalenediyl) (**2**), and (Cy3PAu)2(2,7-naphthalenediyl) (**3**). Global and target analysis of the data based on a sequential kinetic model reveal four spectral components. These components are assigned to (**1**) excited state absorption (ESA) of the ligand-centered S_1 state; (**2**) ESA of a receiver ligand-to-metal or metal-to-ligand charge transfer triplet state ($\tau_1 \leq 300$ fs); (**3**) ESA of the vibrationally-excited, ligand-centered T_1 state (τ_3 = 7 to 10 ps); and (4) ESA of the relaxed T_1 state. Intersystem crossing (ISC) occurs in hundreds of femtoseconds, while internal conversion (IC) in the triplet manifold is slow ($\tau 2 \sim 2$ ps). The relaxed T_1 state shows biphasic decay kinetics in **2** and **3** with lifetimes of hundreds of picoseconds and hundreds of nanoseconds in air-saturated conditions, while only monophasic decay is observed in **1** under identical conditions. The main decay pathway of the T_1 state is assigned to quenching by O_2, while the minor channel is tentatively assigned to self-quenching or triplet-triplet annihilation. The ISC rate in **1** is not modulated significantly by the incorporation of a second heavy-atom group effecter. Instead, the position at which the second Au(I)-phosphine group is attached plays a noticeable role in the ISC rate, showing a threefold decrease in **2** than in **3**. The results challenge the conventional view that the rate of IC is larger than that of ISC, lending further support to the emerging kinetic model proposed for other transition-metal complexes. Gold(I) now joins the exclusive group of transition metals known to form organometallic complexes exhibiting excited-state non-equilibrium dynamics.

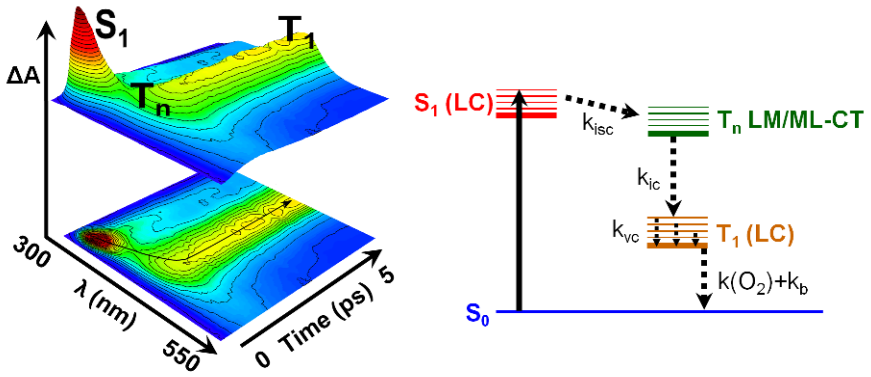

* This text has been modified from Vogt, R. A.; Gray, T. G.; Crespo-Hernández, C. E.; "Subpicosecond Intersystem Crossing in Mono- and Di-(Organophosphine)gold(I) Naphthalene Derivatives in Solution", *J. Am. Chem. Soc.* **2012**, *134*, 14808.

INTRODUCTION

The design of heteroatomic organic compounds exhibiting high triplet yields continues to attract interest because of their potential technological and life sciences applications.[27,157-161,162-164] In particular, the chemistry of organogold(I) compounds is receiving much attention for potential use in advanced materials in metallotherapeutic drugs, photodynamic therapy, organic near-infrared emitters, and sensing applications.[28-34] The formation of a gold(I)-carbon σ bond can significantly modify the electronic states of an organic aromatic compound[136-137,165] by enhancing spin-orbit interactions, thus increasing the rate of radiationless transition between singlet and triplet states relative to the gold(I)-free hydrocarbon counterpart.[165,166] For instance, organogold(I) compounds can exhibit dual luminescence at room temperature with emission yields that depend sensitively on the position of auration.[129,136,138,166-168] Most photophysical investigations performed thus far have focused on describing the absorption and emission properties of the newly-synthesized gold(I) organometallics.[129,136-138,167] Much less is known, however, regarding the excited-state dynamics and relaxation mechanisms that are at play in this family of compounds.[165,166] This fundamental information is essential to current efforts aimed at tuning the photophysical properties of these novel systems and for the rational design of advanced luminescent materials based on gold(I)-functionalization.[30,31,166]

In this contribution, we unravel the electronic structure and excited-state dynamics of Cy_3PAu(2-naphthyl) (**1**), $(Cy_3PAu)_2$(2,6-naphthalenediyl) (**2**), and $(Cy_3PAu)_2$(2,7-naphthalenediyl) (**3**) in dichloromethane. Contrary to the

(organophosphine)gold(I) pyrene and the oligo(o-/m-/p-PE) gold(I) complexes investigated recently,[129,165,166] these gold(I)-substituted naphthalenes show remarkably large intersystem rate constants (ca. 10^{12} to 10^{13} s^{-1}) and unusually slow rates of internal conversion in the triplet manifold (ca. 10^{11} s^{-1}). The sub-picosecond intersystem crossing lifetimes measured for the gold(I) compounds in this work are among the fastest observed in transition metal complexes,[169-178] showing that auration can tune the excited-state dynamics of organic compounds to the strongly non-adiabatic regime. Importantly, we have resolved in time and in frequency the upper electronic state that acts as doorway state in the ultrafast population of the phosphorescent state in these gold(I) organometallic compounds. This was achieved by using global and target analysis[179,180] based on a sequential kinetic model. To the best of our knowledge, these aurated naphthalenes represent the first examples of organogold(I) compounds exhibiting sub-picosecond intersystem crossing dynamics.

RESULTS

Quantum Chemical Calculations. All quantum-chemical calculations for Cy_3PAu(2-naphthyl) (**1**), $(Cy_3PAu)_2$(2,6-naphthalenediyl) (**2**), and $(Cy_3PAu)_2$(2,7-naphthalenediyl) (**3**) were performed with methyl groups in place of the cyclohexyl groups on phosphorus. Hereafter, they are identified as **1'**, **2'**, and **3'**, respectively. The S_0- and S_1-optimized structures for **1'**, **2'**, and **3'** in dichloromethane are shown in Figure 5.1. The naphthalene moiety is planar in the S_0 state, while phosphorus has a tetrahedral geometry and a P-Au-C_2 bond angle of ~180° in all three compounds. The S_0 geometries are in good agreement

with those reported in the gas phase previously.[137] The S_1 state geometry of **1'** shows noticeable changes relative to the geometry in the S_0 state. In particular, the naphthalene moiety losses planarity, with the carbon atom in the position 3 going out of the plane in a semiboat-like conformation. The C_2-C_3-C_4-C_9 and C_1-C_{10}-C_9-C_4 torsion angles twist to 16.7° and -4.3°, respectively, while the P-Au-C_2 bond angle contracts by 5° relative to the bond angle of 179.9° in the S_0 geometry. In addition, the C_1-C_{10}, C_2-C_4, C_5-C_6, and C_7-C_8 bonds enlarge by 0.03 Å, while the C_1-C_2 bond contracts by the same amount relative to the corresponding S_0 bond lengths. The naphthalene moiety remains planar in the S_1-optimized structures of **2'** and **3'** (changes in torsion angles are less than 0.1°), while the C-C bonds lengths enlarge or contract by as much as 0.06 Å relative to the S_0 bond distances. All other geometrical parameters in the S_1-optimized structures of **2'** and **3'** suffer minor changes relative to the corresponding S_0-optimized structures.

The energies and oscillator strengths of the optimized S_1 states for **1'**, **2'**, and **3'** are 3.42 eV (0.0756), 3.73 eV (0.0848), and 3.66 eV (0.5018), respectively. These values were determined by using the IEFPCM equilibrium solvation model in dichloromethane. The S_1 energies are off by 0.4 eV relative to the experimental zero-zero energy of **1'** ($E_{0,0}$ = 3.88 eV) but in excellent agreement to that of **3'** ($E_{0,0}$ = 3.66 eV) in dichloromethane. For **2'**, it is not possible to estimate the zero-zero energy reliably from the absorption and fluorescence spectra (Figure 5.2), but the calculated S_1 energy is in excellent agreement with the lowest-energy fluorescence maximum in dichloromethane.

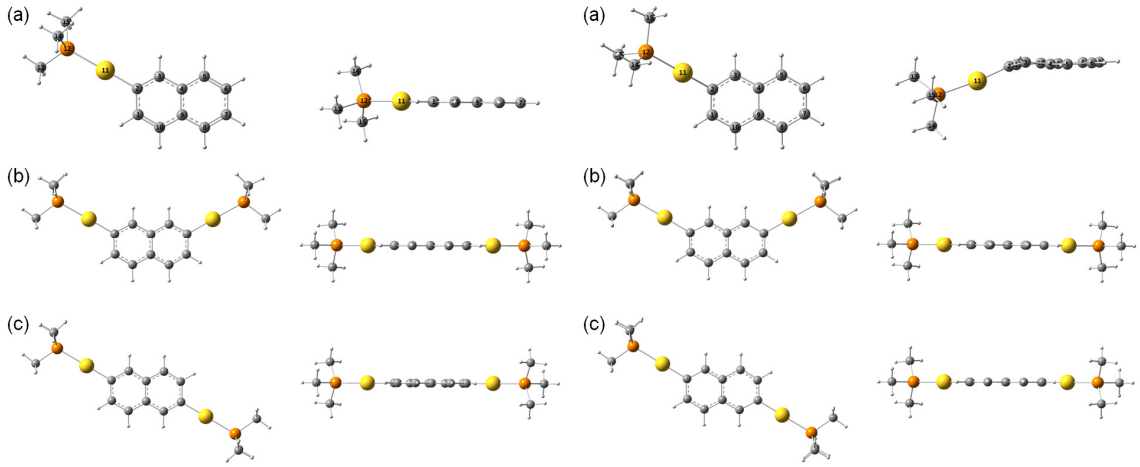

Figure 5.1. Optimized structures of the ground state of the model mono- and di-gold(I) naphthalene compounds; (a) **1'**, (b) **2'**, and (c) **3'**, respectively, at the PBE0/(E)-IEFPCM/LANL2DZ level of theory in dichloromethane (left panel). Optimized structures of the first excited singlet state of the model mono- and di-gold(I) naphthalene compounds at the TD-PBE0/(E)-IEFPCM/LANL2DZ level of theory in dichloromethane (right panel). The number assignment of atoms is shown in (a). Carbon atoms are shown in grey, gold atoms in yellow, phosphorus atoms in orange, and hydrogen atoms in white.

Table 5.1 presents the calculated vertical excitation energies and oscillator strengths of the five and six lowest-energy singlet and triplet states, respectively, for **1'**, **2'**, and **3'** in dichloromethane relative to the optimized S_0 geometry. These vertical excitation energies and oscillator strengths were obtained by using the non-equilibrium IEFPCM solvation model, as explained in the Methods Section. The S_1 vertical excitation energies are in reasonable agreement (within 0.2 to 0.3 eV) with the onset of the absorption spectra of each compound in the same solvent (Figure 5.2). The estimated accuracy of the vertical excitation energies herein is in very good agreement with that recently reported by Jacquemin et al.[181] for the same level of theory from a benchmark work that includes the experimental absorption and emission data of forty compounds. In addition, there

are five triplet states lower in energy than the S_1 state of **1'** and **2'**, while there are four triplet states bellow the S_1 state of **3'** when the S_0-optimized structures are used to calculate the vertical excitation energies. The energy gap between the S_1 state and the nearest lowest-energy triplet state in **1'**, **2'**, and **3'** is 0.01 eV, 0.06 eV, and 0.10 eV, respectively, when using the S_0-optimized geometry as reference. The negligibly small S_1-T_n energy gaps and the high phosphorescence yields[137] suggest the presence of strong spin-orbit coupling interactions between the singlet and the triplet manifolds in **1'**, **2'**, and **3'** in dichloromethane. Finally, and for completeness, Table 5.1 also includes the dipole moments of **1'**, **2'**, and **3'** in the S_0 and S_1 states in dichloromethane.

Table 5.2 reports the estimated character of the vertical singlet and triplet excited states as percentage relative to the S_0-optimized geometry. We remark that a quantitative assignment of the various transitions that leads to a particular character of the excited states is difficult. To make the discussion of the excited state more straightforward, we describe each state by using the Kohn-Sham orbital configurations that play the most preponderant role in the single-particle electronic transitions describing each excited state. In particular, we distinguish three types of transitions:[182,183] (1) transitions between Kohn-Sham orbitals primarily localized on the metal or metal-centered (MC) transitions; (2) transitions between Kohn-Sham orbitals primarily localized on the ligand; known as ligand-centered (LC) transitions; and (3) transitions between a Kohn-Sham orbital primarily localized on the ligand and a Kohn-Sham orbital primarily localized on the metal. The latter transitions can originate from single-particle ligand to metal

or metal to ligand transitions. Therefore, they are labeled as ligand-to-metal (LM) or metal-to-ligand (ML) charge transfer transitions, LMCT or MLCT, respectively.[182,183]

Table 5.1. Vertical excitation energies calculated using TD-PBE0 functional, the LANL2DZ basis set, and the NE-IEFPCM solvation model. These energies were obtained relative to the S_0-optimized geometry, which was optimized using the E-IEFPCM solvation model at the same level of theory. The estimated accuracy in energy from a comparison with the experimental data in Figure 5.2 is $\pm$ 0.3 eV.

Model System	**1'**	**2'**	**3'**
S_1	4.37 (0.086)	4.28 (0.025)	4.20 (0.301)
S_2	4.45 (0.012)	4.28 (0.004)	4.30 (0.014)
S_3	4.63 (0.008)	4.58 (0.013)	4.59 (0.000)
S_4	5.17 (0.001)	4.82 (1.533)	4.88 (0.028)
S_5	5.19 (1.098)	4.87 (0.000)	4.90 (0.000)
T_1	2.59	2.56	2.55
T_2	3.92	3.80	3.83
T_3	4.15	4.12	4.09
T_4	4.23	4.15	4.10
T_5	4.36	4.22	4.32
T_6	4.41	4.33	4.32
$\Delta(S_1 - T_n)^a$	0.01	0.06	0.10
$\Delta(T_n - T_1)^a$	1.77	1.66	1.55
Dipole Moment, S_0 (D)	9.399	8.422	0.010
Dipole Moment, S_1 (D)	9.372	8.532	0.075

[a] T_n is the triplet state that is closest to but lower in energy than the S_1 state.

Table 5.2. Estimated character of the excited states, in percentage, obtained from a time-dependent density-functional analysis of the single particle transitions constituting each state, relative to the S_0-optimized structures.

Model System	S_1	T_1	T_2	T_3	T_4	T_5	T_6
1'-S_0	90% LC 10% LMCT	85% LC 15% LMCT	86% LC 14% LMCT	44% LC 56% LMCT	5% LC 95% LMCT	87% MLCT 13% LMCT	4% LC 96% LMCT
2'-S_0	90% LC 10% LMCT	90% LC 10% LMCT	10% LC 90% LMCT	80% LC 20% LMCT	50% LC 50% LMCT	30% LC 70% LMCT	22% LC 88% MLCT
3'-S_0	80% LC 20% LMCT	90% LC 10% LMCT	90% LC 10% LMCT	70% LC 30% LMCT	30% LC 70% LMCT	20% LC 80% LMCT	90% MLCT 10% MC

Since the experimental and theoretical evidence accumulated in this and in a previous work[137] suggests that strong spin-orbit coupling between the excited electronic states is at play, it may be inappropriate to distinguish between singlet and triplet excited states in these compounds. For convenience, and as it is customary in the literature,[182] we use the spin state to label the excited states even when its denotation is not strict. In support of this choice, we note that the absorption and emission spectra of **1**, **2**, and **3** strongly resemble those of naphthalene in the same solvent (Figure 5.2), indicating a large LC character of the electronic transitions in these compounds and, in particular, of the S_1 states. This choice is also supported by the analysis of the character of the excited states reported in Table 5.2. In addition, we note that the calculations suggest that the T_1 state has mostly LC character, which is in line with the high

phosphorescence yield measured for these metallated naphthalenes in solution.[137] The primary LC nature of the electronic transitions in **1'**, **2'**, and **3'** is in agreement with the LC character reported for the electronic transitions of (organophosphine)gold(I) pyrene and oligo(o-/m-/p-PE) gold(I) complexes recently.[129,165,166]

Broadband Transient Absorption Experiments. Time-resolved absorption spectra were recorded to probe the excited-state dynamics of the gold(I)-naphthalene derivatives and to reveal the decay pathways leading to the population of the phosphorescent state. Transient absorption spectra at selected time delays are given in Figure 5.3 for compounds **1**, **2**, and **3**, respectively. Contour plots showing the multidimensional transient absorption data are shown in Figure 5.4. Following excitation, a broad absorption band grows within the cross-correlation of the pump and probe pulses, with absorption maximum at ~335 nm for compounds **1** and **2** and below 330 nm for **3**. We denote this absorption band as band **A** hereafter. As band **A** grows, another absorption band (band **B**, hereafter) begins to grow with maximum at 430 nm in **1**, ~440 nm in **2**, and 470 nm in **3** (Figure 5.3, panel (a)). Band **B** continues to grow as band **A** decays (Figure 5.3, panel (b)). Figure 5.3 also show that band **B** evolves within the first two picoseconds to populate an absorption band in the same spectral region (band **C***, hereafter). Band **C*** blue shifts, narrows, and becomes more structured as time progresses developing into band **C** after few tens of picoseconds. Band **C** partially decays within a time delay of three nanoseconds in **2** and **3** (but not in **1**), as shown in panel (c) in Figure 5.3.

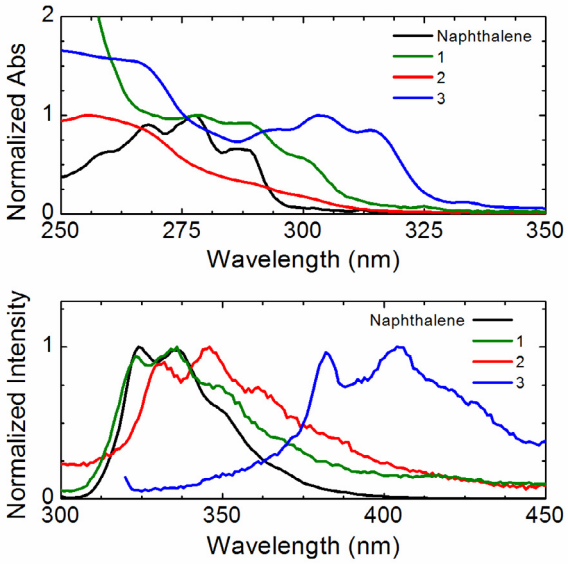

Figure 5.2. Comparison of the absorption (top panel) and fluorescence (bottom panel) spectra of naphthalene with those for Cy_3PAu(2-naphthyl) (**1**), $(Cy_3PAu)_2$(2,6-naphthalenediyl) (**2**), and $(Cy_3PAu)_2$(2,7-naphthalenediyl) (**3**) in dichloromethane.

Transient absorption experiments were also performed in the nanosecond-to-microsecond time scale for compounds **1** and **3** to quantify the rate of decay of the absorption band **C** in air-saturated conditions (panel (d) in Figure 5.3). Analogous experiments for **2** were unsuccessful because of the significant degradation of this compound during the time required to collect the time-resolved data from the nanosecond to microsecond time window. The absorption band **C** in **1** and **3** decays mono-exponentially in the nanosecond to microsecond time scale and, within the sensitivity of our spectrometer, no other absorption bands are observed after ~1μs. Transient absorption experiments performed for **1** and **3** under N_2-saturated conditions display a significant slowdown in the decay of this absorption band (data not shown), showing that this long-lived species is quenched by molecular oxygen.

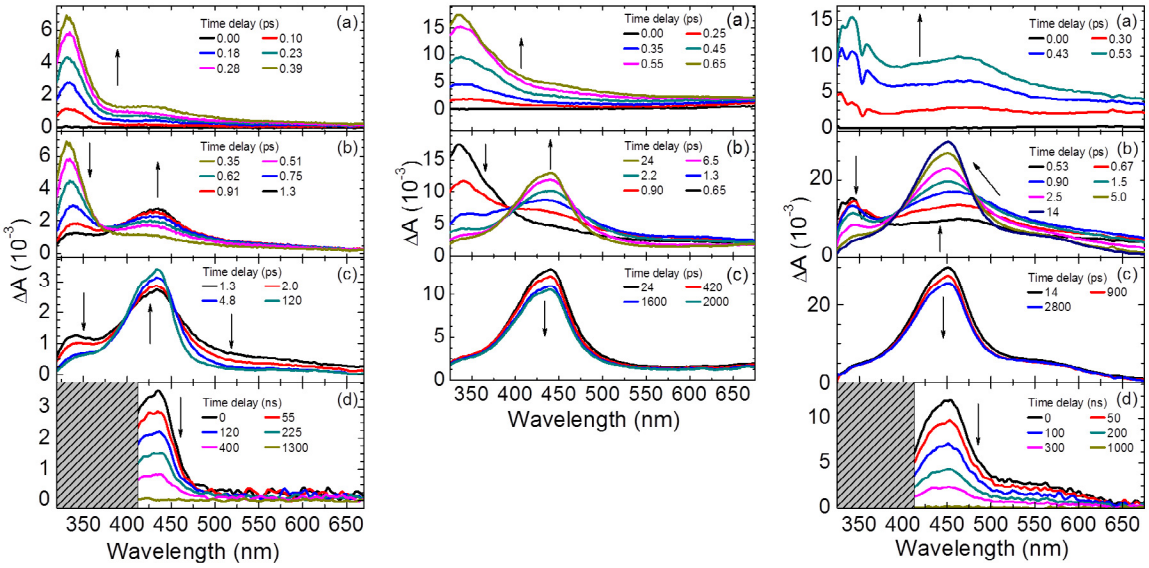

Figure 5.3. Two-dimensional transient absorption spectra at selected time delays for Cy_3PAu(2-naphthyl) (**1**) in dichloromethane excited at 285 nm (left panel); for $(Cy_3PAu)_2$(2,6-naphthalenediyl) (**2**) in dichloromethane excited at 266 nm (middle panel); and for $(Cy_3PAu)_2$(2,7-naphthalenediyl) (**3**) in dichloromethane excited at 320 nm (right panel). Stimulated Raman emission bands of the solvent are observed around 350 nm within the pulse width of the femtosecond excitation beam in graph (a) of the right panel. The bottom graphs in the left and right panels are blocked with dashed rectangle because the absolute magnitude of the absorption intensities in the spectral region below 420 nm are underestimated by white light generation source used in this work to probe the kinetics from the nanosecond-to-microsecond time scale.

Representative decay traces are shown in Figure 5.5 for **1**, **2**, and **3** at select probe wavelengths together with best-global fit curves. We used a global and target analysis method based on a sequential kinetic model to extract the lifetime and associated decay spectra from the multidimensional time-resolved absorption data. Data analysis shows that four lifetimes are needed to fit adequately the decay traces during the first three nanoseconds. These lifetimes are reported in Table 5.3, while the corresponding decay associated spectra are

shown in Figure 5.6. Representative decay traces for **1** and **3** in the nanosecond to the microsecond time window, together with best-global fit curves, are shown in Figure 5.7. The latter decay traces were fitted independently from the femtosecond to nanosecond transient data by using an exponential decay function convoluted with a Gaussian response function, as described in the Methods Section.

Table 5.3. Lifetimes obtained from a global and target analysis of the transient absorption data based on a sequential kinetic model (τ_1 to τ_4) or from an exponential decaying function (τ_5); both model functions were convoluted with the corresponding instrument response functions

Compound	**1**	**2**	**3**
τ_1 (fs)	~230	~330	~100
τ_2 (ps)	2.0 ± 0.5[a]	2.0 ± 0.5[a]	2.0 ± 0.5
τ_3 (ps)	10 ± 1	7.2 ± 0.8	7.6 ± 0.5
τ_4 (ps)	∞[b]	410 ± 60	310 ± 40
τ_5 (ns)	265 ± 40	--	180 ± 40

[a] fixed to the lifetime value obtained for **3** during the global analysis; [b] this lifetime does not decay within the 3.2 ns time window and should be associated to τ_5.

DISCUSSION

The chief aim of this work is to unravel and to understand the electronic energy relaxation pathways that ultimately lead to phosphorescence emission in high yields in **1**, **2**, and **3** at room temperature.[137] Understanding the relaxation mechanisms that control the efficiency of triplet state population is critical to the goal of rationally synthesizing gold(I) organometallic compounds for their potential use in a wide range of applications. We begin the discussion by assigning the transient species observed in the femtosecond-to-microsecond time scale. We then present a detailed kinetic mechanism that satisfactorily

explains the electronic relaxation pathways in these organometallic compounds, followed by a comparison of their excited-state dynamics with those previously reported for the (pyrenyl)gold(I) and NO_2-naphthalene/pyrene analogues. Finally, the central results are summarized in the conclusion section.

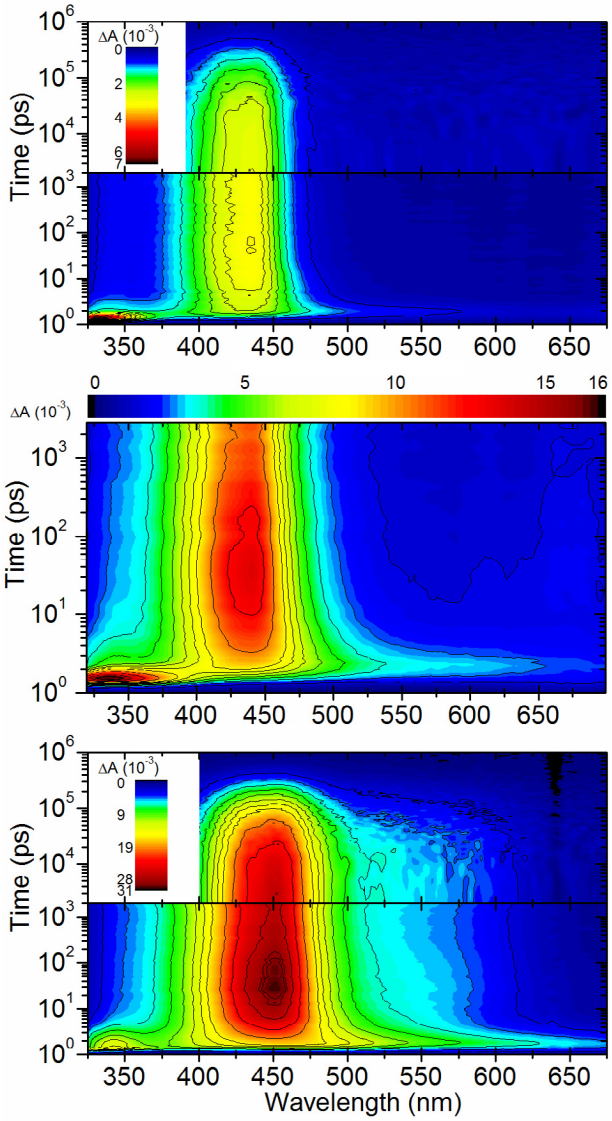

Figure 5.4. Top to bottom: contour representation of the multidimensional time-resolved absorption data for Cy_3PAu(2-naphthyl) (**1**), $(Cy_3PAu)_2$(2,6-naphthalenediyl) (**2**), and $(Cy_3PAu)_2$(2,7-naphthalenediyl) (**3**) in dichloromethane. Note that the time scale expands the femtoseconds to microseconds in **1** and **3**, while only the femtosecond to nanoseconds in **2**.

Assignment of the transient absorption bands. The time-resolved experiments reveal that five relaxation processes take place from the femtosecond-to-microsecond time scale for **2** and **3**, and four relaxation pathways for **1** (Table 5.3). Based on the calculated vertical excitation energies and the corresponding oscillator strengths, the S_1 state in **1'**, **2'**, and **3'** is assigned as the optically populated state with the pump energy used to excite each compound (within the expected accuracy of these calculations $\leq \pm 0.3$ eV). Otherwise stated, the absorption band **A** is assigned to excited state absorption of the optically populated S_1 state. The absence of stimulated emission in the transient absorption spectra of **1**, **2**, and **3** suggests that most of the S_1 state dynamics is occurring on a faster time scale than that accessible using our setup.

Table 5.4. Estimation of fluorescence and phosphorescence quantum yields from the net emission yields for Cy_3PAu(2-naphthyl) (**1**), $(Cy_3PAu)_2$(2,6-naphthalenediyl) (**2**), and $(Cy_3PAu)_2$(2,7-naphthalenediyl) (**3**) at room temperature.

Compound	**1**	**2**	**3**
Net Emission Yield ($\times 10^{-2}$)[a]	0.61	1.4	2.2
Phosphorescence Yield ($\times 10^{-3}$)[b]	5.9	13.1	21.4
Fluorescence Yield ($\times 10^{-4}$)[b]	1.83	9.41	6.1

[a] taken from ref.[137]

[b] calculated by integrating the net emission yield over the fluorescence and phosphorescence bands.

The population in the S_1 state decays in sub-picosecond time scale (τ_1) to populate the transient absorption species **B**. We assign this transient absorption band to a receiver triplet state (T_n) in each compound. This assignment is supported by the following experimental and computational observations. The fluorescence quantum yields of these compounds are negligible (ca. $\leq 10^{-4}$; see Table 5.4), in line with the sub-picosecond lifetime (τ_1), while most of the

emission yields in these compounds at room temperature are due to phosphorescence from the T_1 state.[137] In addition, the population transfer from **A** to **B** shows an isosbestic point in the transient absorption spectra of each compound (Figure 5.3), which suggest state-to-state relaxation dynamics. Furthermore, the calculations predict that several upper triplet (T_n) states lie lower in energy than the S_1 state, one of which is nearly isoenergetic to the S_1 state in each compound. Specifically, the vertical excitation energies shown in Table 5.1 suggest the T_5 state as the receiver state in **1'** and **2'**, while it is the T_4 state in **3'**. The observation that intersystem crossing occurs in hundreds of femtoseconds suggests that singlet to triplet population transfer competes with intramolecular vibrational relaxation in the S_1 state (i.e., intersystem crossing probably occurs in the non-adiabatic regime).[169,172,173,178] The ultrafast nature of the intersystem crossing pathway lend support to the idea that the T_5 state is the receiver state in **1'** and **2'**, while it is T_4 state in **3'**. We remark, however, that high-level *ab initio* calculations that include non-adiabatic molecular dynamics simulations and determination of the spin-orbit overlap integrals for the intersystem crossing pathways are needed to unequivocally assign the receiver triplet state in each compound. Regardless of which upper triplet state actually serves as doorway state, the experimental and computational evidence provides strong support for its involvement in the ultrafast intersystem crossing relaxation pathway in each compound.

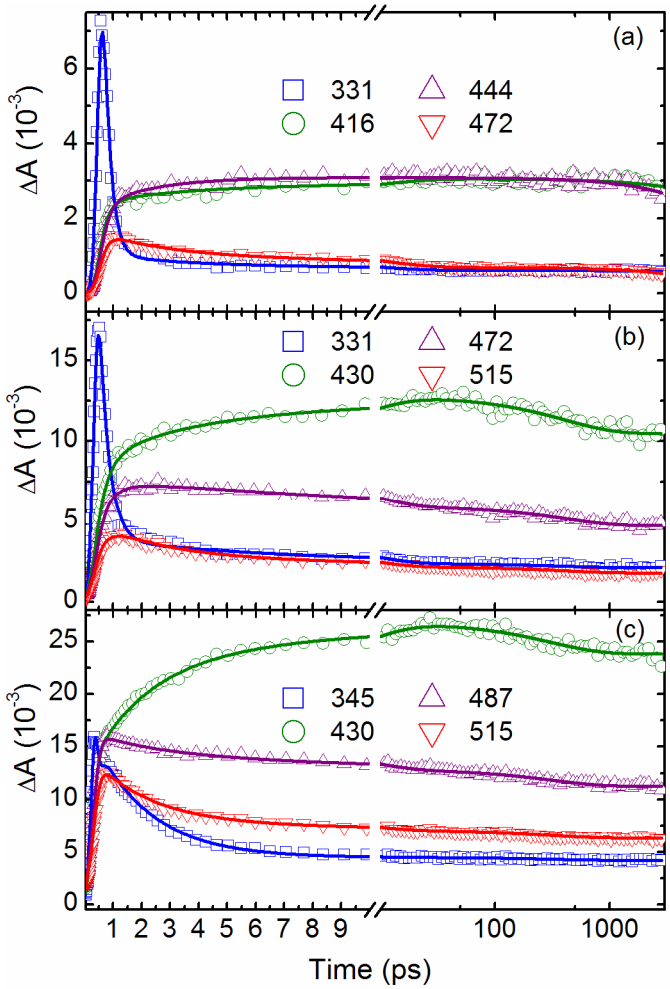

Figure 5.5. Representative decay traces from the femtosecond to nanosecond time scale for (a) Cy_3PAu(2-naphthyl) (**1**), (b) $(Cy_3PAu)_2$(2,6-naphthalenediyl) (**2**), and (c) $(Cy_3PAu)_2$(2,7-naphthalenediyl) (**3**) in dichloromethane. Best global-fit curves obtained by modeling the transient absorption data using target analysis based on a sequential kinetic model are shown by solid lines.

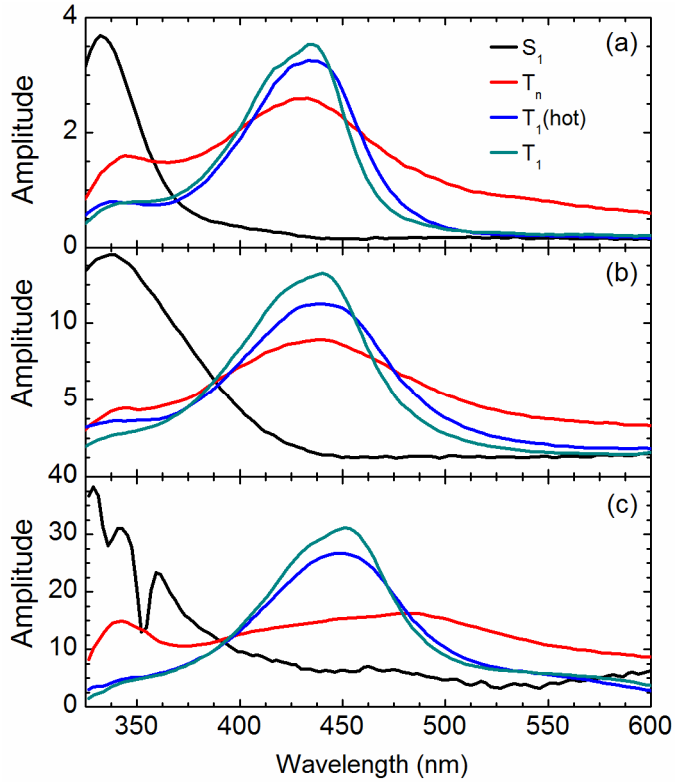

Figure 5.6. Decay associated spectra of the S_1 state, the receiver T_n state, the vibrationally-excited T_1 state, and the vibrationally-relaxed T_1 state in (a) Cy_3PAu(2-naphthyl) (**1**), (b) $(Cy_3PAu)_2$(2,6-naphthalenediyl) (**2**), and (c) $(Cy_3PAu)_2$(2,7-naphthalenediyl) (**3**) in dichloromethane. The decay associated spectra were obtained by modeling the transient absorption data using target analysis based on a sequential kinetic model. Stimulated Raman emission bands of the solvent are captured in the decay associate spectra of the S_1 state in (c) around 350 nm in part because the dynamics of the S_1 state occurs within the pulse width of the femtosecond excitation beam. The decay associated spectra for the S_1 state was scaled by a factor of 0.25, 0.5 and 1 for panels a, b and c, respectively.

The receiver T_n state (band **B**) decays in ~2 ps (τ_2) to populate the transient absorption species labeled as **C***. As shown in Figure 5.9, the absorption band **C*** narrows, blue shifts, and becomes more structured with an increase in time delay (τ_3), resulting in the formation of the long-lived absorption band **C**. Band narrowing, structuring, and blue shifting are often hallmarks of

vibrational cooling dynamics occurring in electronic states.[69-71] Consequently, we assign the decay pathway associated with the conversion of band **B** to **C*** as internal conversion in the triplet manifold (see below), while the transient species **C*** is assigned to the vibrationally excited T_1 state. The vibrationally excited T_1 state decays in 8 to 10 ps to populate the relaxed T_1 state (band **C**). The significantly faster vibrational cooling dynamics in **2** and **3** relative to **1** can be understood in terms of the additional vibrational degrees of freedom imposed by the second (phosphine)gold(I) group in the former compounds. We note that slow internal conversion and vibrational cooling dynamics in the triplet manifold have been reported previously in other naphthalene derivatives.[42,80,81,91] In this respect, the strong ligand-to-metal charge transfer character of the upper excited triplet states reported in Table 5.2 for **1'**, **2'**, and **3'** does not affect significantly the rates of internal conversion and vibrational cooling observed previously in other substituted naphthalene compounds. However, the covalent incorporation of (phosphine)gold(I) groups to the naphthalene framework increases the rate of intersystem crossing from the singlet to the triplet manifold.

Evidence that the band **C** should be assigned to the T_1 state comes from the observation that this transient species is quenched by molecular oxygen in the nanosecond to microsecond time scale. Further support for this assignment comes from the observation of high phosphorescence yield in these aurated naphthalenes at room temperature in solution.[137] Our time-resolved experiments also show that a small fraction of the population in the T_1 state decays with a lifetime of hundreds of picoseconds (τ_4) in **2** and **3** but not in **1**. This decay

pathway is tentatively assigned to triplet-triplet annihilation or self-quenching, but it was not investigated further because its overall contribution to the relaxation mechanism is small. A major fraction of the T_1 state population decays in hundreds of nanoseconds in air-saturated conditions, following a pseudo-first order rate constant characterized by $(\tau_5)^{-1}$.

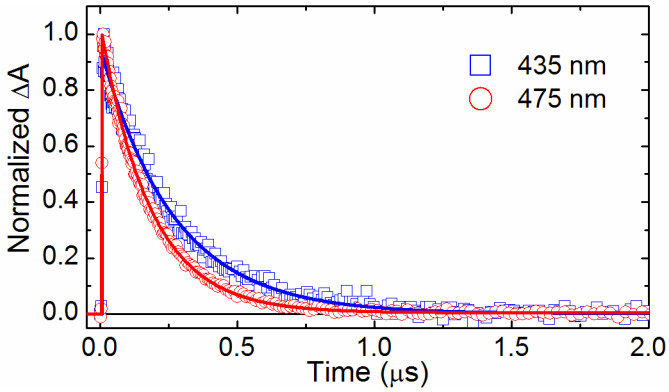

Figure 5.7. Representative decay traces from the nanosecond to microsecond time scale for Cy_3PAu(2-naphthyl) (**1**) (open squares) and $(Cy_3PAu)_2$(2,7-naphthalenediyl) (**3**) (open circles) in dichloromethane. Best global-fit curves obtained by modeling the transient absorption data by using an exponential function convoluted with an instrument response function of 500 ps are shown by solid lines.

The nature of the femtosecond intersystem crossing pathway. In this section we invoke the Fermi's golden rule[187] to rationalized the ultrafast nature of the rate of intersystem crossing in these gold(I)-naphthalene compounds. If we initially assume that any difference between the Franck-Condon overlap factors between the S_1 and T_n states in these compounds can be ignored, the sub-picosecond nature of the intersystem crossing relaxation pathway can be qualitatively explained by the small energy gap between the S_1 and T_n states and by a presumably strong spin-orbit interaction in the region of potential energy surfaces

(PES) where the population transfer occurs. Previous studies have shown that the relative magnitude of the intersystem crossing rate in other transition metal compounds correlates with the square of the spin-orbit integral of the intersystem crossing pathway, but not with the spin-orbit constant of the heavy metal itself.[184,185]

Interestingly, the intersystem crossing pathway in **1** is not modulated significantly by the addition of a second (phosphine)gold(I) functional group (i.e., in **1** versus **2**). This observation suggests that the magnitude of the spin-orbit interaction between the S_1 and T_n PES may be strong enough in **1** that the addition of a secondary heavy-atom group effecter no longer affects the intersystem crossing rate in **2** to a significant extent. This idea is in agreement with the above statement that it is the strength of the square of the spin-orbit integral and not the spin-orbit constant of the metal itself what plays a primary role in the magnitude of the intersystem crossing rate.

On the other hand, the observation that the intersystem crossing lifetime in **2** is approximately threefold slower than in **3** suggests that either the magnitude of the Franck-Condon overlap factors or that of the spin-orbit integral between the S_1 and T_n states (or both) is smaller in **2** than in **3**. Unfortunately, we cannot make any conclusions with the data on hand about which of these two factors play a major role or if, in fact, both are equally important in controlling the intersystem crossing rate. Regardless, the position to which the second (phosphine)gold(I) group is attached, which themselves might reflect a change in the Franck-Condon overlap factors, seems to play a role in modulating the

intersystem crossing rate in these compounds. Thus, we suggest that changes in the topology of PES in the vicinity where the avoided crossing between the S_1 and the T_n adiabatic PES occurs should play a role in modulating the intersystem crossing rate in **2** and **3**. Clearly, information about the topology of the PES involved in the intersystem crossing relaxation pathways as well as the strength of the spin-orbit interaction that promotes them is necessary before a more quantitative discussion is warranted. Taken together, however, the above observations support the idea that intersystem crossing occurs between non-equilibrated excited states,[172,173,175,176,178,186] where the ability of active vibrational modes in the S_1 state to couple and explore the singlet-triplet crossing region might control the intersystem crossing rate.

Evidence supporting the slow rate of internal conversion in the triplet manifold. The suggestion above that internal conversion in the triplet manifold is anomalously slow deserves additional discussion. The calculations presented in Table 5.1 show that there is a large energy difference between the T_n and T_1 states (> 1.5 eV) in these three compounds. We argue that the large energy gap results in poor Franck-Condon overlap factors for internal conversion, which can explain the slow rate of internal conversion in these compounds, as expected from the energy gap law for radiationless transitions.[71,83] Furthermore, the decay associated spectrum of the T_n state in Figure 5.6 is noticeably different from those of the T_1(hot) and T_1 spectra. This provides additional support to the idea that two different excited triplet states are been probed. The slow internal conversion pathway in the triplet manifold is the reason why we are able to

resolve in time and frequency the receiver T_n state from the T_1 state in these gold(I)-naphthalene compounds.

Further evidence for the slow rate of internal conversion is obtained from the data analysis of the transient absorption data. For instance, efforts were made in the case of **1** for using a kinetic model that has two sequential steps instead of the three steps sequential model. However, the two-steps kinetic model did not adequately fit the transient absorption data (Figure 5.8), showing that a three-step sequential model is the simplest model that can be used to satisfactorily model the excited-state dynamics in **1** from the femtosecond to nanosecond time window. Similarly, a four-step sequential model is needed to satisfactorily fit the transient absorption data for **2** and **3** in the same time window. In addition, as noted earlier, slow (ps) internal conversion in the triplet manifold has been reported in other naphthalene derivatives previously,[42,80,81,91] which makes the naphthalene a unique chromophore in this respect. Altogether, the experimental and computational data available provide strong support for the proposed slow internal conversion process in the triplet manifold of these molecules. In the next section, we summarize the overall kinetic model that most adequately explain the transient absorption data from the femtosecond to microsecond time scale in the gold(I)-naphthalene compounds.

Sequential kinetic model. Scheme 5.1 shows a kinetic mechanism that satisfactorily explains the excited-state dynamics observed in these organogold(I) naphthyls. This sequential model is summarized as follows. Excitation of **1**, **2**, and **3** at 285, 320, and 266 nm, respectively, populates primarily the ligand-

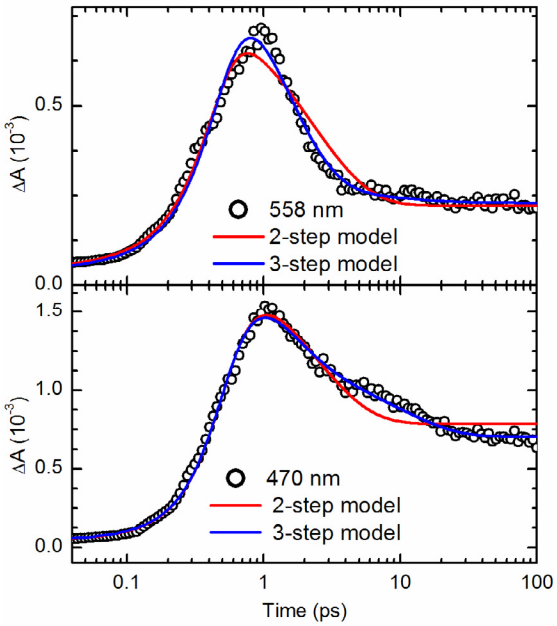

Figure 5.8. Comparison of the goodness of the fit for two representative decay traces at the shown probe wavelengths for compound **1** obtained by using the target analysis method and a two- (red) or three-steps (blue) sequential kinetic model.

centered S_1 state. The S_1 state intersystem crosses to populate a receiver triplet state (T_n) in hundreds of femtoseconds. The T_n state has a strong ligand-to-metal (in **2'** and **3'**) or metal-to-ligand (in **1'**) charge transfer character and internally converts to populate the vibrationally-excited T_1 state in ~2 ps. The hot T_1 state cools down to populate that relaxed T_1 state in 7 to 10 ps. The decay associated spectra of these transient species are reported in Figure 5.6. Finally, the T_1 state decays by two parallel relaxation pathways to populate back the ground state in **2** and **3**, but only one decay pathway is observed in **1** for the triplet state. The main relaxation pathway is assigned to quenching of the T_1 state by molecular oxygen, while the other minor channel, only observed in **2** and **3**, is tentatively assigned to self-quenching or triplet-triplet annihilation. We note that triplet-triplet annihilation

has been shown to play a role in the deactivation mechanism of oligo(PE) gold(I) complexes.[166]

Comparison with (pyrenyl)gold(I) and NO_2-substituted compounds. It is instructive to compare briefly the excited-state dynamics previously reported in aurated pyrenyl derivatives[165] with those in the naphthalene-based systems presented in this work. When the naphthyl in **1** is replaced by pyrenyl moiety, the excited-state dynamics are noticeably affected. The population of the receiver triplet state in **1** is approximately 500-fold faster than in the aurated pyrenyl derivative (pyrenyl compound labeled **2** in ref. [165]). In addition, internal conversion in the triplet manifold of the aurated pyrenyl compound is ultrafast, as expected, while in aurated naphthalenes internal conversion occurs in ~2 ps. Furthermore, while the T_1 state is populated with excess vibrational energy in each of the aurated naphthalene derivatives, vibrational cooling dynamics are not observed in the (pyrenyl)gold(I) derivatives.[165]

Interestingly, the above observations echo those previously reported for 1-nitropyrene (1NP)[40] and 1-nitronaphthalene (1NN)[91] compounds. As in **1**, **2**, and **3**, 1NN shows sub-picosecond population of the triplet manifold and vibrational cooling lifetime of ~10 ps,[91] whereas 1NP shows a slower intersystem crossing to the triplet manifold and no evidence of vibrational cooling dynamics in the T_1 state,[40] as in the (pyrenyl)gold(I) compounds.[165] Taken together, the

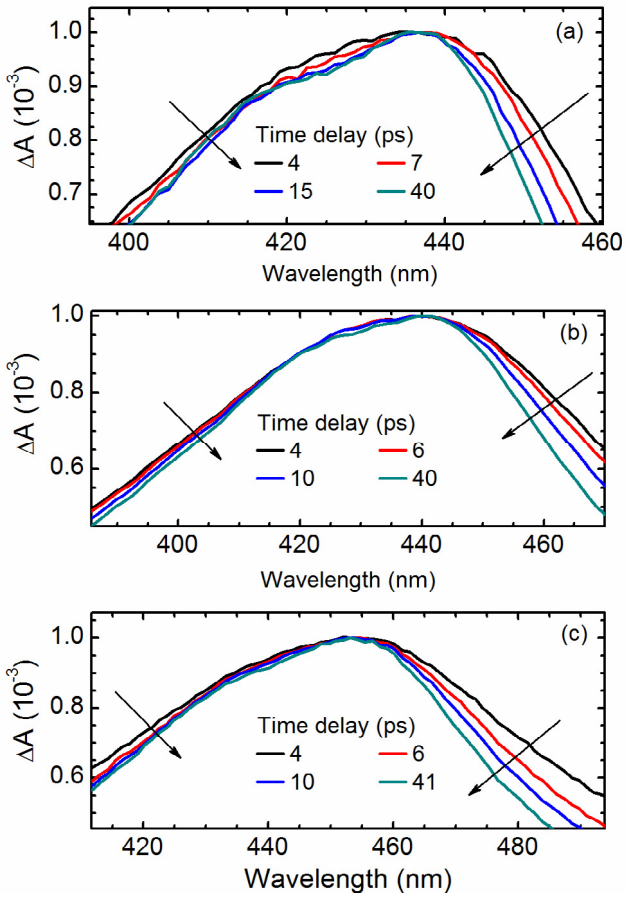

Figure 5.9. Normalized transient absorption spectra for (a) Cy_3PAu(2-naphthyl) (**1**), (b) $(Cy_3PAu)_2$(2,6-naphthalenediyl) (**2**), and (c) $(Cy_3PAu)_2$(2,7-naphthalenediyl) (**3**) in dichloromethane showing the narrowing, blue-shifting, and increased structuring characteristic of vibrational cooling dynamics.

compounds are primarily controlled by the strength of the spin-orbit interaction between the S_1 and T_n PES in the vicinity of the avoided crossing, the position in which the functional group is covalently linked (which themselves might reflect a change in the Franck-Condon overlap factors and topology of the PES), as well as, by how the energy and ordering of the excited states in the Franck-Condon region in the polycyclic aromatic compound are perturbed by the addition of the functional group. It will be interesting to verify if these observations can be

generalized in polycyclic aromatic compounds substituted with other functional groups or with other transition metals. Such systematic experiments have the potential to increase our understanding and ultimately control of the electronic and nuclear factors affecting the rate of intersystem crossing in organometallic compounds, currently being sought for a wide range of biological and technological applications.

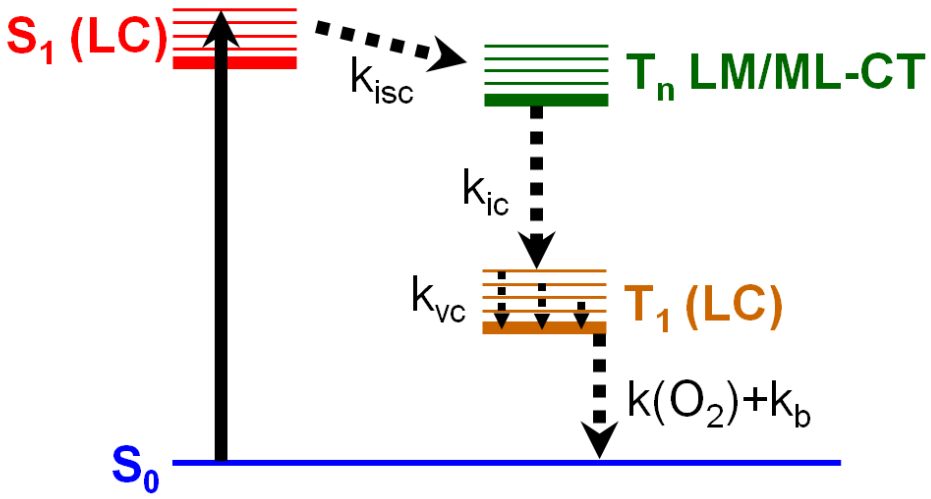

Scheme 5.1. Proposed sequential kinetic mechanism explaining the excited-state dynamics in Cy_3PAu(2-naphthyl) (**1**), $(Cy_3PAu)_2$(2,6-naphthalenediyl) (**2**), and $(Cy_3PAu)_2$(2,7-naphthalenediyl) (**3**) in dichloromethane. Intersystem crossing from the ligand-centered S_1 state to a receiver, high-energy T_n state with ligand-to-metal (in **2'** and **3'**) or metal-to-ligand (in **1'**) charge transfer character occurs with a rate constant k_{ISC} ~10^{12} to 10^{13} s^{-1}. Intersystem crossing possibly occurs in the strong non-adiabatic regime. The doorway T_n state internally converts with a rate constant k_{IC} ~5×10^{11} s^{-1} to populate the vibrationally-excited T_1 state. Vibrational cooling dynamics in the T_1 state occurs with a rate constant of k_{VC} ~5×10^{11} s^{-1}. Finally the T_1 state decays by two parallel bimolecular relaxation pathways. The major relaxation pathway is assigned to triplet quenching by molecular oxygen, $k(O_2)$, while the second, minor channel is tentatively assigned to triplet-triplet annihilation or self-quenching (k_b).

CONCLUSIONS

The electronic structure and excited-state dynamics of Cy_3PAu(2-naphthyl), $(Cy_3PAu)_2$(2,6-naphthalenediyl), and $(Cy_3PAu)_2$(2,7-naphthalenediyl) in dichloromethane are presented. We have resolved in time and in frequency the spectral signatures of the S_1, T_n, T_1(hot), and T_1(relaxed) states by using global and target analysis based on a sequential kinetic model. It is further shown that intersystem crossing to the triplet manifold occurs in hundreds of femtoseconds, presumably from the non-equilibrated S_1 state. The negligible $\Delta E(S_1 - T_n)$ energy gap and strength of the spin-orbit coupling interaction between the S_1 and the T_n PES in the region of the avoided crossing are proposed to explain the ultrafast singlet to triplet population transfer in these gold(I)-naphthalene compounds. Significantly, these aurated naphthalene compounds represent the first examples of gold(I) organometallic compounds exhibiting sub-picosecond intersystem crossing dynamics, thus, expanding the group of transition metals known to promote excited-state dynamics in the strongly non-adiabatic regime. As proposed initially by McCusker and co-workers for other organometallics,[169,176,178] our results challenge the view that the rate of internal conversion is larger than that of intersystem crossing, hence lending further support to the kinetic model proposed in other transition-metal complexes. The results presented in this work are expected to facilitate the rational design of the next generation of gold(I)-substituted organometallic monomers and oligomers with increased potential for applications as metallotherapeutic drugs, photodynamic therapy, organic near-infrared emitters, and/or sensing.[27,28-31]

EXPERIMENTAL AND COMPUTATIONAL METHODS

Broadband transient absorption spectrometer. The transient absorption spectrometer used in this work has been described in detail previously.[163,91] Briefly, the output of a Quantronix Integra-i/e 3.5 Laser (100 fs centered at 800 nm) is fed into an optical parametric amplifier (OPA, TOPAS, Quantronix/Light Conversion) generating the 266, 285, and 320 nm excitation pulses. Contributions from other wavelengths are removed by a reflective wavelength filter and a Glan-Taylor prism. Data are acquired using a broadband transient absorption spectrometer (Helios, Ultrafast Systems, LLC) with home-made LabView 8.6 software (National Instruments, Inc.). A continuously moving 2 mm CaF_2 crystal is used for continuum generation giving access to the spectral range from ~320 to 700 nm. The white-light probe pulses are corrected for group velocity dispersion.[40,91] The instrument response function of our experimental setup was estimated to be (250 $\pm$ 100) fs by using the coherent signal of solvent only (methanol) scans. The concentration used for compounds **1**, **2**, and **3** in these experiments were 4.4×10^{-4} M, 1.1×10^{-4} M, and 1.6×10^{-4} M, respectively. Compounds **1**, **2**, and **3** were excited at 285, 266, and 320 nm, respectively. These excitation wavelengths correspond to the red side of the absorption spectrum in each compound, thus, populating primarily the S_1 state.

Data analysis was performed using Igor Pro 6.12A software (Wavemetrics, Inc.). Nineteen decay traces were selected from the multidimensional data set for each compound at equidistance probe wavelengths and analyzed using a global fitting subroutine set up in the Igor Pro software. The

global and target analysis method[179,180] based on a sequential kinetic model[188] was used to obtain the excited-state lifetimes and decay associated spectra of the three naphthalene derivatives studied in this work. The sequential model rate law was composed of four exponential components.[188] This function was convoluted with a Gaussian-shaped instrument response function. When needed (Figure 5.2, right panel), a delta function was also included to model coherent solvent signals at some of the probe wavelengths. In the case of **1**, the lifetime of the fourth component does not decay within the 3.2 ns time window of our setup and it is denoted by $\tau_4 = \infty$ in Table 5.3. Its decay is likely associated to τ_5 in Table 5.3. The reported uncertainties for the lifetimes shown in Table 5.3 are twice the standard deviation (2σ) obtained from the global analysis of three independent set of experiments for each compound.

Transient absorption spectra of compounds **1** and **3** were also recorded from the picosecond to microsecond time scale using a photonic crystal fiber for probe light generation in the spectral range from ~400 to 675 nm (Eos, Ultrafast Systems, LLC). In this mode, a diode that monitors the light source is used as external trigger that synchronizes the femtosecond system. The light source is coupled to our femtosecond transient absorption spectrometer,[91] allowing the use the same setup for probing the excited-state dynamics from the picosecond to microsecond time scale. The concentration of **1** and **3** used in these experiments was $(4.8 \pm 0.5) \times 10^{-4}$ M and $(3.9 \pm 0.9) \times 10^{-4}$ M, respectively. Analogous experiments for **2** were impractical because it significantly degrades during the time required to collect the data (~5 to 10 min) at the excitation intensity used

(see below). Data acquisition was performed using home-made LabView 8.6 software. As for the femtosecond experiments, nineteen decay traces were selected from the multidimensional data set for each compound at equidistance probe wavelengths and analyzed using a global fitting subroutine set up in the Igor Pro software. The fitting subroutine consisted of an exponential decaying function convoluted with a Gaussian-shaped response function of 400 ps.

The probed volume of each sample was continuously renewed using a Teflon coated stir bar and a magnetic stirrer during all the transient absorption experiments performed in this work. The optical path length of the cell was 0.2 cm. The degradation of the compounds was monitored by using UV absorption spectroscopy and solutions were replaced by fresh ones if the steady-state absorbance at the excitation wavelength decreased by more than 5% during the course of the experiments. The excitation intensity used in all the transient absorption experiments was 2 μJ or less.

Ground- and Excited-State Quantum Chemical Calculations. All quantum-chemical calculations for Cy_3PAu(2-naphthyl) (**1**), $(Cy_3PAu)_2$(2,6-naphthalenediyl) (**2**), and $(Cy_3PAu)_2$(2,7-naphthalenediyl) (**3**) were performed with methyl groups in place of the cyclohexyl groups on phosphorus. They were performed to assist in the interpretation of the experimental data. Ground- and excited-state calculations were performed using the Gaussian09 suite of programs.[98] The ground-state geometries were optimized at the density functional level of theory (DFT) without imposed symmetry by using the parameter-free PBE0 functional[54] and the LANL2DZ[189] basis set. The optimized ground-state structures were

verified to be local minima on the potential energy surface by confirming that all vibrational frequencies have real values. Vertical and adiabatic excitation energies were calculated by using the time-dependent implementation of DFT with the PBE0 functional[54] and the LANL2DZ[189] basis set. Solvent effects were modeled by using the polarizable continuum model (PCM)[61] with the integral equation formalism (IEFPCM).[62] The equilibrium solvation model (E-IEFPCM) was used for all the calculations, except for the vertical excitation energies that used the non-equilibrium model (NE-IEFPCM). The non-equilibrium solvation model was used in the latter calculations because the aim in obtaining those vertical excitation energies was to determine the triplet state that acts as a doorway state in the sub-picosecond singlet-triplet population transfer. Solvation dynamics in the excited states typically occur in similar or slower time scales in other naphthalene derivatives.[91]

Chapter 6. General Experimental Methods

The laser used for all the experiments in this thesis is an *Integra-i/e 3.5* Laser (Quantronix, Inc) which is pumped with a Falcon (Quantronix, Inc). An Imra fiber oscillator provides the seed pulse which is amplified in the Integra.

The Falcon, used to pump the titanium sapphire crystals in the Integra, uses a flash lamp to pump a neodymium-doped yttrium lithium fluoride (Nd:YLF) rod. A schematic for the Falcon is shown in Figure 6.1. Both the flash lamp and the rod are contained in the pump chamber (h in Figure 6.1). After the Nd:YLF rod has built up a sufficient amount of energy the Q-switch becomes transparent and the energy from the rod is emitted via stimulated emission at 1053 nm. The Q-switch, or "quality" switch, consists of an acoustic-optic modulator and an RF driver. In this case the acoustic-optic modulator is a quartz plate. When the RF is turned off, light can travel through the quartz plate. When the RF is turned on the light experiences Bragg diffraction which scatters the beam and causes it to exit at a slightly different direction. The change in direction decreases the quality of the cavity and prevents the laser oscillating. Following the Q-switch, the 1053 nm light goes through a LiB_3O_5 (LBO) crystal where second harmonic generation occurs to form 527 nm light. The outcoupler (**a** in Figure 6.1) transmits 527 nm but reflects 1053 nm light. With a flash lamp current of 22 A it is typical for the Falcon to put out 14 W at 527 nm and 1 kHz.

The seed pulse, which is the low power short duration pulse that is amplified, is generated in an Imra. The Imra is a fiber oscillator which generates

100 fs pulses at 800 nm at 50 MHz. This pulse is fed into the Integra. The Integra is a chirped pulse amplifier which uses two titanium sapphire crystals, one in a regenerative amplifier and another in a multipass (Figure 6.2). The low energy pulse is stretched, or “chirped”, through the use of gratings. The stretched pulse is fed into the regenerative amplifier via a pockels cell. After traversing the cavity of the regenerative amplifier and making ~11 passes through the titanium sapphire the pulse is switched out with another pockels cell. The amplified pulse then goes through the Multipass where it passes through another titanium sapphire crystal twice. A third pockels cell is used to switch out the amplified pulse and clean up any residual seed pulses. Following the third pockels cell the pulse is compressed through a series of gratings back to ~100 fs. The beam characteristics are continuously monitored using a *GRENOUILLE* (Model 8-50, Swamp Optics), which is fed by the light transmitted through a high-reflective dielectric mirror. The method employed is based on the frequency-resolved optical gating (FROG) technique developed by Trebino and coworkers.[49]

After exiting the Integra, 1.2 W of the 800 nm, ~100 fs, 1 kHz pulses are fed into an optical parametric amplifier (OPA, TOPAS, Quantronix / Light Conversion) to generate the desired excitation pulses. Briefly, the OPA works by feeding one 800 nm pulse into a non-linear crystal (NLC) to generate two pulses, a signal and idler, which sum to the same energy as the 800 nm pulse. The wavelengths of the signal and idler can be tuned by adjusting the angle of NLC. This is the portion of the OPA that is the “parametric” part. Depending on the alignment of the OPA, the signal or the idler can then be amplified using 800 nm

light in two more passes through the same NLC. Using only one NLC in the OPA allows for a very compact system. After amplification, the light leaves the OPA. Second harmonic generation occurs two times after leaving the OPA. Any contributions to the excitation beam from other wavelengths or polarizations are effectively removed by a reflective wavelength filter (λ-filter) and a Glan-Taylor prism. A neutral density optical filter is used to attenuate the beam to the desired intensity (see below).

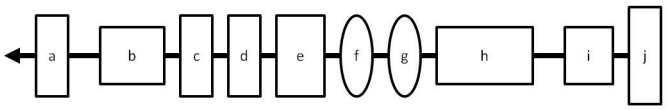

Figure 6.1. Schematic representation of the Falcon laser. Components are as follows: Outcoupler (a), second harmonic generation (b), high transmittance IR/high reflectance 532 nm (c), shutter (d), Q-switch (e), cylindrical lens (f), spherical lens (g), pump chamber (h), polarizer (i), and high reflectance mirror (j). The Falcon is used to pump the Integra.

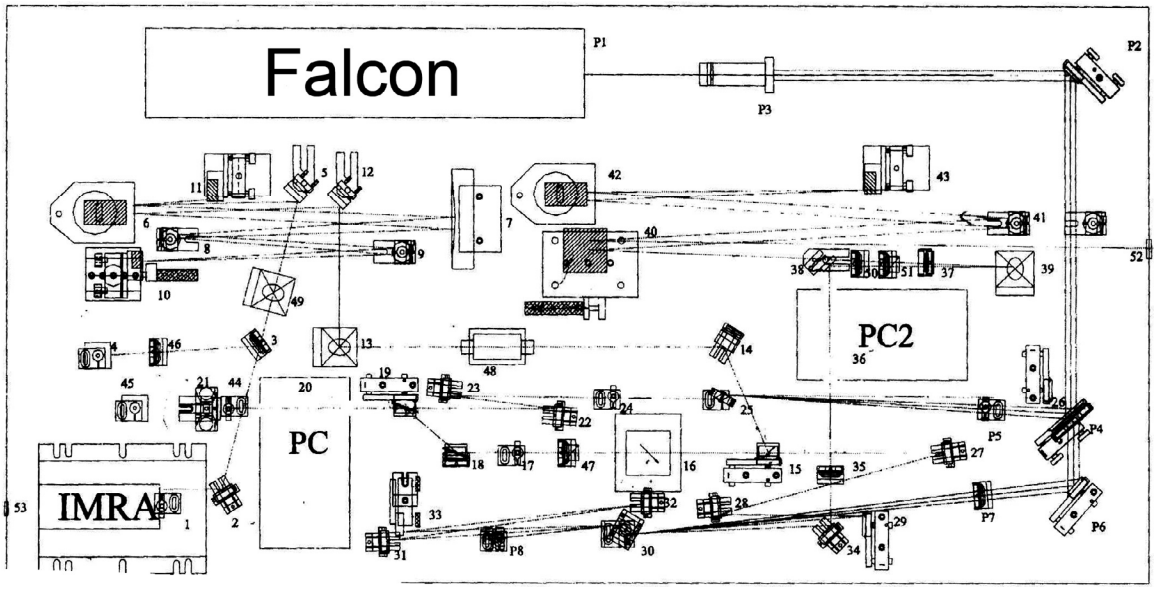

Figure 6.2. Schematic representation of the Integra. Image is based on the one in the Integra manual.

Broadband UV-Vis Transient Absorption

The detection method that I used for all the time-resolved laser experiments was transient absorption (Figure 6.3). Transient absorption is a pump-probe technique. The pump pulse is used to promote the sample into an excited state. In general, the probe pulse measures the depopulation of the ground state and the absorbance of the excited states, intermediate species, and products formed after excitation. The pump pulse is generated by the Integra and fed into the OPA to generate the user selectable wavelength. The ouput of the OPA goes into the Helios and Eos spectrometers. In the case of the Helios, the pump pulse goes through a chopper, a depolarizing plate and a lens which focuses the pump into the sample. The chopper blocks every other pulse. The depolarizer plate scrambles the polarization of the pump. To avoid anisotropy effects, transient absorption is usually done with the pump polarization at 54.7° relative to the probe polarization, which is known as the magic angle condition. To control the polarization a different halfwave plate would be needed for every different wavelength that the system can pump with. In the case of this research, to avoid needing many halfwave plates the pump pulse's polarization is scrambled by passing it through a depolarizer plate. The pump beam path for the Eos is the same as for the Helios except the chopper is not needed for the Eos.

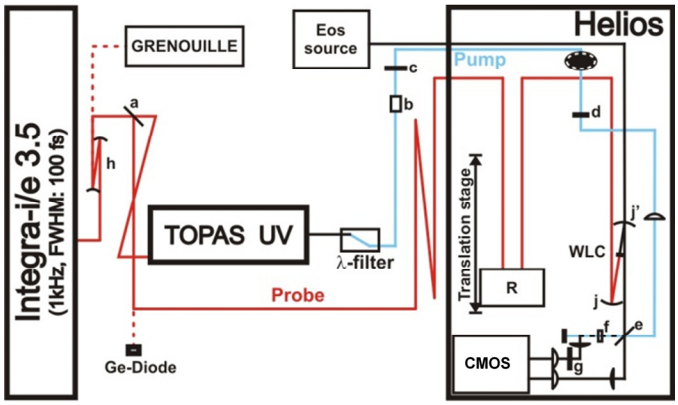

Figure 6.3. Schematic representation of the experimental setup used for the Helios. Key components are shown.

Two spectrometers were available for transient absorption, the Helios (Ultrafast Systems, Inc.) which allows transient absorption measurements to be made up to 3 ns with an IRF of ~200 fs and the EOS which allows measurements to be made up to 125 ms with an IRF of 500 ps. In the case of the Helios, the probe pulse is fed through a translation stage with a retroreflector which allows the path length that the probe travels to be varied. Increasing the pathlength increases the amount of time that it takes for the probe to reach the sample. White light is generated by focusing the 800 nm probe into a calcium fluoride (CaF_2) or sapphire crystal. The white light is focused and split, with one part going through the sample and to a detector and the other part going to the reference detector. The detectors are CMOS arrays and use a mirror/grating to disperse the incoming light onto the detectors. The intensity of the light is recorded at different delay times with the probe blocked and unblocked. The measurement of interest is the change of absorption caused by the pump. Absorbance is calculated using

$$A = \log\frac{I_o}{I} \quad (1)$$

where I_o is intensity of the light and I is intensity of light transmitted through the sample. Change in absorbance can be calculated using

$$\Delta A = A_{pumped} - A_{unpumped} \quad (2)$$

$$\Delta A = \log\frac{I_o^{pumped}}{I^{pumped}} - \log\frac{I_o^{unpumped}}{I^{unpumped}} = \log\left(\frac{I_o^{pumped}}{I^{pumped}}\frac{I^{unpumped}}{I_o^{unpumped}}\right) \quad (3)$$

where pumped/unpumped refers to the statues of the pump pulse and I_o is the intensity of the probe without passing through the sample. Upon simplifying the equation we get

$$\Delta A = \log\frac{I^{unpumped}}{I^{pumped}} \quad (4)$$

since the I_o values will cancel out. To correct for any shot-to-shot fluctuations in intensity a reference detector is used to normalize the intensities.

$$\Delta A = \log\frac{I_{probe}^{unpumped} I_{reference}^{pumped}}{I_{probe}^{pumped} I_{reference}^{unpumped}} \quad (5)$$

where probe/reference refer to which detector.

The software used was based on a home-made program that I created. LabVIEW 8.6 (National Instruments, Inc.) was used to control the instruments. The CMOS sensors used by the Helios spectrophotometer are Hamamatsu S10453-1024. The timing chart and pin-out information was readily available from Hamamatsu. The next step was designing new drivers to control the chips. A clock signal was generated using a National Instruments PCI-6602 DAQ card.

This clock signal was output to the detectors through a National Instruments PCI-6132 card along with a start signal. The PCI-6132 was also used to read the analog voltages corresponding to the intensity of light at each pixel of the detectors. The signals travelled along a National Instruments SH68-68-D1 cable to a home-made interface box which converted the signal from the SH68-68-D1 connector into individual VGA connectors that were connected to each detector. Another SH68-68-D1 cable was used to connect the PCI-6602 to another custom made interface box for outputting the trigger signal to the laser.

In addition to the Helios, the Eos (Ultrafast Systems, Inc.) was used for detection. The Eos uses a photonic crystal fiber to generate white light pulses at 8 kHz with widths of ~500 ps. The spectrum of the light source used in the Eos is shown in Figure 6.4. The upper limit of 750 nm is a result of a filter used to block

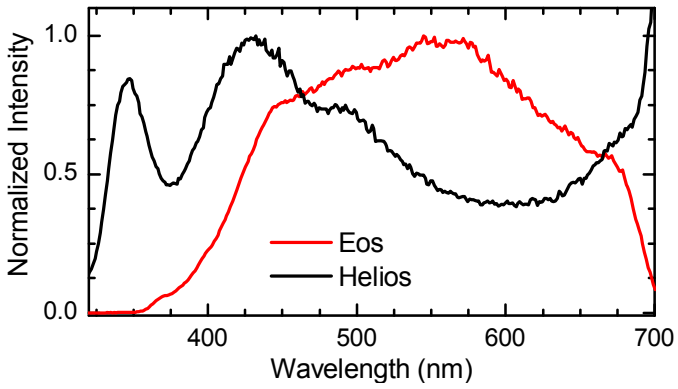

Figure 6.4. Spectrum of the white light continuum used as the probe for Eos and Helios systems.

residual 800 nm light which is inside the detector. Ultrafast systems states that the probe used in the Eos goes up to 900 nm. Similar to the Helios, the software for the Eos was home-made using LabVIEW 8.6. The system uses a Pendulum CNT-90 Frequency Timer/Counter/Analyzer (Pendulum, Inc) to measure the

delay between the pump and the probe signals. The 8 kHz pulse train from the white light source is used to trigger the Integra. Every eighth pulse, the Integra is fired at a user programmable delay time. Changing the delay time allows one to get the absorbance at various delay times and piece those together to see the evolution of the absorption with time. This is very similar to the Helios, except that instead of using a delay stage to delay the probe while keeping the pump constant, the computer delays the trigger signal to the Integra which delays the pump while keeping the probe constant. As the absorbance measurements are made, they are placed in to bins depending on their delay time. Each bin is averaged to give the absorbance corresponding to those delay times. The home-made software has the ability to automatically scan a range of delay times and the ability to control the size and number of bins. Designing this software was more challenging than the Helios software since the absorption measurements had to be perfectly synchronized with the time measurements. Since there was a small amount of uncertainty, or jitter, in the time that the laser would fire, the time and absorption measurements had to be perfectly synchronized or else the data appeared scrambled.

Steady-State Irradiation Experiments

Degradation Quantum Yields. In addition to the software and interface boxes for the Helios and Eos systems I also designed a shutter for the steady-state irradiation setup. This shutter implements a rotary solenoid (Lucas Ledex H-2346-032) which is triggered from the computer. Small pieces of metal are attached to the solenoid and rotated out of the beam path when the light needs to

be unblocked. For safety, the shutters' off position is blocking the beam. The solenoid is controlled via a home-made control box triggered through the parallel port. The software which controls the shutter was created using LabVIEW 8.6.

LabVIEW 8.6 was also used to develop a program for calculating the quantum yield of degradation. [103]

Potassium Ferrioxalate was used as an actinometer to measure the output of the Xe lamp (Newport Oriel 150 W Xe) using the following procedure which is similar to that used by Calvert and Pitt.[102] The spectrum of the lamp after filtering with a FGUV11S (Thorlabs, Inc.) filter is shown in Figure 6.5. The following solutions were made: 0.006 M Potassium ferrioxalate in 0.1N sulfuric acid was made by dissolving 0.2947g of potassium ferrioxalate in approximately 50 mL of clean water in a 100 mL fask. 10 mL of 1N sulfuric acid was added by volumetric pipet. The solution was diluted to 100 mL with water. The second solution made was a buffer combined with phenanthroline. To make this 36 mL of 1N sulfuric acid was added to 60 mL of 1N sodium acetate (NaO_2CCH_3) in a 100 mL volumetric flask. Solutions were diluted to ~80 mL before adding 0.100 g of 1,10-phenanthroline. The resulting solution was diluted to 100 mL. Both solutions proved to be stable for at least a couple months but were used within a week of preparation.

To measure the output of the lamp, 3.75 mL of the 0.006 M potassium ferrioxalate solution was placed in a 1 cm cuvette with a stir bar. The solution

was irradiated for 20 seconds with stirring. The reaction that takes place upon irradiation with light is

$$2\left[Fe\left(C_2O_4\right)_3\right]^{3-} + h\nu \rightarrow 2\left[Fe\left(C_2O_4\right)_2\right]^{2-} + {C_2O_4}^{2-} + 2CO_2 \qquad (6)$$

For every photon absorbed 2 ferrioxalate molecules can be destroyed. This allows potassium ferrioxalate to have a quantum yield greater than one. Following irradiation the solution was mixed with 1,10-phenanthroline in buffer to form ferrous tris-o-phenanthroline for this reaction

$$Fe^{2+} + 3C_{12}H_8N_2 \rightarrow \left[Fe\left(C_{12}H_8N_2\right)_3\right]^{2+} \qquad (7)$$

To perform this reaction, 0.48 mL of the irradiated potassium ferrioxalate solution, 0.32 mL of the buffer/phenanthroline solution and 3.20 mL water was placed into a 4 mL vial. The same quantities were measured into another 4 mL vial but the irradiated potassium ferrioxalate was exchanged for unirradiated potassium ferrioxalate. Both vials were capped and place in a dark place for 30 minutes. The absorbance of each solution was measured at 510 nm. The unirradiated solution was used as the baseline. The Beer-Lambert Law was used to calculate the concentration of the ferrous tris-o-phenanthroline formed in Equation 7. The epsilon for the complex formed is 11,150 $M^{-1}cm^{-1}$.[192]

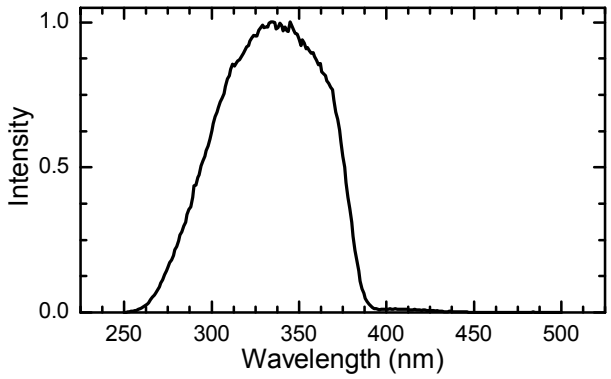

Figure 6.5. Spectrum of the light used for all steady-state irradiation experiments.

Since the experiments used polychromatic light, as shown in Figure 6.5, the calculation of the quantum yield was a little more complicated than if the experiments had used monochromatic light. The first step is to find the average quantum yield for the Potassium Ferrioxalate over the band of wavelengths that the lamp emits using

$$\Phi_{avg} = \frac{\Sigma E_\lambda \times \Phi_\lambda}{\Sigma E_\lambda} = \frac{\int_{\lambda_1}^{\lambda_2} E_\lambda \times \Phi_\lambda d\lambda}{\int_{\lambda_1}^{\lambda_2} E_\lambda d\lambda} \qquad (8)$$

where E is the relative incident photon flux at wavelength λ and φ is the quantum yield at wavelength λ. The relative incident photon flux was measured using a spectrometer prior to the quantum yield measurements and is shown in Figure 6.5. The procedure is similar to that of Chen et al.[191] Experimental Potassium Ferrioxalate quantum yields were taken from Murov et al.[192] The intensity of the lamp is calculated using the average quantum yield with the following equation

$$I_o = \frac{N_{Fe^{2+}}}{t \times \Phi_{avg}} \quad (9)$$

where I_o is the intensity of the lamp in photons per second, N_{Fe2+} is the number of Fe^{2+} ions formed and t is time irradiated. In the wavelength range that was used for irradiation, see Figure 6.5, the average quantum yield is 1.227.

Once the output of the lamp has been measured the degradation of the sample of interest can be measured. A known volume of a solution with a known concentration was added to the same cuvette used for the actinometer. A volume of 3.75 mL worked well using the 1 cm red screw cap cuvette (Starna, Inc). A stir bar (Starna, Inc) was added and the cuvette was capped. The initial absorbance was measured using the UV/Vis spectrometer (Varian, Inc. Cary 100). This value will be called $A_{(\lambda)}$. A known volume of the solution was removed and injected into the HPLC. The current HPLC system has a 20 μL sample loop, good results have been obtained by injecting 100 μL into the sample loop which assures that the sample loop is homogenous with the sample. The volume removed will be called x. The sample was irradiated for an amount of time sufficient to cause 1 to 5% degradation. Time irradiated is called t. The irradiation and injection into the HPLC were repeated until a sufficient number of data points were collected, usually 5 points. In the case of freeze-pump-thaw experiments, the sample was irradiated only one time. Since the cuvette had to be opened to remove the sample it was not possible to do multiple points. However, multiple trials were performed in that case. The total amount of sample degraded should be less than 20% to minimize the amount of light that is absorbed by the photoproducts.

The quantum yield of the unknown sample can be calculated next. First, the number of molecules that the light degraded needs to be calculated. The concentrations at each time were calculated using the HPLC peak areas and a HPLC calibration curve. The total number of molecules destroyed at each time was calculated. Because the volume is changing the change in concentration between each data point was used to calculate the number of molecules destroyed. The changes are summed to find the total number of molecules destroyed at each time

The next step is to calculate the number of photons absorbed. First, the absorbance of the compound was calculated at each time using Equation 10 at each time. According to the Beer-Lambert law absorbance is proportional to concentration. Since the concentration is known (from the HPLC results) the absorbance at each concentration can be calculated using

$$Absorbance_{time=t} = \frac{concentation_{time=t}}{concentration_{time=0}} \times Absorbance_{time=0} \quad (10)$$

The fraction of the photons absorbed was then calculated using

$$FracA_{\lambda} = 1 - 10^{-A_{(\lambda)}} \quad (11)$$

where $A_{(\lambda)}$ is absorbance at wavelength λ. Using the result of the previous equation the fraction of photons over the entire range of wavelengths can be calculated using

$$FracA = \frac{\int_{\lambda_1}^{\lambda_2} E_{(\lambda)} \times FracA_{(\lambda)} d\lambda}{\int_{\lambda_1}^{\lambda_2} E_{(\lambda)} d\lambda} \quad (12)$$

where E is the relative intensity of the lamp. The number of photons is calculated using

$$I_a = FracA \times I_o \quad (13)$$

The fraction of photons absorbed will change with the concentration and must be recalculated for each concentration. The number of photons absorbed from the beginning of the irradiation to the current time point was found using

$$I_{a_{Total}} = \sum_{0}^{t_f} (I_{a_{(t=n)}} \times \Delta t) \quad (14)$$

Finally, the quantum yield of degradation can be calculated by graphing the number of molecules destroyed vs. the number of photons absorbed as shown in Equation 15.

$$\Delta N_{nitronaphthalene} = \phi \times I_a \quad (15)$$

The slope will be the degradation quantum yield.

Fluorescence Quantum Yields. The fluorescence quantum yield is the number of photons emitted per photon absorbed. A standard is used as a reference to calculate the fluorescence quantum yield using Equation 16.[193]

$$\phi_{un} = \phi_R \times \frac{Int_{un}}{Int_R} \frac{A_R}{A_{un}} \frac{\eta_{un}^2}{\eta_R^2} \quad (16)$$

where ϕ is the fluorescence quantum yield, Int is the integral of the fluorescence band, η is the refractive index and subscripts R and un refer to the reference sample and the unknown sample, respectively.

Chapter 7. Future Work

The focus of this research was on nitro and organophosphine gold(I) naphthalenes and organophosphine gold(I) pyrenes. It would be useful to extend this research into derivatives with other numbers of rings. The next logical step would be the anthracenes which are similar to the naphthalenes but have one more ring. This would reveal trends between the photodynamics and the size of the poly cyclic aromatic hydrocarbon (PAH) portion of the molecules. In addition, it would be interesting to take a look at di substituted nitro-PAH compounds. This research has demonstrated that adding a nitro group to a naphthalene greatly enhances the intersystem crossing. Can the intersystem crossing be enhanced even more by adding more nitro groups? Further down the road, the mechanisms demonstrated in this thesis should be applied to advance pollution control strategies.

Chapter 8. References

1. Tong, H. Y.; Karasek, F. W., *Anal. Chem.* **1984,** *56*, 2129.

2. Cass, G. R.; Hughes, L. A.; Bhave, P.; Kleeman, M. J.; Allen, J. O.; Salmon, L. G., *Philos. Trans. Royal Soc. London Ser. A* **2000,** *358*, 111.

3. Yu, H., *J. Environ. Sci. Health C* **2002,** *C20*, 149.

4. In IPCS INCHEM (2003) Selected Nitro- and Nitro-Oxy-Polycyclic Aromatic Hydrocarbons. Environmental Health Criteria (EHC) Monographs, No. 229: WHO, Geneva, 2003.

5. Diesel and Gasoline Engine Exhausts and Some Nitroarenes. In *IARC Monographs on the Evaluation of Carcinogenic Risks to Humans*, World Health Organization, International Agency for Research on Cancer: No. 46, Lyon, France, 1989.

6. Atkinson, R.; Arey, J., *Environ. Health Perspect.* **1994,** *102*, 117.

7. Arey, J.; Zielinska, B.; Atkinson, R.; Winer, A. M., *Mutat. Res.* **1988,** *207*, 45.

8. Arey, J.; Atkinson, R., Photochemical Reactions of PAHs in the Atmosphere. In *PAHs: An Ecotoxicological Perspective*, Douben, P. E. T., Ed. John Wiley & Sons: Chichester, England, 2003; pp 47-63.

9. Tokiwa, H.; Ohnishi, Y., *CRC Crit. Rev. Toxicol.* **1986,** *17*, 23.

10. Möller, L., *Environ. Health Perspect.* **1994,** *102*, 139.

11. Purohit, V.; Basu, A. K., *Chem. Res. Toxicol.* **2000,** *13*, 673.

12. Arlt, V. M., *Mutagenesis* **2005,** *20*, 399.

13. Kamiya, A.; Ose, Y., *Sc. Total Environ.* **1988,** *72*, 1.

14. Henderson, T. R.; Sun, J. D.; Royer, R. E.; Clark, C. R.; Li, A. P.; Harvey, T. M.; Hunt, D. H.; Fulford, J. E.; Lovette, A. M.; Davidson, W. R., *Environ. Sci. Technol.* **1983,** *17*, 443.

15. Handa, T.; Yamauchi, T.; Sawai, K.; Yamamura, T.; Koseki, Y.; Ishii, T., *Environ. Sci. Technol.* **1984,** *18*, 895.

16. Hönor, A.; Arnold, M.; Hüsers, N.; Kleiböhmer, W., *J. Chromatogr. A* **1995,** *710*, 129.

17. Schauer, C.; Nierrner, R.; Pöschl, U., *Anal. Bioanal. Chem.* **2004,** *378*, 725.

18. Tokiwa, H.; Sera, N.; Horikawa, K.; Nakanishi, Y.; Shigematu, N., *Carcinogenesis* **1993,** *14*, 1933.

19. Kamens, R. M.; Zhi-Hua, F.; Yao, Y.; Chen, D.; Chen, S.; Vartiainen, M., *Chemosphere* **1994,** *28*, 1623.

20. Fan, Z.; Chen, D.; Birla, P.; Kamens, R. M., *Atmos. Environ.* **1995,** *29*, 1171.

21. Fan, Z.; Kamens, R. M.; Hu, J.; Zhang, J.; McDow, S., *Environ. Sci. Technol.* **1996,** *30*, 1358.

22. Feilberg, A.; Kamens, R. M.; Strommen, M. R.; Nielsen, T., *Atmos. Environ.* **1999,** *33*, 1231.

23. Feilberg, A.; Nielsen, T., *Environ. Sci. Technol.* **2000,** *34*, 789.

24. Feilberg, A.; Nielsen, T., *Environ. Sci. Technol.* **2001,** *35*, 108.

25. Arce, R.; Pino, E. F.; Valle, C.; Ágreda, J., *J. Phys. Chem. A* **2008,** *121*, 10294.

26. Katarina, V., *Mutat. Res.* **1994,** *317*, 43.

27. Allendorf, M. D.; Bauer, C. A.; Bhakta, R. K.; Houk, R. J. T. *Chem. Soc. Rev.* **2009**, *38*, 1330.

28. Ho, S. Y.; Tiekink, E. R. T. In Metallotherapeutic Drugs & Metal-Based Diagnostic Agents: The Use of Metals in Medicine; Gielen, M., Tiekink, E. R. T., Eds.; Wiley: New York, 2005; pp 507-528.

29. Partyka, D. V.; Zeller, M.; Hunter, A. D.; Gray, T. G. *Angew. Chem. Int. Ed.* **2006**, *45*, 8188.

30. Lima, J. C.; Rodrígues, L. *Chem. Soc. Rev.* **2011**, *40*, 5442.

31. Raubenheimer, H. G.; Schmidbaur, H. *Organometallics* **2012**, *31*, 2507.

32. Craig, S.; Gao, L.; Lee, I.; Gray, T.; Berdis, A. J. *J. Med. Chem.* **2012**, *55*, 2437.

33. Partyka, D. V.; Teets, T. S.; Zeller, M.; Updegraff, J. B., III;; Hunter, A. D.; Gray, T. G. *Chem. Eur. J.* **2012**, *18*, 2100.

34. Gao, L.; Niedzwiecki, D. S.; Deligonul, N.; Zeller, M.; Hunter, A. D.; Gray, T. G. *Chem. Eur. J.* **2012**, *18*, 6316.

35. Turro, N.J. *Modern Molecular Photochemistry*, 1st ed. (University Science Books, Sausalito, CA, 1991).

36. Döpp, D. in *CRC Handbook of Organic Photochemistry and Photobiology*, edited by W. Horspool and P.-S. Song (CRC Press, Inc., Boca Raton, FL, 1995), pp. 1019.

37. V. Katarina, *Mutat. Res*. **1994**, *317*, 43.

38. Morales-Cueto, R.; Esquivelzeta-Rabell, M.; Saucedo-Zugazagoitia, J.; Peon, J. *J. Phys. Chem. A* **2007**, *111*, 552.

39. Mohammed, O. F.; Vauthey, E. *J. Phys. Chem. A* **2008**, *112*, 3823.

40. Crespo-Hernández, C. E.; Burdzinski, G.; Arce, R. **2008**, *J. Phys. Chem. A* *112*, 6313.

41. Zugazagoitia, J. S.; Almora-Díaz, C. X.; Peon, J. *J. Phys. Chem. A* **2008**, *112*, 358.

42. Zugazagoitia, J. S.; Collado-Fregoso, E.; Plaza-Medina, E. F.; Peon, J. *J. Phys. Chem. A* **2009**, *113*, 805.

43. Hurley, R.; Testa, A. C. *J. Am. Chem. Soc.* **1968**, *90*, 1949.

44. Rusakowicz, R.; Testa, A. C. *Spectrochim. Acta.* **1971**, *27A*, 787.

45. Mikula, J. J.; Anderson, R. W.; Harris, L. E.; Stuebing, E. W. *J. Mol. Spec.* **1972**, *42*, 350.

46. Mikula, J. J.; Anderson, R. W.; Harris, L. E. *Adv. Mol. Relax. Proc.* **1973**, *5*, 193.

47. Capellos, C.; Porter, G. *J. Chem. Soc. Faraday Trans. 2* **1974**, 70, 1159.

48. Anderson Jr., R. W.; Hochstrasser, R. M.; Lutz, H.; Scott, G. W. *Chem. Phys. Lett.* **1974**, *28*, 153.

49. Trebino, R.; DeLong, K. W.; Fittinghoff, D. N.; Sweetser, J. N.; Krumbügel, M. A.; Richman, B. A.; Kane, D. J. *Rev. Sci. Instrum.* **1997**, *68*, 3277.

50. Maciejewski, A.; Naskrecki, R.; Lorenc, M.; Ziolek, M.; Karolczak, J.; Kubicki, J.; Matysiak, M.; Szymanski, M. *J. Mol. Struc.* **2000**, *555*, 1; Lorenc, M.; Ziolek, M.; Naskrecki, R.; Karolczak, J.; Kubicki, J.; Maciejewski, A. *Appl. Phys. B: Laser Opt*. **2002**, *87*, 2340.

51. Nakayama, T.; Amijima, Y.; Ibuki, K.; Hamanoue, K. *Rev. Sci. Instrum.* **1997**, *68*, 4364.

52. Frisch, M. J.; Trucks, G. W.; Schlegel, H. B.; Scuseria, G. E.; Robb, M. A.; Cheeseman, J. R.; Zakrzewski, V. G.; Montgomery Jr., J. A.; Stratmann, R. E.; Burant, J. C.; Dapprich, S.; Millam, J. M.; Daniels, K. N.; Kudin, K. N.; Strain, M. C.; Farkas, O.; Tomasi, J.; Barone, V.; Cossi, M.; Cammi, R.; Mennucci, B.; Pomelli, C.; Adamo, C.; Clifford, S.; Ochterski, J.; Petersson, G. A.; Ayala, P. Y.; Cui, Q.; Morokuma, K.; Malick, D. K.; Rabuck, A. D.; Raghavachari, K.; Foresman, J. B.; Cioslowski, J.; Ortiz, J. V.; Baboul, A. G.; Stefanov, B. B.; Liu, G.; Liashenko, A.; Piskorz, P.; Komaromi, I.; Gomperts, R.; Martin, R. L.; Fox, D. J.; Keith, T.; Al-Laham, M. A.; Peng, C. Y.; Nanayakkara, A.; Gonzalez, C.; Challacombe, M.; Gill, P. M. W.; Johnson, B. G.; Chen, W.; Wong, M. W.; Andres, J. L.; Head-Gordon, M.; Replogle, E. S.; Pople, J. A.; Gaussian 03 (Revision D.01) (Gaussian, Inc., Wallingford CT: Pittsburgh, PA, 2004).

53. Becke, A. D. *J. Chem. Phys.* **1993**, *98*, 1372.; Lee, C.; Yang, W.; Parr, R. G.; *Phys. Rev.* **1988**, *B37*, 785.

54. Adamo C.; Barone, V. *J. Chem. Phys.* **1999**, *110*, 6158; Adamo, C.; Scuseria, G. E.; Barone, V. *J. Chem. Phys.* **1999**, *111*, 2889.

55. Crespo-Hernández, C. E.; Cohen, B.; Hare, P. M.; Kohler, B. *Chem. Rev.* **2004**, *104*, 1977.

56. Raganato, M. F.; Vitale, V.; Della Sala, F.; Anni, M.; Cingolani, R.; Gigli, G.; Favaretto, L.; Barbarella, G.; Weimer, M.; Görling, A.; *J. Chem. Phys.* **2004**, 121, 3784; Jacquemin, D.; Wathelet, V.; Perpète, E. A.; Adamo, C. *J. Chem. Theory Comput.* **2009**, *5*, 2420.

57. Fabiano, E.; Della Sala, F.; Barbarella, G.; Lattante, S.; Anni, M.; Sotgiu, G.; Hättig, C.; Cingolani, R.; Gigli, G. *J. Phys. Chem. B* **2006**, *110*, 18651.

58. Mennucci, B.; Toniolo, A.; Tomasi, J. *J. Phys. Chem. A* **2001**, *105*, 4749.

59. Improta, R.; Barone, V.; Santoro, F.; *J. Phys. Chem. B* **2007**, *111*, 14080. Jacquemin, D.; Preat, J.; Wathelet, V.; Fontaine, M.; Perpète, E. A. *J. Am. Chem. Soc.* **2006**, *128*, 2072.

60. Gustavsson, T.; Sarkar, N.; Lazzarotto, E.; Markovitsi, D.; Barone, V.; Improta, R. *J. Phys. Chem. B* **2006**, *110*, 12843; Improta, R.; Scalmani, G.; Frisch, M. J.; Barone, V. *J. Chem. Phys.* **2007**, *127*, 074504.

61. Barone, V.; Cossi, M.; Tomasi, J. *J. Chem. Phys.***1997**, *107*, 3210.

62. Cances, M. T.; Mennucci, V.; Tomasi, J. *J. Chem. Phys.* **1997**, *107*, 3032.

63. Tomasi, J.; Mennucci, B.; Cammi, R. *Chem. Rev.* **2005**, *105*, 2999.

64. Takezaki, M.; Hirota, N.; Terazima, M.; Sato, H.; Nakajima, T.; Kato, S. *J. Phys. Chem. A* **1997**, *101*, 5190; Farztdinov, V. M.; Schanz, R.; Kovalenko, S. A.; Ernsting, N. P. *J. Phys. Chem. A* **2000**, *104*, 11486; Takezaki, M.; Hirota, N.; Terazima, M. *J. Phys. Chem. A* **1997**, *101*, 3443.

65. Kovalenko, S. A.; Schanz, R.; Farztdinov, V. M.; Hennig, H.; Ernsting, N. P. *Chem. Phys. Lett.* **2000**, *323*, 312.

66. Onchoke, K. K.; Hadad, C. M.; Dutta, P. K. *Polycycl. Arom. Compd.* **2004**, *24*, 37.

67. El-Sayed, M. A.; *J. Chem. Phys.* **1962**, 36, 573; El-Sayed, M. A. *J. Chem. Phys.* **1963**, *38*, 2834.

68. See EPAPS supplementary material at http://dx.doi.org/10.1063/1.3272536 for LUMO and HOMO molecular orbitals for optimized 1NN in cyclohexane, acetonitrile, and methanol at the TD-PBE0/ NE-IEFPCM/6-311++G(d,p) || B3LYP/IEFPCM/6-311++G (d,p) level of theory.

69. Elsaesser T.; Kaiser, W. Ann. *Rev. Phys. Chem.* **1991**, *42*, 83;

70. Owrutsky, J. C.; Raftery, D.; Hochstrasser, R. M. *Ann. Rev. Phys. Chem.* **1994**, *45*, 519.

71. Nibbering, E. T. J.; Elsaesser, T. *Chem. Rev.* **2004**, *104*, 1887.

72. Kovalenko, S. A.; Schanz, R.; Henning, H.; Ernsting, N. P. *J. Chem. Phys.* **2001**, *115*, 3256.

73. Elles, C. G.; Crim, F. F. *Ann. Rev. Phys. Chem.* **2006**, *57*, 273.

74. Horng, M. L.; Gardecki, J. A.; Papazyan, A.; Maroncelli, M. *J. Phys. Chem.* **1995**, *99*, 17311.

75. Reynolds, L.; Gardecki, J. A.; Frankland, S. J. V.; Horng, M. L.; Maroncelli, M. *J. Phys. Chem.* **1996**, *100*, 10337.

76. Glasbeek, M.; Zhang, H. *Chem. Rev.* **2004**, *104*, 1929.

77. Ladany, B. M.; Stratt, R. M. *J. Phys. Chem.* **1996**, *100*, 1266.

78. Letsinger, R. L.; Wubbels, G. G. *J. Am. Chem. Soc.* **1966**, *88*, 5041; Hashimoto, S.; Sunamoto, J.; Fujii, H.; Kano, K.; *Bull. Chem. Soc. Jpn.* **1968**, *41*, 1249; Trotter, W.; Testa, A. C. *J. Phys. Chem.* **1970**, *74*, 845; Hashimoto, S.; Ueda, K.; Kano, K. *Bull. Chem. Soc. Jpn.* **1971**, *44*, 1102; Wubbels, G. G.; Jordan, J. W.; Millis, N. S. *J. Am. Chem. Soc.* **1973**, *95*, 1281; Cu, A.; Testa, A. C.; *J. Phys. Chem.* **1973**, *77*, 1487; Wubbels, G. G.; Letsinger, R. L. *J. Am. Chem. Soc.* **1974**, *96*, 6698; Cu, A.; Testa, A. C. *J. Am. Chem. Soc.* **1963**, *96*, 1963; Cu, A.; Testa, A. C.; *J. Phys. Chem.* **1975**, *79*, 644; Wubbels, G. G.; Snyder, E. J.; Coughlin, E. B. *J. Am. Chem. Soc.* **1988**, *110*, 2543; Nakagaki R.; Mutai, K. *Bull. Chem. Soc. Jpn.* **1996**, *69*, 261.

79. Vogt, R. A.; Reichardt, C.; Crespo-Hernández, C. E. Unpublished results.

80. Sakamoto, M.; Cai, X.; Hara, M.; Fujitsuka, M.; Majima, T. *J. Am. Chem. Soc.* **2004**, *126*, 9709;

81. Sakamoto, M.; Cai, X.; Hara, M.; Fujitsuka, M.; Majima, T. *J. Phys. Chem. A* **2005**, *109*, 4657.

82. Englman, R.; Jortner, J. *Mol. Phys.* **1970**, *18*, 145;

83. Freed, K. F.; Jortner, J. *J. Chem. Phys.* **1970**, *52*, 6272.

84. Chapman, O. L.; Heckert, D. C.; Reasoner, J. W.; Thackaberry, S. P. *J. Am. Chem. Soc.* **1966**, *88*, 5550.

85. Hamanoue, K.; Nakayama, T.; Ushida, K.; Kajiwara, K.; Yamanaka, S. *J. Chem. Soc. Faraday Trans.* **1991**, *87*, 3365.

86. Hamanoue, K.; Nakayama, T.; Kajiwara, K.; Yamanaka, S. *J. Chem. Soc. Faraday Trans.* **1992**, *88*, 3145.

87. Hamanoue, K.; Nakayama, T.; Amijima, Y.; Ibuki, K. *Chem. Phys. Lett.* **1997**, *267*, 165;

88. Brown, H. W.; Pimentel, G. C. *J. Chem. Phys.* **1958**, *29*, 883.

89. Lide, D. R. *CRC Handbook of Chemistry and Physics*, 56 ed. (CRC Press Cleveland, Cleveland, OH, 1975).

90. Ciocirlan, O.; Iulian, O. *J. Serb. Chem. Soc.* **2009**, *74*, 317.

91. Reichardt, C.; Vogt, R. A.; Crespo-Hernández, C. E. *J. Chem. Phys.* **2009**, *131*, 224518.

92. Vyas, S.; Onchoke, K. K.; Rajesh, C. S.; Hadad, C. M.; Dutta, P. K. *J. Phys. Chem. A* **2009**, *113*, 12558.

93. Arce, R.; Pino, E. F.; Valle, C.; Negrón-Encarnación, I.; Morel, M. *J. Phys. Chem. A* **2011**, *115*, 152.

94. Plaza-Medina, E. F.; Rodríguez-Córdoba, W.; Morales-Cueto, R.; Peon, J. *J. Phys. Chem. A* **2011**, *115*, 577.

95. Wehry, E. L. Effects of Molecular Structure on Fluorescence and Phosphorescence. In *Practical Fluorescence*; 2 ed.; Guilbault, G. G., Ed.; Marcel Dekker, Inc.: New York, 1990; pp 75-125.

96. Warner, S. D.; Farant, J.-P.; Butler, I. S. *Chemosphere* **2004**, *54*, 1207.

97. Vogt, R. A.; Rahman, S.; Crespo-Hernández, C. E. Structure-Activity Relationships in Nitro-Aromatic Compounds. In *Practical Aspects of Computational Chemistry*; Leszczynski, J., Shukla, M. K., Eds.; Springer Science+Business Media: Netherlands, 2009; pp 217-240.

98. Frisch, M. J.; Trucks, G. W.; Schlegel, H. B.; Scuseria, G. E.; Robb, M. A.; Cheeseman, J. R.; Scalmani, G.; Barone, V.; Mennucci, B.; Petersson, G. A.; Nakatsuji, H.; Caricato, M.; Li, X.; Hratchian, H. P.; Izmaylov, A. F.; Bloino, J.; Zheng, G.; Sonnenberg, J. L.; Hada, M.; Ehara, M.; Toyota, K.; Fukuda, R.; Hasegawa, J.; Ishida, M.; Nakajima, T.; Honda, Y.; Kitao, O.; Nakai, H.; Vreven, T.; Montgomery Jr., J. A.; Peralta, J. E.; Ogliaro, F.; Bearpark, M.; Heyd, J. J.; Brothers, E.; Kudin, K. N.; Staroverov, V. N.; Kobayashi, R.; Normand, J.; Raghavachari, K.; Rendell, A.; Millam, J. M.; Klene, M.; Knox, J. E.; Cross, J. B.; Bakken, V.; Adamo, C.; Jaramillo, J.; Gomperts, R.; Stratmann, R. E.; Yazyev, O.; Austin, A. J.; Cammi, R.; Pomelli, C.; Ochterski, J.; Martin, R. L.; Morokuma, K.; Zakrzewski, V. G.; Voth, G. A.; Salvador, P.; Dannenberg, J. J.; Dappich, S.; Daniels, A. D.; Farkas, O.; Foresman, J. B.; Ortiz, J. V.; Cioslowski, J.; Fox, D. J.; Gaussian 09 (Revision A.01), Gaussian, Inc.: Wallingford, CT, 2009.

99. Becke, A. D. *J. Chem. Phys.* **1993**, *98*, 5648.

100. Crespo-Hernández, C. E.; Flores, S.; Torres, C.; Negrón-Encarnación, I.; Arce, R. *Photochem. Photobiol.* **2000**, *71*, 534.

101. Crespo-Hernández, C. E.; Arce, R. *Photochem. Photobiol.* **2000**, *71*, 544.

102. Calvert, J. G.; Pitts, J. N. In *Photochemistry*; Wiley: New York, **1966**; pp 783-786.

103. Dodson, L.; Vogt, R. A.; Reichardt, C.; Marks, J.; Crespo-Hernández, C. E. *Chemosphere* **2011**, *83*, 1513.

104. Carmichael, I.; Hug, G. L. *J. Phys. Chem. Ref. Data*, **1986**, *15*, 1.

105. Horrocks, A.R.; Wilkinson, F. *Proceedings of the Royal Society of London Series A, Mathematical and Physical Sciences.* **1968,** *306*, 257.

106. Dreuw, A.; Weisman, J. L.; Head-Gordon, M. *J. Chem. Phys.* **2003**, *119*, 2943.

107. Dreuw, A.; Head-Gordon, M. *Chem. Rev.* **2005**, *105*, 4009.

108. Richard, R. M.; Herbert, J. M. *J. Chem. Theory Compt.* **2011**, *7*, 1296.

109. Turro, N. J.; Ramamurthy, V.; Scaiano, J. C. *Principles of Molecular Photochemistry: An Introduction*; University Science Books: Sausalito, CA, 2009.

110. Geske, D. H.; Ragle, J. L.; Bambenek, M. A.; Balch, A. L. *J. Am. Chem. Soc.* **1964**, *86*, 987.

111. Dirk, J. A.; Ridder, D.; Schenk, H. *Acta Cryst.* **1995**, *B51*, 221.

112. Barrows, S. E.; Cramer, C. J.; Truhlar, D. G. *Environ. Sci. Technol.* **1996**, *30*, 3028.

113. He, X.; Lam, W. H.; Zhu, N.; Yam, V. W.-W. *Chem. Eur. J.* **2009**, *15*, 8842.

114. Castellano, F. N.; Pomestchenko, I. E.; Shikhova, E.; Hua, F.; Muro, M. L.; Rajapakse, N. *Coord. Chem. Rev.* **2006**, *250*, 1819.

115. Wong, K. M-C.; Yam, V. W.-W. *Coord. Chem. Rev.* **2007**, *251*, 2477.

116. Rachford, A. A.; Hua, F.; Adams, C. J.; Castellano, F. N. *Dalton Trans.* **2009**, 3950.

117. Ratilla, E. M. A.; Brothers, H. M., II; Kostić , N. M. *J. Am. Chem. Soc.* **1987**, *109*, 4592.

118. Williams, J. A. G.; Develay, S.; Rochester, D. L.; Murphy, L. *Coord. Chem. Rev.* **2008**, *252*, 2596.

119. Murphy, L.; Williams, J. A. G. *Top. Organomet. Chem.* **2010**, *28*, 75.

120. Jiang, F.-L.; Fortin, D.; Harvey, P. D. *Inorg. Chem.* **2010**, *49,* 2614.

121. Sun, W.; Wu, Z.-X.; Yang, Q.-Z.; Wu, L.-Z.; Tung, C.-H. *Appl. Phys. Lett.* **2003**, *82*, 850.

122. Guo, F.; Sun, W.; Liu, Y.; Schanze, K. Synthesis, *Inorg. Chem.* **2005**, *44*, 4055.

123. Hagfeldt, A.; Grätzel, M. Molecular Photovoltaics. *Acc. Chem. Res.* **2000**, 33, 269.

124. Zhang, J.; Du, P.; Schneider, J.; Jarosz, P.; Eisenberg, R. *J. Am. Chem. Soc.* **2007**, *129*, 7726.

125. Lower, S. K.; El-Sayed, M. A. *Chem. Rev.* **1966***, 66,* 199.

126. Gorin, D. J.; Toste, F. D. *Nature* **2007**, *446*, 395.

127. Kaltsoyannis, N. *J. Chem. Soc., Dalton Trans.* **1997**, 1.

128. Fernández, E. J.; Laguna, A.; Olmos, M. E. *Adv. Organomet. Chem.* **2005**, *52*, 77.

129. Chao, H.-Y.; Lu, W.; Li, Yi.; Chan, M. C. W.; Che, C.-M.; Cheung, K.-K.; Zhu, N. *J. Am. Chem. Soc.* **2002**, *124*, 14696.

130. Gray, T. G. *Comments Inorg. Chem.* **2007**, *28*, 181.

131. Partyka, D. V.; Robilotto, T. J.; Updegraff, J. B. III; Zeller, M.; Hunter, A. D.; Gray, T. G. *Organometallics*. **2009**, *28*, 795.

132. Gao, L.; Partyka, D. V.; Teets, T. S.; Updegraff, J. B. III; Deligonul, N.; Gray, T. G. *Organometallics* **2009**, *28*, 6171.

133. Hashmi, A. S. K.; Ramamurthi, T. D.; Rominger, F. *J. Organomet. Chem.* **2009**, *694*, 592.

134. Schmidbaur, H.; Schier, A. In *Comprehensive Organometallic Chemistry III*; Crabtree, R.; Mingos, M., Eds.; Elsevier: 2006, Volume 2, Section 2.05.

135. Coco, S.; Espinet, P. Liquid Crystals Based on Gold Compounds. In *Gold Chemistry;* Mohr, F., Ed. Wiley-VCH: Weinheim, 2009, pp 357–396.

136. Partyka, D. V.; Esswein, A. J.; Zeller, M.; Hunter, A. D.; Gray, T. G. *Organometallics* **2007**, *26*, 3279.

137. Gao, L.; Peay, M. A.; Partyka, D. V.; Updegraff, J. B. III; Teets, T. S.; Esswein, A. J.; Zeller, M.; Hunter, A. D.; Gray, T. *Organometallics* **2009**, *28,* 5669.

138. Heng, W. Y.; Hu, J.; Yip, J. H. K. *Organometallics* **2007**, *26*, 6760.

139. Neuwahl, F. V. R.; Foggi, P. *Laser Chem.* **1999**, *19*, 375.

140. Griffith, J. S. *Theory of Transition Metal Ions;* Cambridge University Press, Cambridge, 1964, pp. 437–439.

141. Friedrich, J.; Metz, F.; Dörr, F. *Mol. Phys.* **1975**, *30*, 289.

142. Okada, T.; Karaki, I.; Mataga, N. *J. Am. Chem. Soc.* **1982**, *104*, 7191.

143. Hashimoto, S. *J. Phys. Chem.* **1993**, *97*, 3662.

144. Kollár, J.; Hrdlovič, Chmela, Š.; Sarakha, M.; Guyot, G. *J. Photochem. Photobiol.* **2005**, *171*, 27.

145. Langkilde, F. W.; Thulstrup, E. W.; Michl, J. *J. Chem. Phys.* **1983**, *78*, 3372.

146. Ham, J. S. *J. Chem. Phys.* **1953***, 21*, 756.

147. Patt, J. R. *J. Mol. Spectrosc.* **1962**, *9*, 288.

148. Bosque, R.; Sales, J. *J. Chem. Inf. Comput. Sci.* **2002**, *42*, 1154.

149. Maciejewski, A.; Naskrecki, R.; Lorenc, M.; Ziolek, M.; Karolczak, J.; Kubicki, J.; Matysiak, M.; Szymanski, M. *J. Mol. Struc.* **2000**, *555*, 1.

150. (a) Lorenc, M.; Ziolek, M.; Naskrecki, R.; Karolczak, J.; Kubicki, J.; Maciejewski, A. *Appl. Phys. B: Laser Opt.* **2002**, *74*, 19. (b) Ekvall, K.; van der Meulen, P.; Dhollande, C.; Berg, L. -E.; Pommeret, S.; Naskrecki, R.; Mialocq, J.C. *J. Appl. Phys.* **2000***, 87*, 2340.

151. Godbout, N.; Salahub, D. R.; Andzelm, J.; Wimmer, E. *Can. J. Chem.* **1992**, *70*, 560.

152. Dolg, M.; Wedig, U.; Stoll, H.; Preuss, H. *J. Chem. Phys.* **1987**, *86*, 866.

153. Laitar, D. S.; Müller, P.; Gray, T. G.; Sadighi, J. P. *Organometallics* **2005**, *24*, 4503.

154. Miertus S.; Scrocco, E.; Tomasi, J. *Chem. Phys.* **1981**, *55*, 117.

155. Gorelsky, S. I. AOMix: Program for Molecular Orbital Analysis; York University: Toronto, 1997, http://www.sg-chem.net.

156. Gorelsky, S. I.; Lever, A. B. P. *J. Organomet. Chem.* **2001**, *635*, 187.

157. Hamblin, M. R.; Mroz, P. T., G. P.;; Gali, H.; Wharton, T.; Sarna, T.; Pawlak, A. Photodynamic therapy with fullerenes. In *Fullerene Research Advances*; Kramer, C. N., Ed.; Nova Sceince Publishers, Inc.: Hauppauge, N. Y., 2007; pp 1-31.

158. Mroz, P.; Tegos, G. P.; Gali, H.; Wharton, T.; Sarna, T.; Hamblin, M. R. *Photochem. Photobiol. Sci.* **2007***, 6,* 1139.

159. Duncan, T. V.; Frail, P. R.; Miloradovic, I. R.; Therien, M. J. *J. Phys. Chem. B* **2010**, *114*, 14696.

160. Tsuboyama, A.; Okada, S.; Ueno, K. Highly Efficient Red-Phosphorescent Iridium Complexes. In Highly Efficient OLEDs with Phosphorescent Materials; Yersin, H., Ed.; Wiley-VCH Verlag GmbH & Co.: Weinheim, 2008; pp 163-183.

161. Segura Carretero, A.; Salinas Castillo, A.; Fernández Gutiérrez, A. *Crit. Rev. Anal. Chem.* **2005**, *35*, 3.

162. Reichardt, C.; Crespo-Hernández, C. E. *J. Phys. Chem. Lett.* **2010**, *1*, 2239.

163. Reichardt, C.; Guo, C.; Crespo-Hernández, C. E. *J. Phys. Chem. B* **2011**, *115*, 3263.

164. Reichardt, C.; Crespo-Hernández, C. E. *Chem. Comm.* **2010**, *46,* 5963.

165. Vogt, R. A.; Peay, M. A.; Gray, T. G.; Crespo-Hernández, C. E. *J. Phys. Chem. Lett.* **2010**, *1*, 1205.

166. Lu, W.; Kwok, W.-M.; Ma, C.; Chan, C. T.-L.; Zhu, M.-X.; Che, C.-M. *J. Am. Chem. Soc.* **2011**, *133*, 14120.

167. Gao, L.; Partyka, D. V.; Updegraff III, J. B.; Deligonul, N.; Gray, T. G. *Eur. J. Inorg. Chem.* **2009**, 2711.

168. Peay, M. A.; Heckler, J. E.; Deligonul, N.; Gray, T. G. *Organometallics* **2011**, *30*, 5071.

169. Damrauer, N. H.; Cerullo, G.; Yeh, A.; Boussie, T. R.; Shank, C. V.; McCusker, J. K. *Science* **1997**, *275*, 54.

170. Bhasikuttan, A. C.; Suzuki, M.; Nakashima, S.; Okada, A. *J. Am. Chem. Soc.* **2002**, *124*, 8398.

171. Busby, M.; Matousek, P.; Towrie, M.; Vlček, A., Jr. *J. Phys. Chem. A* **2005**, *109*, 3000.

172. Gawelda, W.; Cannizzo, A.; Pham, V.-T.; van Mourik, F.; Bressler, C.; Chergui, M. *J. Am. Chem. Soc.* **2007**, *129*, 8199.

173. Cannizzo, A.; Blanco-Rodríguez, A. M.; El Nahhas, A.; Šebera, J.; Záliš, S.; Vlček, A., Jr.; Chergui, M. *J. Am. Chem. Soc.* **2008**, *130*, 8967.

174. Ramakrishna, G.; Goodson III, T.; Rogers-Haley, J. E.; Cooper, T. M.; McLean, D. G.; Urbas, A. *J. Phys. Chem. C* **2009**, *113*, 1060.

175. El Nahhas, A.; Cannizzo, A.; van Mourik, F.; Blanco-Rodríguez, A. M.; Záliš, S.; Vlček, A., Jr.; Chergui, M. *J. Phys. Chem. A* **2010**, *114*, 6361.

176. Juban, E. A.; McCusker, J. K. *J. Am. Chem. Soc.* **2005**, *127*, 6857.

177. Bhasikuttan, A. C.; Okada, T. *J. Phys. Chem. B* **2004**, *108*, 12629.

178. Monat, J. E.; McCusker, J. K. *J. Am. Chem. Soc.* **2000**, *122*, 4092.

179. van Stokkum, I. H. M.; Larsen, D. S.; van Grondelle, R. *Biochim. Biophys. Acta* **2004**, *1657*, 82.

180. van Stokkum, I. H. M.; Larsen, D. S.; van Grondelle, R. *Biochim. Biophys. Acta* **2004**, *1658*, 262.

181. Jacquemin, D.; Planchat, A.; Adamo, C.; Mannucci, B. *J. Chem. Comput.* **2012**, *8*, 2359.

182. Balzani, V. Photophysics of Transition Metal Complexes in Solution. In CRC Handbook of Photochemistry; 3 ed.; Taylor & Francis Group, LLC: Boca Raton, 2006; pp 60-82.

183. McMillan, D. R. In Physical Methods in Bioinorganic Chemistry; Que, L. Q. J., Ed.; University Science Books: Sausalito, CA, 2000.

184. Abedin-Siddique, Z.; Yamamoto, Y.; Ohno, T.; Nozaki, K. *Inorg. Chem.* **2003**, *42*, 6366.

185. Abedin-Siddique, Z.; Yamamoto, Y.; Ohno, T.; Nozaki, K. *Inorg. Chem.* **2004**, *43*, 663.

186. Cannizzo, A.; van Mourik, F.; Gawelda, W.; Zgrablic, G.; Bressler, C.; Chergui, M. *Angew. Chem. Int. Ed.* **2006**, *45*, 3174.

187. Turro, N. J.; Ramamurthy, V.; Scaiano, J. C. In Modern Molecular Photochemistry of Organic Molecules; 1 ed.; University Science Books: Sausalito, CA, 2010.

188. Capellos, C.; Bielski, B. H. J. Kinetic Systems: Mathematical Description of Chemical Kinetics in Solution; Wiley-Interscience: New York, 1972.

189. Hay, P. J.; Wadt, W. R. *J. Chem. Phys.* **1985**, *82*, 270; Hay, P. J.; Wadt, W. R. *J. Chem. Phys.* **1985**, *82*, 284; Hay, P. J.; Wadt, W. R. *J. Chem. Phys.* **1985**, *82*, 299.

190. Pitts, J. N., Jr.; Vernon, J. M.; Wan, J. K. *Air Water Pollut.* **1965**, *9*, 595.

191. Chen, B.; Yang, C.; Goh, N. K. *J. Environ. Sci. (Beijing, China)* **2005**, *17*, 598.

192. Murov, S.; Carmichael, I.; Hug, G. *Handbook of photochemistry*; Marcel Dekker Inc.: NY, 1993.

193. Lakowicz, J. *Principles of Fluorescence Spectroscopy*; Springer: NY, 2006.